ARMY RESEARCH LABORATORY

A THREE DIMENSIONAL MESOSCALE ATMOSPHERIC SIMULATION SYSTEM FOR USE IN VARIOUS MOBILE BATTLEFIELD ENVIRONMENTS PHASE II: TRANSITION TO AN OPERATIONAL FORECAST SYSTEM

SBIR PHASE II FINAL REPORT

John W. Zack
Kenneth T. Waight III
Steven H. Young
Mary D. Bousquet
Pamela E. Price

MESO, Inc.
185 Jordon Road
Troy, NY 12180

Under Contract DAAD07-90-C-0134
Contract Monitor Teizi Henmi

ARL-CR-98

May 1994

NOTICES

Disclaimers

The findings in this report are not to be construed as an official Department of the Army position, unless so designated by other authorized documents.

The citation of trade names and names of manufacturers in this report is not to be construed as official Government indorse-ment or approval of commercial products or services referenced herein.

Destruction Notice

When this document is no longer needed, destroy it by any method that will prevent disclosure of its contents or reconstruction of the document.

REPORT DOCUMENTATION PAGE

Form Approved
OMB No. 0704-0188

1. AGENCY USE ONLY *(Leave blank)*	2. REPORT DATE	3. REPORT TYPE AND DATES COVERED
	May 1994	Final 15 Sep 90 - 15 Mar 93

4. TITLE AND SUBTITLE
A THREE DIMENSIONAL MESOSCALE ATMOSPHERIC SIMULATION SYSTEM FOR USE IN VARIOUS MOBILE BATTLEFIELD ENVIRONMENTS PHASE II: TRANSITION TO AN OPERATIONAL FORECAST SYSTEM

5. FUNDING NUMBERS
DAAD07-90-C-0134

6. AUTHOR(S)
John W. Zack, Kenneth T. Waight III, Steven H. Young, Mary D. Bousquet, and Pamela E. Price

7. PERFORMING ORGANIZATION NAME(S) AND ADDRESS(ES)
MESO, Inc.
185 Jordon Road
Troy, NY 12180

8. PERFORMING ORGANIZATION REPORT NUMBER
ARMYSBIRII-0393

9. SPONSORING / MONITORING AGENCY NAME(S) AND ADDRESS(ES)
U.S. Army Research Laboratory
Battlefield Environment Directorate
ATTN: AMSRL-BE-W
White Sands Missile Range, NM 88002-5501

10. SPONSORING / MONITORING AGENCY REPORT NUMBER
ARL-CR-98

11. SUPPLEMENTARY NOTES
Teizi Henmi (Contract Monitor)

12a. DISTRIBUTION / AVAILABILITY STATEMENT
Approved for public release; distribution unlimited.

12b. DISTRIBUTION CODE

13. ABSTRACT *(Maximum 200 words)*

A self-contained mesoscale numerical weather prediction system which can generate real-time or historical simulations on a high performance moderate-cost workstation computer was developed and tested in this project. The system is designed to: (1) ingest a variety of atmospheric data types; (2) combine the diverse mixture of ingested data into a dynamically consistent initialization dataset for the numerical model: (3) generate a mesoscale numerical simulation; (4) display the output from the simulation in a variety of graphical and tabular formats; and (5) be easily used and reconfigured through a graphical user interface. The system was created by porting a version of the Mesoscale Atmospheric Simulation System (MASS) from a supercomputer to a Standent 750 vector processing workstation, and then configuring it to perform all the functions of a numerical weather prediction system within the workstation environment. The system was tested by executing 36 simulations with real-time atmospheric data and performing a subjective and objective verification. In addition to the generation of real-time mesoscale simulations for military applications, it is envisioned that the workstation-based mesoscale simulation system could have a considerable number of application in the private sector including the generation of tailored local forecasts for business and government operations that are weather sensitive.

14. SUBJECT TERMS
Mesoscale modeling, numerical weather prediction, data assimilation, model verification, graphical user surface

15. NUMBER OF PAGES
132

16. PRICE CODE

17. SECURITY CLASSIFICATION OF REPORT	18. SECURITY CLASSIFICATION OF THIS PAGE	19. SECURITY CLASSIFICATION OF ABSTRACT	20. LIMITATION OF ABSTRACT
Unclassified	Unclassified	Unclassified	SAR

PROJECT SUMMARY

A self-contained mesoscale numerical weather prediction system which can generate real-time or historical simulations on a high performance moderate-cost workstation computer was developed and tested in this project. The system is designed to: (1) ingest a variety of atmospheric data types; (2) combine the diverse mixture of ingested data into a dynamically consistent initialization dataset for the numerical model; (3) generate a mesoscale numerical simulation; (4) display the output from the simulations in a variety of graphical and tabular formats; and (5) be easily used and reconfigured through a graphical user interface.

The project consisted of three segments. In the first portion of the project, the workstation-based mesoscale atmospheric simulation system was created by porting a version of the Mesoscale Atmospheric Simulation System (MASS) from a supercomputer to a Stardent 750 vector processing workstation, and then upgrading the system by implementing: (1) a new lateral boundary condition scheme; (2) a positive definite advection formulation; (3) a more sophisticated surface energy and moisture budget formulation; (4) a four-dimensional data assimilation system based on a Newtonian relaxation scheme; and (5) a method to enhance the initialization of relative humidity through the use of satellite image data, manually digitized radar (MDR) reports, pilot reports and surface cloud observations. In the second portion of the project, a graphical user interface (GUI) was developed to permit the user to easily reconfigure the system and execute simulations, and the model software was modified to increase its computational performance on the workstation computer. The final segment of the project consisted of the execution of a observation system simulation experiment (OSSE) to test the performance of the data assimilation system, and the execution of 36 real data simulations to evaluate the performance of the simulation system in a variety of environments.

The 36-case evaluation experiment indicated that the modeling system was able to consistently simulate some classes of phenomena quite well. These included (1) synoptic or meso-α scale features which are well-resolved by the rawinsonde network, (2) convective events which are strongly forced by larger scale circulations, (3) mesoscale circulations which are tied to surface features that are well-represented, e.g. land/sea breezes, terrain-induced circulations; (4) surface and boundary layer flows occurring under quiescent (clear, non-convective) conditions. However, the evaluation experiment also suggested that there was a set of phenomena that was difficult to simulate well. These phenomena included (1) convective events which are only weakly forced by larger scale circulations (i.e. quasi-barotropic systems); (2) features which result from convective-scale feedback to the grid scale (e.g. from latent heat release, downdrafts, etc.); (3) mesoscale circulations which are driven by more subtle surface gradients, especially soil moisture; (4) circulations driven by the effects of cloud boundary on the surface energy budget; and (5) features in the vicinity of large terrain gradients.

In addition to the generation of real-time mesoscale simulations for military applications, it is envisioned that the workstation-based mesoscale simulation system could have a considerable number of applications in the private sector including the generation of tailored local forecasts for business and government operations that are weather sensitive. A number of organizations in the transportation, recreation, construction and utility industries could benefit from high resolution short-term weather forecasts that could be provided by such a system.

Three significant factors should permit the computational and meteorological performance of the simulation system to dramatically increase during the next few years: (1) the computational power of workstation computers will increase and thereby permit higher resolution models with more complex physics to executed on workstation-class machines; (2) model initialization data with mesoscale and cloud-scale resolution will become available from new atmospheric observing systems; and (3) the physics of the model will be improved as the knowledge of mesoscale and cloud-scale phenomena increases.

TABLE OF CONTENTS

1. Introduction

Atmospheric conditions can have a significant impact on military operations within a battlefield environment. Some of the environmental factors which can impact the success of a military operation include: (1) the state of the ground surface; (2) vertical and horizontal visibility; (3) the temperature of the ground and the surface air; (4) the vertical profile of temperature and moisture; and (5) the vertical profile of the wind direction and speed. Significant precipitation can cause the soil to become saturated and turn to mud which can adversely impact the ability of a vehicle to quickly traverse an area. Clouds and fog can impose severe restrictions on visibility which can inhibit aircraft operations and even ground-based activities. Extreme cold or heat at the surface of the earth can cause problems with the operation of some types of equipment and with the ability of personnel to efficiently perform critical tasks. The vertical profiles of temperature and moisture can impact the propagation characteristics of electromagnetic and acoustic sensing systems and can prevent or enhance the ability of personnel to acquire critical information. The direction and speed of the wind can play an important role in determining the manner in which substances (some which may be toxic) injected into the air as a planned or inadvertent result of explosive detonations are dispersed. The manner in which such substances are dispersed by the atmospheric circulation may be critical to the survival of personnel in an area.

Due to these potential effects of weather on a variety of military operations, weather information can play an important role in the decision-making process. In recent years, weather information for military operations has been extracted by forecasters from the output of large scale numerical weather prediction models that are executed at centralized military forecast centers such as the Air Force Global Weather Central (AFGWC) in Omaha, Nebraska, or the Fleet Numerical Oceanographic Center (FNOC) in Monterey, California. These forecasts have been quite successful at providing information about the evolution of general conditions over an area of interest. However, it has long been recognized that weather conditions can vary significantly on short space and time scales within an area of operations, which is typically a few hundred kilometers on each side. For example, heavy rain from thunderstorms can create very moist soil conditions that drastically reduce the trafficability over an area which is less than 100 km on a side, while soil conditions in other nearby areas remain relatively dry and favorable for the movement of military vehicles. Similar variations can occur in the other meteorological parameters that have a direct impact on military operations. Thus, it would be desirable to have forecast information about the mesoscale (10 - 500 km) and cloud-scale (< 10 km) variability of the important parameters.

A logical approach to the prediction of the mesoscale and cloud-scale variability of weather-related conditions in the battlefield environment is to extend the dynamical simulation model technology that has proven so successful in generating global and continental scale forecasts to the mesoscale and cloud-scale. Mesoscale and cloud-scale models which could be used for this purpose have been under development by several universities (e.g. Perkey, 1976; Warner and Seaman, 1990; Tripoli and Cotton, 1989) and federal research organizations (Hodur, 1987; Mesinger et al., 1988), as well as a few private companies (Kaplan et al., 1982c) since the late 1970's. Research investigations have shown that these models have considerable skill in simulating the mesoscale and cloud-scale variability associated with some types of atmospheric phenomena (e.g. Kocin et al., 1985; Zhang and Fritsch, 1988), but have considerable difficulty in correctly simulating other classes of mesoscale or cloud-scale phenomena. Nevertheless, the perception among many meteorologists is that these models offer the potential to significantly improve the ability to produce accurate short-term forecasts over small regions in at least some situations. However, these models must be executed at a very high computational rate if their output is to be available in real time. Until recently, it was only possible to generate forecasts (as

opposed to historical simulations) from these models by using a high performance supercomputer, such as a Cray XMP or Cray 2, which cost tens of millions of dollars. In fact, the generation of real-time cloud-scale simulations is still slightly beyond the capability of the fastest supercomputers. The requirement for extremely high computational power meant that the cost of generating real-time mesoscale numerical simulations was very high and that the forecasts could be generated only at operational centers which possessed such computer systems. In most instances, this was not feasible, because the supercomputer resources at these centers were already totally committed to the ingestion and processing of the real-time atmospheric data and the execution of global and regional forecast models. Thus, computational resources have generally not been available at operational centers to execute real-time high resolution mesoscale simulations over limited areas.

Recent advances in computer technology have provided an alternative approach. High performance, moderate-cost computer workstations now have the computational power to execute a high resolution (e.g. 10 km grid increment) mesoscale simulation over a 500 x 500 km area in time to have a significant period of forecast utility. This capability raises the possibility of executing mesoscale simulations over limited areas on workstation computers at local sites where forecast information is needed. Such a system would have several advantages for use in military applications. First, the components of the modeling systems could be selected for each application based upon which configuration of the model is likely to perform best in a particular environment. This is an issue because certain components of the model physics are not understood sufficiently well to formulate a general mathematical treatment that is valid for all environments. An example of this problem is the parameterization of the effects of sub-grid scale moist convection. At present, there is no universal parameterization that works equally well for all grid scales and all environments. Thus, there can be an advantage to selecting an appropriate scheme for a particular application. This would be very difficult to do at a forecast center which must execute a simulation over a large domain which encompasses many types of environments. However, it is quite feasible for local area simulations on a computer workstation. This also has the possibility of accelerating the computational rate of a simulation if some physics can be omitted from a simulation in a particular situation without significantly degrading the forecast. A second advantage of the local workstation system is that the system could be easily adapted to ingest local datasets that might not be available to the operational forecast center. For example, the military has (and will enhance) the capability to gather meteorological data throughout the battlefield environment through the use of surface and airborne sensors which accompany operational units. This data could be transmitted back to the local workstation computer for assimilation into the local simulations. A third point is the fact that the local system could continue to ingest local data and generate updated simulations even if communications with the central forecast center were lost during an operation. Finally, the local simulation system provides a large degree of flexibility to the decision-makers which require timely and easily-interpreted display of meteorological information for use as a Tactical Decision Aid (TDA). Simulations could be generated by the workstation system on demand with the latest information. Thus, if other factors dictate a requirement for a re-evaluation of the operational plan, updated weather forecast information could be generated and displayed in an easily interpreted format for quick access during the decision-making process. Such an on-demand service would be difficult for a central forecast center to satisfy, since it generally has a commitment to provide numerical forecast products to a much larger area. A redirection of resources to the localized simulation could compromise the quality of weather information for other regions. All of these factors suggest that it would be desirable to construct a self-contained workstation-based mesoscale atmospheric simulation system. This was the basic objective of this Small Business Innovation Research (SBIR) project.

It was envisioned that a workstation-based mesoscale simulation system would also have a considerable number of applications in the private sector. One application with considerable

potential is the generation of tailored local forecasts for business and government operations that are weather sensitive. A number of organizations in the transportation, recreation, construction and utility industries could benefit from high resolution short-term weather forecasts that could be provided by such a system. Universities could also utilize the workstation-based simulation system as an instructional or research tool.

The fundamental approach to the creation of a high quality workstation-based simulation system in this project was to port an existing mesoscale atmospheric simulation model to a high performance computer workstation and to enhance the system by: (1) broadening its ability to assimilate a diverse mixture of atmospheric data types; (2) improving the physics of the model by incorporating state-of-the-art formulations for certain key components of the atmospheric physics; (3) selecting an appropriate high performance moderate-cost workstation computer system to serve as the computational platform for the simulation system and then optimizing the model to execute efficiently on this system ; and (4) developing a graphical user interface (GUI) to permit the user to easily and quickly configure the data assimilation and simulation model for a particular application. The modeling system that was selected to port to the workstation was the Mesoscale Atmospheric Simulation System (MASS) model (Kaplan et al., 1982c). The history and structure of this modeling system is described in Chapter 2 of this report.

The technical feasibility of the workstation-based mesoscale atmospheric simulation system was demonstrated during the Phase I portion of this project, by executing a MASS simulation over the Honduras/Nicaragua border region of Central America on an Alliant FX-1 computer system. The model was able to execute at a sufficient rate to permit real-time forecasts to be generated over small domains. Furthermore, the numerical model was able to replicate realistic meteorological features in the flow field, including the development and inland propagation of a sea breeze convergence front and intricate mountain/valley wind circulations in regions of complex terrain. Bursts of a low-level "dust" tracer and plumes of an upper-level "smoke" tracer were injected into the model grid domain and their transport was successfully simulated. The advection of these optical obscurants conformed to the detailed flow patterns generated by the locally-forced atmospheric circulations.

The objective of the Phase II project was to transform the modeling system into a tool that could efficiently be used to generate quality real-time or research simulations on a high performance workstation computer. The first task during Phase II was to select an appropriate computational platform for the simulation system. The Stardent 750 workstation was chosen because it had a custom vector processor that was similar to those found on supercomputers such as the Cray systems. Since the MASS code was originally designed to execute efficiently in a vector processing environment, it was anticipated that it would perform quite well on the Stardent system, even though the system's scalar processing speed was not significantly faster than other workstation computers available at the time it was acquired. Benchmark tests of the MASS code proved this expectation to be true. Once the computational platform was selected, four types of enhancements to the system were made: (1) the numerical algorithms and physics included in the weather prediction model were improved to increase the accuracy of the mesoscale simulations; (2) the initialization procedure of the model was augmented so that real-time meteorological data from local battlefield sensors could be incorporated into the forecasts; (3) a user-friendly graphical user interface (GUI) was developed in order to allow the simulation system to be operated easily with minimal training, and to reduce the probability of user errors; and (4) the simulation system software was optimized so that the time to execute a simulation on a workstation computer could be minimized. This report describes the work completed in each of these areas during Phase II.

An overview of the MASS model is presented in Chapter 2. The improvements to the modeling system that were implemented during this project are described in Chapters 3, 4 and 5. The improvements included the implementation of: (1) a radiative lateral boundary condition formulation to improve the simulation of the flow near the lateral boundaries of the model; (2)

the MPDATA advection scheme; and (3) an augmented surface energy and moisture budget formulation. The implementation of a four dimensional data assimilation capability and an enhanced static initialization capability is described in Chapter 6. This chapter includes a description of the Newtonian relaxation (i.e. nudging) scheme that can be used to assimilate rawinsonde, surface or wind profiler data, and can easily be extended to other data types. An Observation Simulation System Experiment (OSSE) was conducted to analyze the impact of different data types on the data assimilation scheme. The design, implementation and results from this experiment are described in Chapter 7. The modeling system was evaluated by executing a set of 36 simulations and subjectively and objectively verifying the results. The results of the evaluation experiment are presented in Chapter 8. The development and design of the GUI is described in Chapter 9. A summary of the work completed in this project is presented in Chapter 10. This chapter also includes a discussion of the areas in which future model development is required.

2. Overview of the MASS Model

The modeling system used as the basis for the workstation-based mesoscale simulation system was version 5 of the Mesoscale Atmospheric Simulation System (MASS). The first documented version (MASS 2.0) of this model was described by Kaplan et al. (1982c). MASS was originally formulated as a limited area hydrostatic mesoscale modeling system. The model finite-difference equations were formulated on a terrain-following normalized pressure coordinate system and an unstaggered horizontal grid in which all prognostic variables were computed at the same grid point. Sixth-order accurate horizontal space finite differences were used to calculate spatial derivatives and the Euler-backward time marching scheme was employed. A 30-case sample of MASS 2.0 simulations was gathered during the spring and summer of 1982. This sample was extensively analyzed by scientists at the Goddard Space Flight Center. The synoptic scale forecast skill of the model was evaluated and compared to the highest resolution model then operationally available, NMC's LFM model. The results of this study were reported in Koch et al. (1985). The same sample of cases was used to investigate the ability of the model to predict the genesis of intense mesoscale convective systems. The results of that analysis was reported in Koch (1985).

After the 1982 test period the MASS 2.0 model was upgraded to version 3.0. The upgrades were described in Wong et al. (1983). The improvements included additions to the surface energy and moisture budgets and the implementation the Fritsch and Chappell (1980) cumulus parameterization scheme. A version of the Kuo-Anthes (Anthes, 1977) cumulus parameterization schemes was implemented in 1984. The 6th-order accurate finite difference approximations were replaced with 4th-order accurate approximations since the higher order formulation provided a minimal benefit at a significant computational cost. The MASS 3.0 model was used in a series of dynamical case studies in the middle 1980's. The MASS model was used to study the mesoscale evolution of the Grand Island tornado case of June 3, 1980 by Kaplan et al. (1982d), Coats et al. (1984) and Kaplan et al. (1985). Coats et al. (1984) used MASS to investigate the effect of soil moisture gradients on the evolution of the mesoscale environment in this event. Zack et al. (1984) studied the effect of boundary layer fluxes and deep convective processes on the evolution of the early phases of the east coast snowstorm of February 10, 1983 (the Megalopolitan Snowstorm). Uccellini et al. (1983), Uccellini et al. (1987) and Whitaker et al. (1988) used the Goddard Space Flight Center version of the MASS model to investigate the role of jet streak dynamics and boundary layer fluxes in their multi-year study of the Presidents' Day snowstorm of February 18-19, 1979. Kocin et al. (1985) documented the performance of the MASS model for a Washington DC snowburst event in March of 1984. Zack and Kaplan (1987) used the MASS model to study the evolution of the severe storm environment of the April 10, 1979 Wichita Falls tornado outbreak which was also the first field day of the AVE-SESAME experiment.

Version 4 of the MASS model was formulated in 1988. The Euler backward time marching scheme was replaced by a split explicit scheme as reported by Karyampudi et al. (1988). In addition to this change, a version of the Blackadar boundary layer parameterization scheme (Zhang and Anthes, 1982) was implemented. Zack et al. (1988) used this version of the model to study the impact of synthetic relative humidity data derived from satellite data on the short term simulation of convective precipitation over the Florida peninsula. Waight et al. (1989) and Waight and Zack (1990) used MASS to simulate the evolution of convection during one of the cases that were intensively observed during the Cooperative Huntsville Meteorological Experiment (COHMEX). Cram et al. (1991) utilized version 4 of MASS to conduct an Observation System Simulation Experiment (OSSE) to test a scheme to retrieve temperature data from wind data reported by the experimental network of four wind profiler in eastern Colorado.

Version 5.0 of the MASS model was developed during 1991 and 1992. This version of the model included a prognostic grid scale moisture scheme, an enhanced surface energy budget, a modified Kuo cumulus parameterization scheme that included convective scale downdrafts and a more comprehensive long and short wave radiation scheme.

The model was further developed during this project by (1) adding a four dimensional dynamic data assimilation capability based on a Newtonian relaxation scheme and the specification of vertical profiles of latent heating and moistening from cloud and precipitation observations.; (2) broadening the scope of the surface energy and moisture budgets; (3) implementing a radiative lateral boundary condition formulation; (4) incorporating a positive definite advection scheme for selected prognostic variables; and (5) improving the computational efficiency of the model software. At the end of the project the version of MASS which included all of these enhancements was designated as version 5.5. The main components of MASS 5.5 are summarized in Table 2-1. A detailed description of this version of the model can be found in the MASS Version 5.5 Reference Manual (MESO, 1993a). The components that are shaded in Table 2-1 were added or significantly upgraded during this project. Chapters 3 through 6 of this report provide additional detail about the improvements to the modeling system that were completed in this project.

Table 2-1 Summary of MASS 5.5.

Initialization
• Automatic calculation of terrain, land/water distribution, land use, climatological vegetation index value at resolution of chosen grid domain.
• Accepts several types of NMC gridded data as first guess fields: LFM, NGM, Gridded Optimum Interpolation (GOI). Data from previous MASS run can also be used as first guess fields.
• Soil temperature based on surface temperature averaged over the previous three days.
• Re-analysis using either Barnes or optimum interpolation objective analysis scheme with significant level rawinsonde, surface, and wind profiler data.
• Static assimilation of synthetic relative humidity profiles derived from surface cloud observations, pilot reports, manually digitized radar (MDR) data and infrared and visible satellite data.
Numerical Techniques
• 3-D prognostic equations for u, v, T, p_s, q_v, q_c and q_r.
• Hydrostatic assumption.
• Terrain following σ_p (normalized pressure) vertical coordinate.
• Arakawa unstaggered "A" grid on a stereographic map image plane.
• Fourth-order accurate horizontal space differencing.
• Split-explicit time marching scheme.
• Forward-backward scheme used for inertia-gravity modes.
• Adams-Bashforth scheme used for the advection terms.
• Positive definite advection scheme (MPDATA) available as alternative to Adams-Bashforth.
• Absorbing upper layer can be used to damp vertically propagating waves.
• Dynamic data assimilation (nudging) of rawinsonde, wind profiler, surface and radar data.
PBL Physics
• Blackadar high resolution PBL parameterization.
• Detailed surface energy and moisture budgets including three-layer surface hydrology scheme, and vegetation-sensitive evapotranspiration scheme.
• Uses high resolution (1 km) USGS land use and vegetation index databases to determine surface characteristics such as roughness height, fraction of surface covered by vegetation, etc.
Moisture Physics
• Prognostic equations for cloud water and ice (q_c) and rain water and snow (q_r) (Diagnostic condensate scheme available as an option).
• Simplified parameterization of cloud microphysical interactions.
• Kuo-type cumulus parameterization with moist downdraft physics (Fritsch-Chappell scheme available as an option).

Dust/Smoke Physics
• Option to incorporate an arbitrary number of dust/smoke mixing ratio variables. • Parameterization of gravitational settling.
Radiation
• Longwave and shortwave radiation parameterized in surface energy budget and in the free atmosphere. Interaction with atmospheric cloud and rain fields, and with parameterized sub-grid clouds.

3. Implementation of Radiative Boundary Conditions

All previous versions of MASS utilized the sponge boundary condition originally proposed by Perkey and Kreitzberg (1976). In this formulation the tendencies of prognostic variables from an external source are blended with internally-generated tendencies within a region around the boundaries of the domain.

In this formulation, the tendency of a prognostic variable at a point near the boundary is specified by the relationship,

$$\frac{\partial \chi}{\partial t} = W(I)\frac{\partial \chi}{\partial t_{int}} + [1-W(I)]\frac{\partial \chi}{\partial t_{ext}} \qquad (3\text{-}1)$$

where the subscript "int" denotes an internally-generated model tendency and the subscript "ext" denotes a tendency from an external source such as a larger scale model or an analysis of observational data. W is a weighting factor which determines the relative contributions of the internal and external tendencies to the final grid point tendency. The values of the weighting coefficients W(I) are:

$$W(I) = \begin{cases} 0.0 \text{ for I = the boundary grid points} \\ 0.4 \text{ for I = the boundary-1 grid points} \\ 0.7 \text{ for I = the boundary-2 grid points} \\ 0.9 \text{ for I = the boundary-3 grid points} \\ 1.0 \text{ for I = all other interior grid points} \end{cases}. \qquad (3\text{-}2)$$

If these weighting coefficients are utilized, then the boundary point is completely specified by the external tendency while the tendency at a point 4Δ from the boundary is completely determined by the model physics.

Perkey and Kreitzberg (1976) demonstrated that the effect of this boundary condition is to reduce the phase velocity of a disturbance as it approaches the boundary. This transforms long- and medium-length advective and gravity waves into short waves which can then be removed by a low pass filter, thereby giving the appearance that the exiting waves simply passed through the boundary. This formulation performs reasonably well, but it does have some drawbacks for mesoscale simulations on workstation computers.

The most significant negative is the fact that at least 4 points adjacent to each lateral boundary must be used to apply the boundary condition. All the terms in the equations must be solved at all of the boundary condition points with the exception of the outermost row and column. This results in the execution of a sizable number of computations just to apply the boundary condition. It also causes the size of the interior portion of the domain to be reduced since a total of 8 points in each horizontal coordinate direction must be used for boundary conditions. This is somewhat acceptable on supercomputers where large matrix sizes can be employed. However, it represents a considerable fraction of the domain when the simulations must executed with a moderate matrix size in order to keep the processing time within real-time constraints on a workstation computer. For example, a 55 by 50 matrix becomes a 47 by 42 matrix of interior points.

In order to address these problems, it was decided to implement a nonperiodic, open lateral boundary condition based on the radiation condition:

$$\frac{\partial \chi}{\partial t} + C\frac{\partial \chi}{\partial n} = 0 \ , \qquad (3\text{-}3)$$

where χ is a prognostic variable, n is the coordinate perpendicular to the boundary, and C is the phase velocity directed normal to the boundary. Orlanski (1976) developed a boundary condition for atmospheric models based upon this condition. In the Orlanski scheme, the phase speeds for each prognostic variable are explicitly calculated at the nearest interior grid point, then applied at the boundary during the subsequent timestep. A version of this radiative formulation, adapted for use in MESO's TASS (Terminal Area Simulation System) cloud scale model (Proctor, 1985), has been shown to allow a realistic propagation of disturbances through the open lateral boundaries with a minimum of wave reflection.

3.1 Orlanski Radiative Formulation

In the Orlanski (1976) formulation, the values of the dependent variables at the boundaries of the domain are determined from the relationship

$$\frac{\partial \chi}{\partial t} = -C\frac{\partial \chi}{\partial n} \ , \qquad (3\text{-}4)$$

where χ is any prognostic variable, C is the phase velocity of waves propagating normal to the boundary of the domain, and n is the grid coordinate in the direction normal to the boundary. In order to use this relationship, the phase velocity must be specified. In practice, there are a number of wave modes which are impinging upon the boundary at a particular time, each with its own phase velocity. Consequently, the most rigorous application of (3-4) requires a *decomposition* of the prognostic variable field into its component wave modes and the calculation of a phase velocity for each mode. This would require a significant amount of computational resources if it had to be done at every model timestep. Fortunately, a simpler approach has proven to yield reasonable results in most circumstances. In the simpler approach, a composite phase velocity is estimated by solving (3-4) for "C" at a point adjacent to the boundary point:

$$C = -\frac{\dfrac{\partial \chi}{\partial t}}{\dfrac{\partial \chi}{\partial n}} = -\frac{\chi^{t}(BP\text{-}1) - \chi^{t-\Delta t}(BP\text{-}1)}{\chi^{t}(BP\text{-}1) - \chi^{t}(BP\text{-}2)}\frac{\Delta n}{\Delta t} \ . \qquad (3\text{-}5)$$

In this expression, BP denotes the boundary point, t is the current time, Δt is the length of a model timestep, and Δn is the grid increment in the direction normal to the boundary. The phase velocity calculated from this expression represents a composite value which does not correspond to the phase velocity of a particular mode. However, it should be close to the mean phase velocity of the highest amplitude waves. The value of C is restricted by the following requirements:

(1) If $-\partial\chi/\partial t \ / \ \partial\chi/\partial n \ > \Delta n/\Delta t$ then

$$C = \frac{\Delta n}{\Delta t} . \qquad (3\text{-}6)$$

This represents the maximum feasible numerical velocity. That is, the wave would move one grid increment in one timestep.

(2) If $0 < -\partial\chi/\partial t \; / \; \partial\chi/\partial n \; < \Delta n/\Delta t$ then

$$C = -\frac{\frac{\partial \chi}{\partial t}}{\frac{\partial \chi}{\partial n}} \qquad (3\text{-}7)$$

from (3-4). This condition represents an outward propagation at less than the maximum speed.

(3) If $-\partial\chi/\partial t \; / \; \partial\chi/\partial n \; < 0$, then $C = 0$ and

$$\chi^{t+\Delta t}(BP) = \chi^{t}(BP) + \left(\frac{\partial \chi}{\partial t}\right)_{ext} \Delta t \; , \qquad (3\text{-}8)$$

where $(\partial\chi/\partial t)_{ext}$ is a tendency from an external source such as a larger scale model or a gridded observational dataset. This case represents inward propagation. In this situation, the condition insures that no interior information is used to update the value of the prognostic variable at the boundary point.

3.2 Implementation and Testing

Before the software for the radiative boundary conditions was inserted in the three-dimensional version of the MASS model, the scheme was tested in a simple two-dimensional advection program. A couple of two-dimensional simulations were executed. The first simulation employed a simulation grid with 25 points in the I (left to right) direction and 20 points in the J (up and down direction). The grid spacing was specified as 50 km and the timestep was set to 60 s. A tracer value of 10 units was specified over a 7 x 7 set of points centered at point I=18, J=10. A uniform flow of 25 m s^{-1} along the I-axis was used to advect the tracer substance. In order to execute the simulations quickly on a Macintosh II microcomputer, the 1st-order MPDATA (donor cell) advection scheme was used for the advection computations. This resulted in a more diffusive solution than would be the case had the 3rd-order MPDATA scheme been utilized (see section 5). However, this should not have had a significant effect on the conclusions about the performance of the radiative boundary condition software. The second simulation was identical to the first with the exception that the I-dimension of the domain was expanded from 25 points to 35 points. Thus, the boundary column (I=25) on the first run was located 10 points to the left of the boundary in the second run. Therefore, the tracer values for the I=25 column in Run 1 (designated the "Boundary" run) were determined by the radiative boundary conditions while in Run 2 (termed the "Internal" run), they were the result of the MPDATA advection calculations. Both simulations were executed for a total of 720 timesteps which is equivalent to 12 hours of simulated time. Figure 3-1a illustrates the history of the tracer values at the point I=25, J=10 for both Run 1 and Run 2. The values are so similar that only one

curve is perceptible in the figure, even though data from both runs were plotted. The difference between the two curves is shown in Figure 3-1b. The magnitude of the difference peaks approximately 30 to 40 timesteps before the tracer value peaks at the boundary point. At 25 m s^{-1} the tracer peak would take 33.3 timesteps to move across one 50 km grid cell. Thus, the peak in the difference values occurs at the time when the peak of the tracer pool is approaching the point that is one grid interval from the boundary. An explanation for this behavior can be formulated by recalling that the phase velocity used to transport the tracer from the interior to the boundary point is determined by

$$C = -\frac{\frac{\partial \chi}{\partial t}}{\frac{\partial \chi}{\partial n}}, \qquad (3\text{-}9)$$

where the numerator is the temporal derivative at the point adjacent to oundary and the denominator is the spatial derivative normal to the boundary. In the version of the radiative boundary condition subroutine that was implemented in the MASS code, the temporal derivative is determined by time differences of the tracer values one point in from the boundary, and the spatial gradient is calculated from the difference in tracer values between the points one and two grid intervals in from the boundary. As the tracer maximum passes through the area bounded by the two points used to calculated the spatial derivative the sign of the derivative must change. Therefore, the spatial derivative history curve must pass through zero. The software is formulated so that a zero value can never be used in the calculation of the phase velocity. However, very small values of the spatial derivative can result in large values of the calculated phase velocity. The only limit on C is the ratio of the grid spacing to the timestep, which in this case is 833 m s^{-1}. Figure 3-1c illustrates the variation of C at point I=25, J=10 for the Boundary run. The calculated values are generally very close to the actual constant advective speed of 25 m s^{-1} used in both simulations. However, a noticeable perturbation is present just after the 180th timestep, when the tracer peak passes between points I=23 and I=24 and the calculated value of the spatial derivative approaches zero. Despite this singularity in the C values, Figure 3-1a indicates that the quality of the simulation at the boundary point is still quite good.

Another view of the evolution of the Boundary simulation is shown in Figure 3-2. The initial tracer distribution is contoured in Figure 3-2a. The advection of the tracer downstream is depicted in the plots for 120, 240 and 360 timesteps in figures 3-2b, 3-2c and 3-2d. These plots confirm the expectation that the first order MPDATA scheme would significantly diffuse the tracer pool during the course of the simulation. However, it can also be seen that the pool passes through the boundary without the development of any spurious reflections or others perturbations. In addition to the two simulations described in the preceding paragraphs, several tests were run with different magnitudes for the advective velocity and transport across each of the four sides of the domain. All of these simulations produced satisfactory results.

The Orlanski-type radiative lateral boundary condition formulation was then implemented into the three-dimensional MASS model. An experiment was conducted to verify that the boundary condition formulation and software were working satisfactorily and to compare the performance of the new radiative boundary condition to the Kreitzberg-Perkey porous sponge boundary condition that was previously used in the MASS model. The boundary condition test was conducted by running three simulations. All three simulations were initialized with an identical analytical dataset generated from the set of equations formulated by Fritsch et al. (1980). All of the simulations used 20 vertical layers extending from a flat surface at 0 m elevation to 100 mb and a horizontal grid distance of 20 km. The relative humidity was set to a uniform initial value of 1% so that no condensation would occur during the simulation. Each

simulation was executed for a period of 6 hours. The first simulation was the control simulation. This simulation was initialized over a 50 by 40 horizontal matrix that covered the entire area shown in Figure 3-3a. The second simulation was integrated over a 40 × 30 matrix that covered the area depicted by the inner box in Figure 3-3a. This simulation used the Kreitzberg-Perkey porous sponge lateral boundary condition formulation and will be referred to as the "sponge" simulation. The lateral boundaries of the domain for the second simulation are within the domain of the control simulation. Thus, a comparison of the sponge simulation with the control simulation provides a measure of the impact of the lateral boundary conditions on the sponge simulation. The third simulation was identical to the second simulation with the exception that the radiative lateral boundary condition formulation was used. This simulation will be referred to as the "radiative" simulation. The 300 mb height and wind fields at the end of each 6 hr simulation are shown in Figures 3-3b, 3-3c and 3-3d. These fields reveal that there is a noticeable phase error in the sponge simulation which is much less significant in the radiative simulation. The phase error is revealed by the position of the main ridge axis in each simulation. In the control simulation the ridge axis extends from eastern South Dakota southward to eastern Nebraska. The radiative simulation places the axis in almost the same location. However, the sponge simulation places the ridge axis over South Dakota well to the west of its position in the control simulation. An examination of the mass and momentum fields at other levels indicates that, in general, the radiative simulation reproduced the features of the control simulation somewhat better than the sponge simulation. The one negative aspect of the radiative simulation was that there was a domain-scale mass depletion during the course of the simulation that was not present in the sponge simulation. One manifestation of the mass depletion is that the average 300 mb heights are about 100 m lower in the radiative simulation than they are in the sponge or control simulations. The mass depletion was a result of the fact that the radiative boundary condition formulation results in a mixture of externally-specified (inflow points) and internally-specified (outflow points) values being assigned to the boundary points of the domain. This is not a problem when all of the boundary points are specified from a single external source as is the case when the sponge lateral boundary condition is employed. This problem was corrected by enforcing a domain-scale total mass constraint as part of the radiative boundary condition formulation.

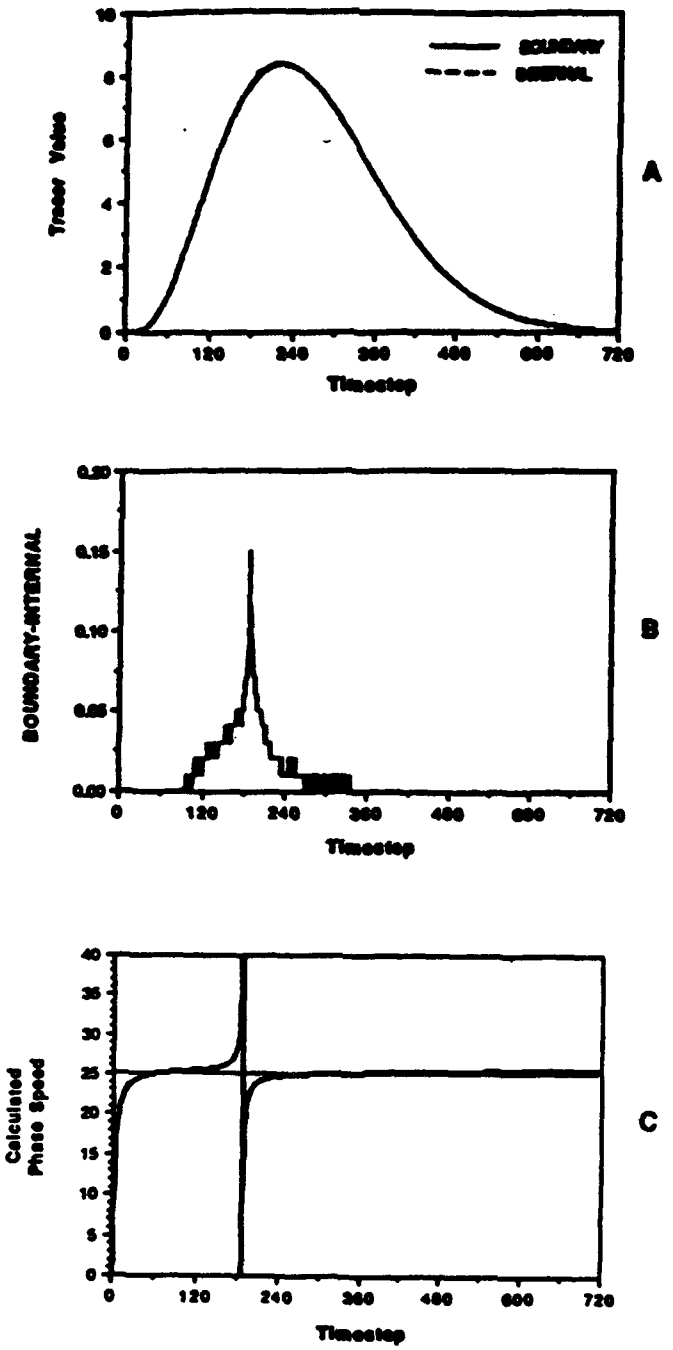

Figure 3-1 *History plots from the two-dimensional radiative boundary condition test simulations: (a) tracer values from the point (25, 10) for the "Boundary" and "Internal" simulations. Note that the curves for the two simulations are virtually coincident. (b) Difference in tracer values at point (25, 10) between the "Boundary" and "Internal" simulations; and (c) calculated phase speed "C" from the point (25, 10) from the "Boundary" run.*

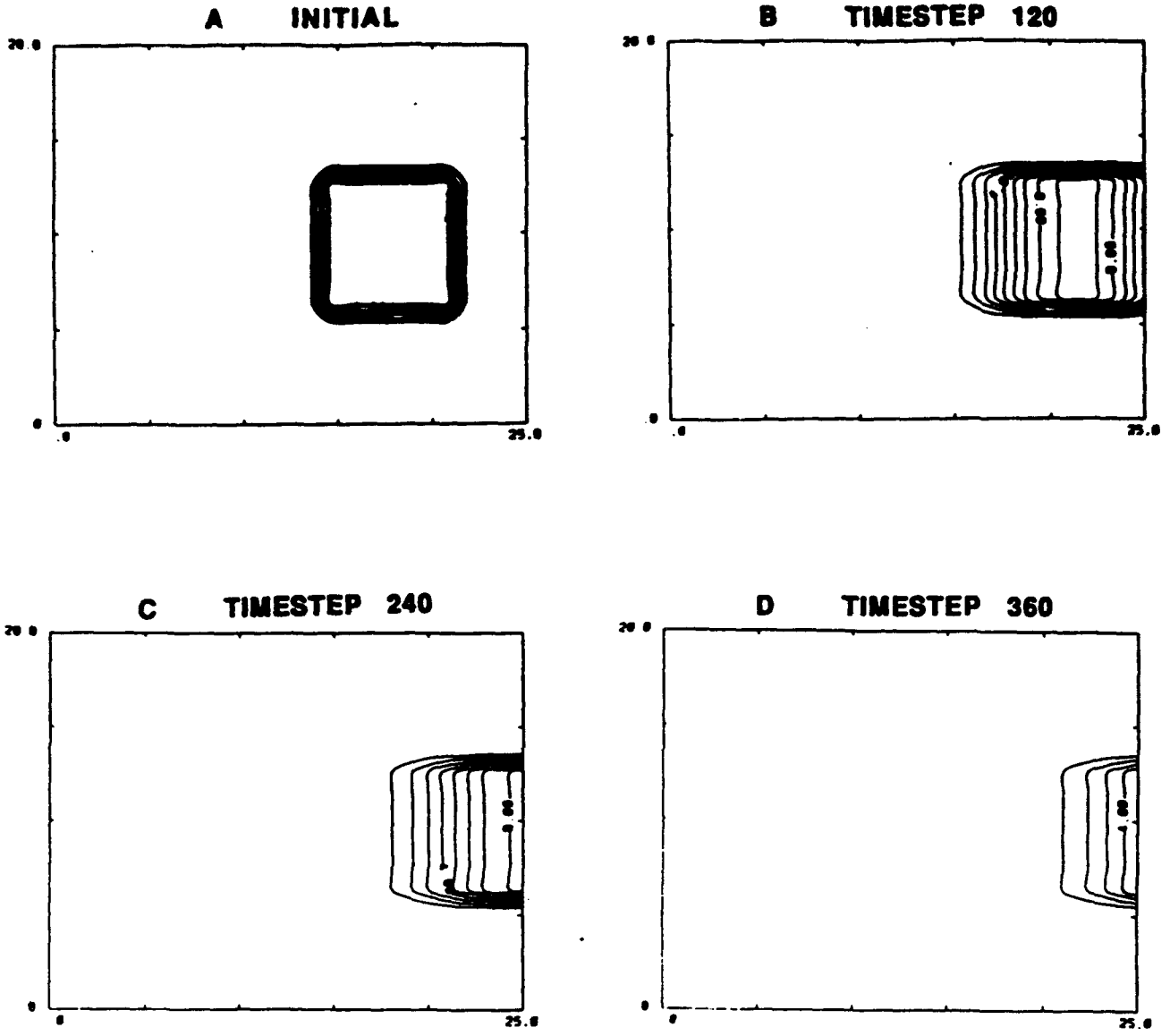

Figure 3-2 Contours of tracer values in the I-J plane from the "Boundary" simulation for: (a) the initial time; (b) after 120 timesteps; (c) after 240 timesteps; and (d) after 360 timesteps.

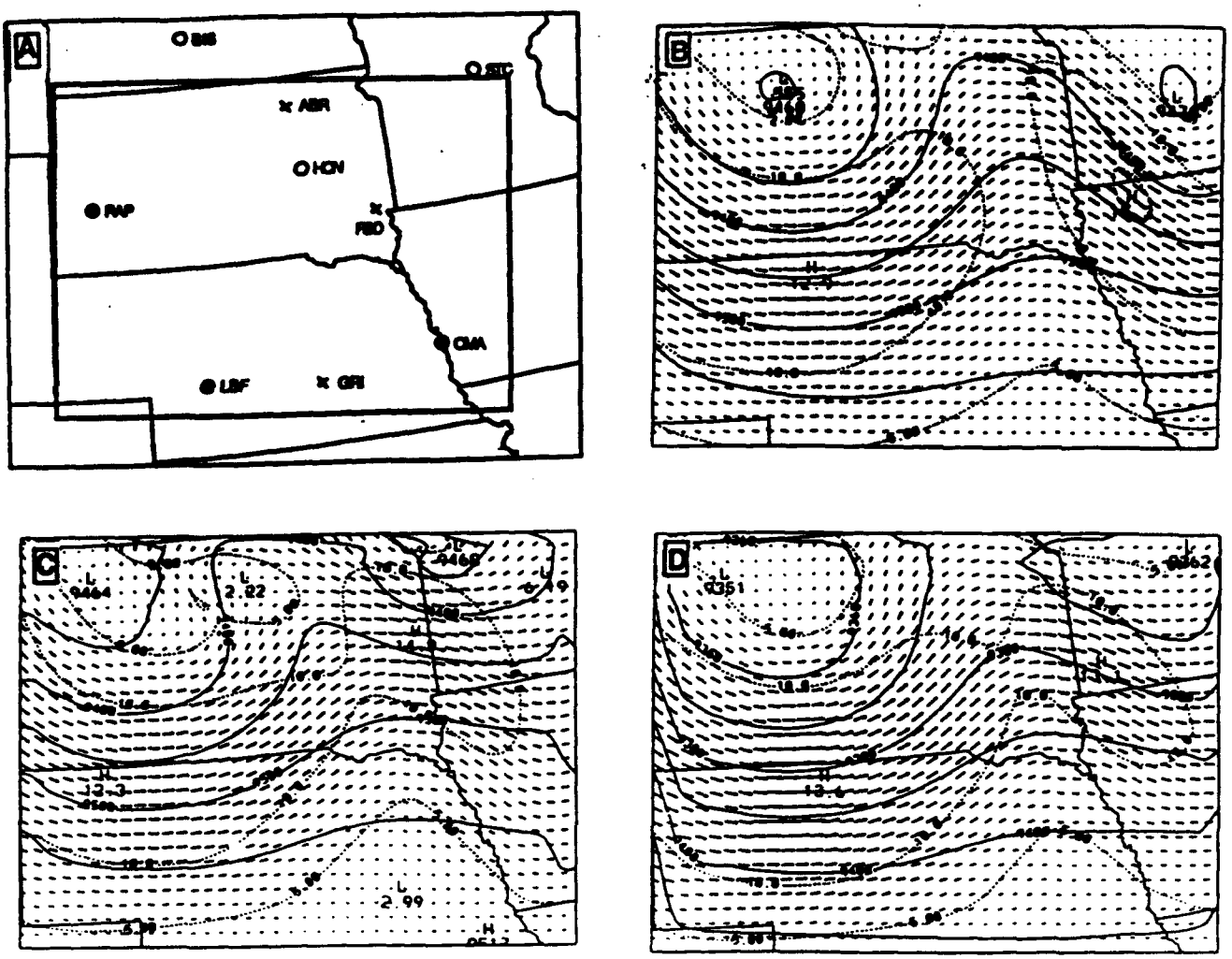

Figure 3-3 Results from a lateral boundary condition test experiment with the three-dimensional version of MASS: (a) depiction of the small (inner box) and large (outer box) domains used in the experiment and 300 mb heights (solid lines, m), wind vectors and isotachs (dashed lines, m s^{-1}) six hours after the initialization time for: (b) the control simulation; (c) the simulation with sponge boundary conditions; and (d) the simulation with radiative boundary conditions.

4. Improvements in Surface Physics

During the course of this project, extensive changes to the model's surface parameterization schemes were made. Significant changes to the surface energy budget scheme included an improved evapotranspiration scheme and a better treatment of the subsoil temperature. A completely revamped longwave and shortwave radiation scheme was implemented, and a formulation for solar radiation on sloping terrain surfaces was added. The planetary boundary layer scheme was cleaned up and recoded, and a much more sophisticated surface hydrology scheme was implemented. The improvements in several of these areas will be discussed in the following sections.

4.1 Evapotranspiration Scheme

It has long been recognized that the evaporation over land surfaces is highly variable in both space and time, and that it depends heavily on local surface characteristics, such as vegetation cover and structure, which are not well understood at scales larger than the microscale. The term evapotranspiration has been coined to describe the combined effects of evaporation from various surfaces and transpiration from plant canopies. Dr. Joe Russo of ZedX, Inc. served as a consultant to this project to help develop a comprehensive evapotranspiration scheme for the MASS model. There are separate formulations for transpiration, and for evaporation from bare soil and from the cover reservoir, which represents water on the surface of plants and other surfaces which consists of intercepted rainfall.

The latent heat flux, E_{tot}, represents the effects of evapotranspiration from three separate sources:

$$E_{tot} = E_{veg} + E_{soil} + E_{cov} \quad . \tag{4-1}$$

E_{veg} is the transpiration from plants, E_{soil} is the evaporation directly from the top layer of soil, and E_{cov} is the cover layer evaporation, which occurs as a result of rainfall interception. An empirical formulation for E_{veg} has been developed which scales the actual transpiration to the potential evaporation and the deep layer soil moisture. When the evaporative demand is low, vegetation can transpire freely over a wide range of soil moisture conditions. As the evaporative demand increases however, the actual transpiration becomes more sensitive to soil moisture conditions, representing in a simple way the process of stomatal closure in plants. The transpiration rate is parameterized as:

$$E_{veg} = \min \begin{cases} (1 - \sigma_i)\sigma_v \, k_v \, E_p \\ R_{s\downarrow} \end{cases} \quad . \tag{4-2}$$

E_{veg} is not allowed to exceed the incoming solar radiative flux density, acknowledging the direct relationship between the absorption of solar radiation and transpiration through the common mechanism of stomatal control. E_p is the potential evapotranspiration, given by

$$E_p = \rho_a L_v C_H V_a (q_s(T_g) - q_a) \quad . \tag{4-3}$$

where L_v is the latent heat of vaporization, $q_s(T_g)$ is the saturation vapor mixing ratio at the surface temperature, and q_a is the atmospheric vapor mixing ratio near the surface. The empirical transpiration coefficient is given by

$$k_v = \frac{1}{1 + a_1 \exp\left[a_2\left(\frac{w_2}{w_{sat}}\right)\right]}, \qquad (4\text{-}4)$$

where a_1 and a_2 are

$$a_1 = \exp\left(-.41457 + 2.5527\ E_* - 10.134\ E_*^2 + 41.894\ E_*^3\right),$$
$$a_2 = -27.914 + 80.100\ E_* - 95.607\ E_*^2 + 8.8831\ E_*^3. \qquad (4\text{-}5)$$

E_* is a normalized transpiration,

$$E_* = \min\left\{\frac{E_p / E_{max}}{1.3}\right., \qquad (4\text{-}6)$$

where E_{max} is a transpiration rate which is taken to be nearly the maximum allowable rate. E_{veg} is not constrained to be only positive. Figure 4-1 shows the variation of transpiration with both evaporative demand (potential evaporation) and soil moisture. One of the essential characteristics of the scheme is that it mimics the tendency of plants to progressively restrict evaporation (by stomatal closure) with increasing evaporative demand, sometimes even in the presence of abundant soil moisture.

There are several serious uncertainties concerning transpiration. First, different species of plants can react very differently to similar conditions. Since comprehensive digital data on the geographical and seasonal distribution of species is hard to find, this is a serious problem. Second, many of the transpiration studies which have been conducted have been performed with plants isolated in an artificial (experimental) environment, and it is not clear how to extrapolate the transpiration behavior of individual plants to the characteristics of a complex (perhaps very heterogeneous) plant canopy.

The bare soil evaporation is a modification of the formulation of Noilhan and Planton (1989):

$$E_{soil} = \sigma_b\,(1 - \sigma_v)\,\rho_a\,L_v\,C_H\,V_a\left[h_u\,q_s\,(T_g) - q_a\right], \qquad (4\text{-}7)$$

where σ_b is the fraction of the non-vegetated portion of the model grid box which is covered by bare soil, which is considered to be a function of land use type. The relative humidity at the ground surface is given by

$$h_u = \begin{cases} 0.5\left[1 - \cos\left(\frac{w_1}{w_{fc}}\pi\right)\right], & \text{if } w_1 < w_{fc}, \\ 1, & \text{if } w_1 \geq w_{fc}, \end{cases} \qquad (4\text{-}8)$$

where w_{fc} is the field capacity, which is defined as $0.75\ w_{sat}$.

The cover evaporation is the evaporation of water which is stored in a cover reservoir, made up of snowfall, dewfall and intercepted rainfall. As will be discussed in the hydrology section, the interception parameterization of Mahfouf and Jacquemin (1989) is used. If there is intercepted rainfall present, then the fraction of the grid covered by intercepted rainfall is assumed to be

$$\sigma_i = \left(\frac{w_c}{w_{cmax}}\right)^{2/3}, \qquad (4\text{-}9)$$

where w_c is the interception reservoir and w_{cmax} is the maximum amount of water allowed. The cover evaporation is then

$$E_{cov} = \min \begin{cases} \dfrac{\rho_w L_v w_c}{\Delta t} \\ \sigma_i \sigma_v E_p \end{cases}, \qquad (4\text{-}10)$$

where the top expression represents the evaporation rate which would occur if all of the intercepted moisture evaporated in one surface energy budget timestep, and the lower expression is a rate which is calculated assuming that cover moisture can evaporate freely at the potential rate over vegetated areas. In the presence of intercepted water, transpiration is reduced by the factor $(1-\sigma_i)$, following Mahfouf and Jacquemin (1989). If the water vapor gradient is reversed, then condensation (dew formation) is allowed to occur at a rate of $\sigma_v E_p$, with the constraint that the cover reservoir cannot exceed a maximum value.

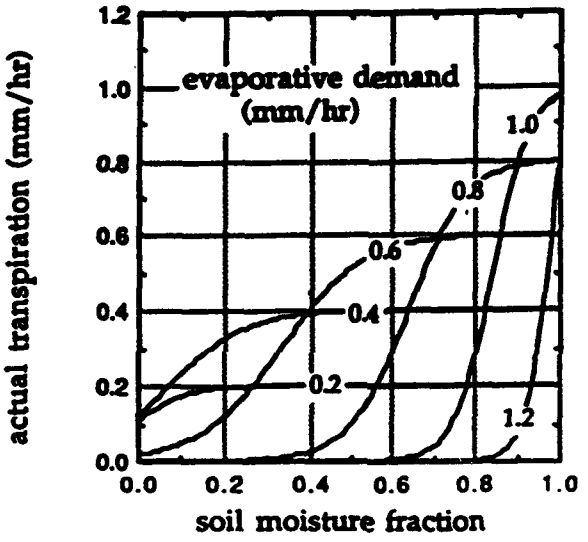

Figure 4-1 Transpiration curves as a function of soil moisture for several values of evaporative demand. All transpiration units are mm/hr. The soil moisture fraction is the fractional soil saturation, not the volumetric soil moisture fraction.

4.2 *Treatment of Subsoil Temperature*

One longstanding model initialization problem is that a routine data source for surface temperature ("skin temperature", the actual temperature of the ground surface, not the near-surface atmospheric temperature) is not available. The traditional solution to the problem has been to assume that the surface temperature is equal to the atmospheric temperature, but that assumption is clearly incorrect much of the time. To test the sensitivity of the scheme to initial surface temperature, a series of runs were made in which the atmospheric temperature remained constant, and the surface temperature varied from 255 to 280 K. In these runs, the subsoil temperature was set equal to 5 K less than the surface temperature. Figure 4-2a shows the evolution of the low level atmospheric temperature over a 24 hr period for two initial surface

temperatures. There is a dramatic difference in the nighttime low temperature between the two runs, even larger than the difference between the initial surface temperatures. This suggests that the scheme can be very sensitive to the initial surface temperature. A second series of runs with the same initial variation of surface temperature but with the subsoil temperature kept constant at 262.5 K is shown in Figure 4-2b. The difference in the nighttime low between the two runs has been significantly reduced, and there is no significant difference in daytime highs. This indicates that it is the variation in subsoil temperatures which produces most of the difference in Figure 4-2a, not the variation of surface temperatures. The reason for this is that the ground heat flux term in the surface energy budget can be very significant, even over fairly short periods. A method of initializing the subsoil temperature from an average atmospheric temperature over the previous several days was developed and used in all of the simulations for this project.

The ground heat flux term, H_m, is given by

$$H_m = \frac{2\pi}{\tau} (T_g - T_2) , \qquad (4\text{-}11)$$

where τ is the number of seconds in one day and T_2 is the subsurface "restoring" temperature in the force-restore method. This formulation allows T_2 to vary with the surface temperature, on the time scale of about one day. The initialization of T_2 is not obvious; one approach is to define it as the average temperature over the previous few days.

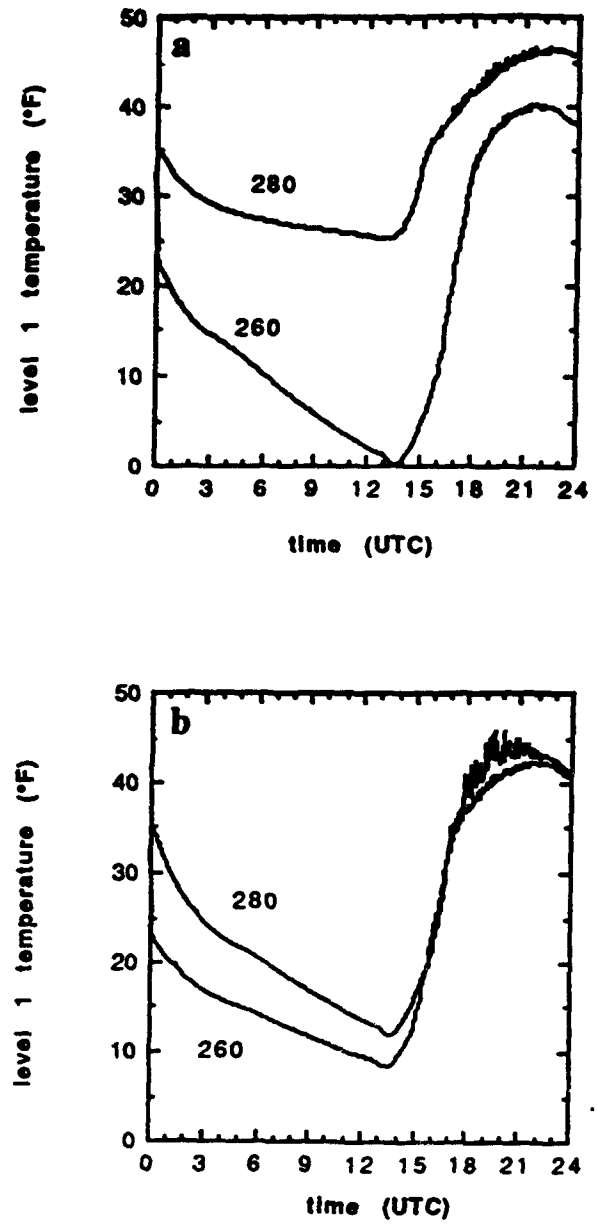

Figure 4-2 Diurnal variation of low level temperature for two one-dimensional simulation initialized with the same analytical vertical temperature profile, surface temperatures of 260 and 280 K, and: (a) subsoil temperatures of 255 and 275 K, respectively, and (b) subsoil temperatures of 262.5 K for both simulations.

4.3 *Solar Radiation on Sloping Surfaces*

The effect of terrain slope was added to the calculation of incoming solar radiation. The method follows the discussion in Pielke (1984). The solar zenith angle, Z, is replaced in the incoming shortwave term in the radiation budget with a modified zenith angle, Z', which is the angle between a vector normal to the terrain slope and the solar position.

The solar zenith angle (Z) is defined as

$$\cos Z = \cos \varphi \cos \delta \cos h + \sin \delta \sin \varphi \ , \qquad (4\text{-}12)$$

where φ is latitude, δ is the solar declination angle, and h is the hour angle. If there is a local terrain slope, then the following calculations are made to incorporate the effect. If the magnitude of the local slope is

$$\alpha_z = \left[\left(\frac{\partial z_g}{\partial x}\right)^2 + \left(\frac{\partial z_g}{\partial y}\right)^2\right]^{1/2} , \qquad (4\text{-}13)$$

where z_g is the terrain height. The azimuth of the local slope is

$$\gamma_z = \frac{\pi}{2} - \tan^{-1}\left(\frac{\partial z_g/\partial y}{\partial z_g/\partial x}\right) , \qquad (4\text{-}14)$$

and the solar azimuth (which varies from $-\pi$ to $+\pi$, with south being zero and west of south being the positive direction) is

$$\gamma_s = \sin^{-1}\left(\frac{\cos \delta \sin h}{\sin Z}\right) . \qquad (4\text{-}15)$$

The zenith angle corrected for slope is then

$$\cos Z' = \cos \alpha_z \cos Z + \sin \alpha_z \sin Z \cos (\gamma_s - \gamma_z) . \qquad (4\text{-}16)$$

Care must be taken that no division by zero occurs in (4-14) and (4-15).

To show the effect of slope on incoming solar radiation, the differences between the radiation received on level terrain and surface sloping (α = .05) to the east and south at 32°N latitude at both solstices is shown in Figure 4-3. The differences are large enough to be significant in areas of mountainous terrain, especially when the model is used at high resolution (e.g. 10 km). Although this formulation is a part of the MASS model, no three-dimensional simulations with the terrain slope effects were performed, because a high resolution terrain dataset has not yet been incorporated into the preprocessor. At the end of the project, a 1 km terrain dataset which would allow for reasonable slope calculations for high resolution MASS grids had been obtained, and a relatively modest effort is needed to integrate it into the preprocessor.

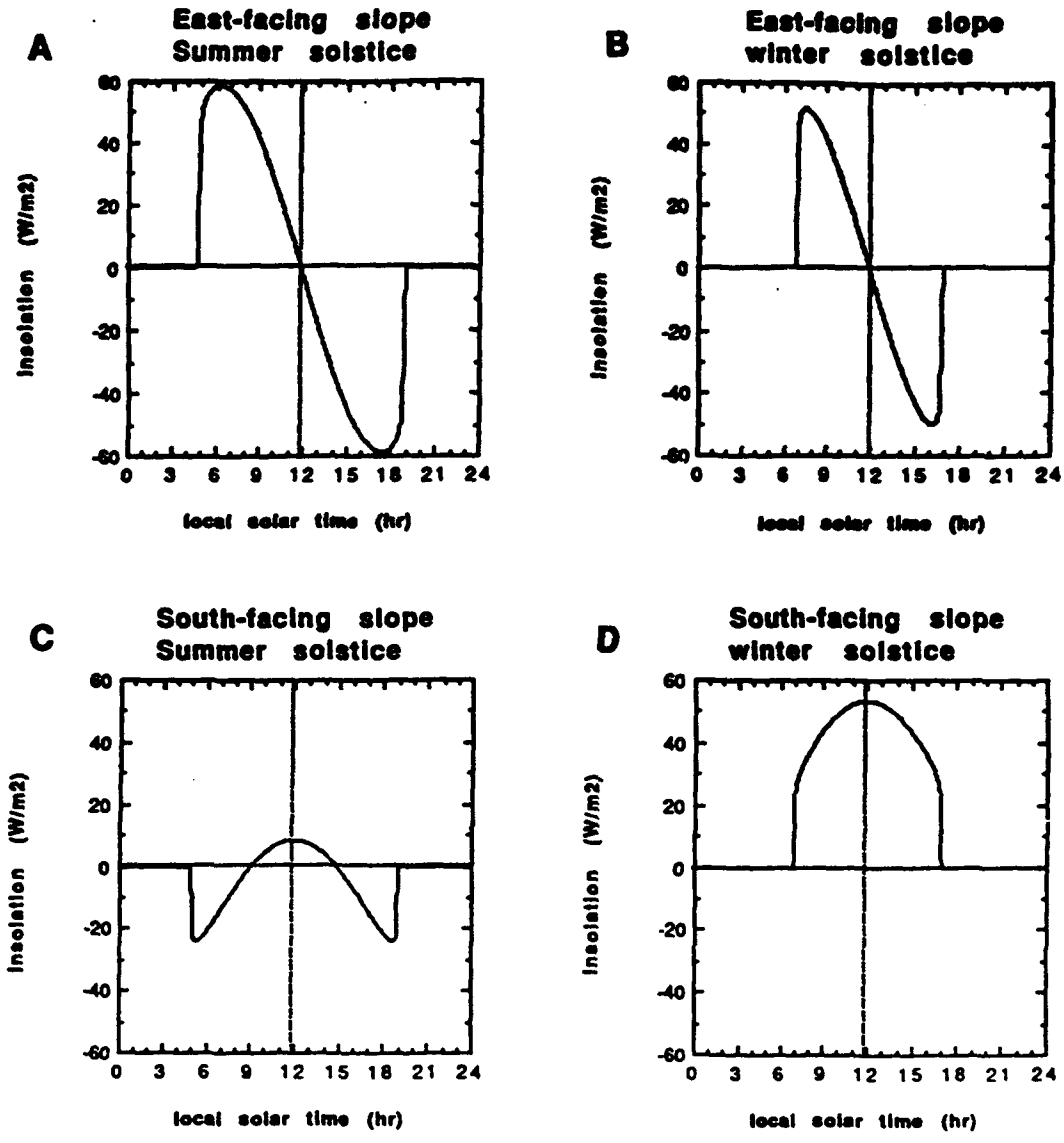

Figure 4-3 The effect of sloping surfaces on incoming solar radiation. The difference in direct shortwave radiation (W m^{-2}) between a surface of slope .05 and a flat surface (sloping – flat) is plotted vs. time of day for an east-facing slope at the (a) summer and (b) winter solstices, and for a south-facing slope at the (c) summer and (d) winter solstices. All plots assume a dry cloudless day at a latitude of 32 N.

4.4 *Hydrology Scheme*

As a part of the effort to improve the model's evapotranspiration scheme, it was necessary to construct a complete hydrology framework. The soil hydrology scheme is based on the model of Mahrt and Pan (1984). The soil is divided into two layers – a shallow 5 cm layer at the surface and a layer from 5 cm to 30 cm deep, which is assumed to contain the majority of plant roots. An additional reservoir of moisture is parameterized, a "cover" moisture reservoir which retains intercepted rainfall. The model structure and processes considered are depicted in Figure 4-4. Each model surface grid box has been assigned a land use type, a soil type, and a value of fractional vegetation.

4.4.1 Soil moisture budgets

With the notation that layer 1 is the shallow layer, and layer 2 is the deep layer, soil moisture budgets for the two layers are

$$\begin{aligned} \frac{\partial w_1}{\partial t} &= \frac{1}{z_1}(\mathrm{INFIL} - \mathrm{DIFF} - \mathrm{CON}_1 - E_{soil}) \ , \\ \frac{\partial w_2}{\partial t} &= \frac{1}{(z_2 - z_1)}(\mathrm{DIFF} - \mathrm{CON}_1 - \mathrm{CON}_2 - E_{veg}) \ , \end{aligned} \tag{4-17}$$

where w_1 and w_2 are volumetric soil moisture fractions for the two layers, and z_1 and z_2 are the depths of the bottom of each layer (5 cm and 30 cm). All of the terms in parentheses in (4-17) have units of m s^{-1}. Many of the expressions for the terms are from McCumber and Pielke (1981).

The first term in the w_1 equation is the *infiltration of precipitation into the top layer of* soil. The infiltration is the precipitation rate minus the rainfall interception:

$$\mathrm{INFIL} = \mathrm{PRECIP} - \mathrm{ICEPT} \ . \tag{4-18}$$

The infiltration rate is constrained to not exceed a maximum rate, which is related to the properties of the soil and the degree of saturation of the soil:

$$\mathrm{INFIL}_{max} = \frac{D_{sat}(w_{sat} - w_1)}{\frac{z_1}{2}} + K_{sat} \ , \tag{4-19}$$

where

$$D_{sat} = -\frac{b\, K_{sat}\, \psi_{sat}}{w_{sat}} \ , \tag{4-20}$$

and b, K_{sat} and ψ_{sat} are functions of soil type.

Diffusion between layers assumes that the soil moisture values occur at the midpoint of the layers, with a linear vertical gradient:

$$\frac{\partial w}{\partial z} = 2\frac{w_1 - w_2}{z_2}\,, \tag{4-21}$$

where the diffusivity is calculated for the layer which is the most moist, following Mahrt and Pan:

$$D = \begin{cases} -\dfrac{b\,K_{sat}\,\psi_{sat}}{w_1}\left(\dfrac{w_1}{w_{sat}}\right)^{(b+3)}, & w_1 \geq w_2 \\ -\dfrac{b\,K_{sat}\,\psi_{sat}}{w_2}\left(\dfrac{w_2}{w_{sat}}\right)^{(b+3)}, & w_2 > w_1 \end{cases} \tag{4-22}$$

The diffusion term is then

$$DIFF = D\frac{\partial w}{\partial z}\,. \tag{4-23}$$

There are conductivity terms for both layers:

$$\begin{aligned} CON_1 &= K_{sat}\left(\frac{w_1}{w_{sat}}\right)^{2b+3}\,, \\ CON_2 &= K_{sat}\left(\frac{w_2}{w_{sat}}\right)^{2b+3}\,, \end{aligned} \tag{4-24}$$

but if the deep soil layer is more moist, CON_1 is set equal to CON_2. The evaporation from bare soil (E_{soil}) and transpiration (E_{veg}) are calculated in the surface energy budget and passed into the hydrology scheme.

4.4.2 Rainfall interception and cover moisture reservoir

The parameterization for rainfall interception follows that of Mahfouf and Jacquemin (1989). The prognostic equation for the cover moisture is

$$\frac{\partial w_c}{\partial t} = ICEPT - E_{cov}\,, \tag{4-25}$$

where w_c is the cover moisture with units of length, which can be thought of as the depth of moisture on the surface. The interception term is given as

$$ICEPT = \max\begin{cases}\sigma_v\,PRECIP \\ c_{imin}\,PRECIP\end{cases}, \tag{4-26}$$

where σ_V is the fractional vegetation, PRECIP is the precipitation rate, and where c_{imin} is a minimum interception constant, which is a function of land use type. c_{imin} is nonzero for those land use types which are assumed to intercept rainfall, even when the NDVI is very low, such as forests and rangeland. For example, deciduous forests may have low NDVI in the winter, but rainfall interception will still take place even with all the leaves gone, although at a lower rate.

The expression for the cover layer evaporation is given in (4-10). The moisture in the cover reservoir is not allowed to exceed a maximum value, parameterized as

$$w_{cmax} = \begin{cases} \sigma_v \, c_i \, h_{max} , & \text{if } \sigma_v > 0 \\ 0.01 \, c_i \, h_{max} , & \text{if } \sigma_v = 0 \end{cases} , \qquad (4\text{-}27)$$

where c_i is a land use dependent constant, which can vary from 0 to about 3 for forested land. This parameter replaces the leaf area index in Mahfouf and Jacquemin. h_{max} is a maximum reservoir value; the value of 0.2 kg m^{-2} from Mahfouf and Jacquemin is used.

4.4.3 Snow cover

A parameterization for the effects of snow cover follows that of Segal et al. (1991). The most important effect is a strong increase in the shortwave albedo. An expression for the albedo is

$$\alpha = 0.5 \, (\alpha_{v0} + \alpha_{i0}) + 0.32 \, f(Z) , \qquad (4\text{-}28)$$

where α_{v_0} is the albedo for solar radiation with a wavelength ≤ 0.7 mm (0.95), and α_{i0} is the albedo for solar radiation with wavelengths > 0.7 mm. The last term represents the additional reflectance of snow surfaces at large solar zenith angles:

$$f(Z) = \begin{cases} 0. & , Z \leq 60^\circ \\ \frac{1}{b}\left(\frac{b+1}{1+2b\cos Z} - 1\right) & , 60^\circ < Z < 80^\circ \\ \frac{1}{b}\left(\frac{b+1}{1+2b\cos 80^\circ} - 1\right) & , 80^\circ \leq Z \end{cases} , \qquad (4\text{-}29)$$

where Z is the zenith angle, and b is a constant set to 2, as in Segal, et al. Several other surface variables are changed for snow cover, superseding values otherwise derived from land use type. The heat capacity is set to 9.305×10^{-5} K m^2 J^{-1}, a value for fresh snow from Oke (1978). The longwave emissivity is set to 0.99, also from Oke. The roughness length is set to 1×10^{-4} over some land use type (agricultural land, rangeland, and barren land), but is unchanged for other types (urban land, forests, open water, wetlands) on the assumption that large obstacles dominate the roughness length. With snow cover, the fractional vegetation is set to zero, so that any vegetative effects are eliminated.

To test the snow cover parameterization, a similar series of runs were made. Figure 4-5 demonstrates that snow cover effectively decouples the atmosphere from the soil temperature due to the insulating effect of a complete snow cover, and that the initial surface temperature is unimportant, since an equilibrium is reached very quickly due to the low heat capacity of snow.

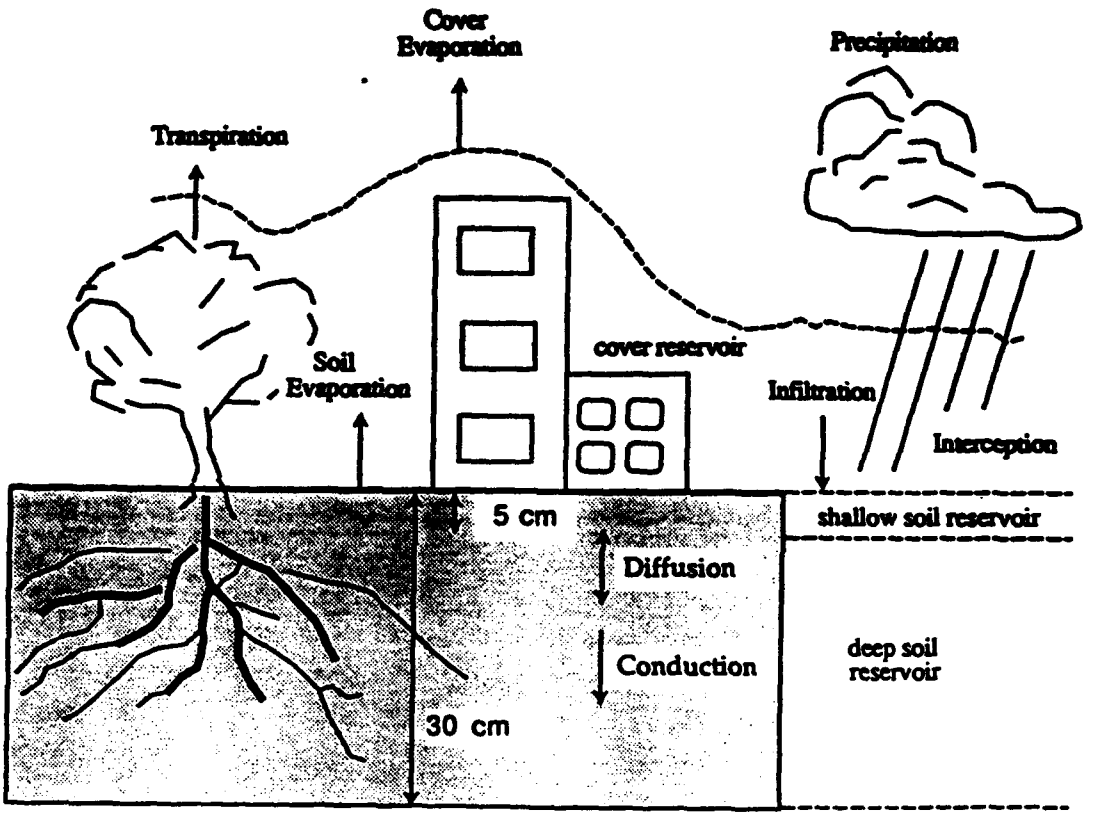

Figure 4-4 Schematic diagram of the MASS model hydrology scheme.

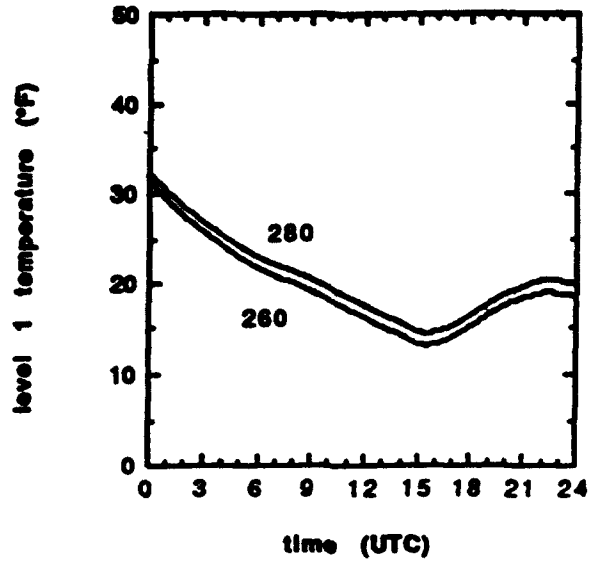

***Figure 4-5** Diurnal variation of low level temperature for two one-dimensional simulation initialized with the same analytical vertical temperature profile, surface temperatures of 260 and 280 K, and with a complete snow cover.*

5. Positive Definite Transport Scheme

When simulating moist processes, it is imperative to resolve strong humidity and cloud water, cloud ice, rain water and snow gradients. Version 5 of the MASS model utilizes a split-explicit time integration scheme (a forward-backward scheme for inertial-gravity modes and the Adams-Bashforth scheme for the advective modes) and fourth-order accurate advection and diffusion operators. Despite these measures, the forecast fields still suffer from false numerical dispersion (Gibbs oscillations) and produce small negative amounts of water vapor and cloud water, cloud ice, rain water and snow. In practice, these artificial, high frequency ripples are filtered out of the solution by the lateral diffusion operator. Any residual negative values of the mixing ratio of these quantities were then reset to a small positive amount. However, this indiscriminately smears out the solution so that the fine scale structure in the field is often lost. This problem was addressed during Phase II by implementing a positive-definite non-diffusive advection scheme into the simulation model.

5.1 Review of Candidate Schemes

Three numerical techniques, each developed for modeling fluid flows characterized by strong shocks and discontinuities, were considered as potential candidates for implementation: (1) Flux-Corrected Transport (FCT) (Boris and Book, 1973; Zalesak, 1979), (2) the Smolarkiewicz Multidimensional Positive Definite Advection Transport Algorithm (MPDATA) scheme (Smolarkiewicz, 1983a), and (3) the Piecewise Parabolic Method (PPM) (Carpenter et al., 1990). Each of these techniques is characterized by a lack of numerical dispersion and a low level of inherent diffusion. To illustrate the concepts behind these three numerical methods, consider the continuity equation written in flux form:

$$\frac{\partial \varphi}{\partial \tau} + \vec{\nabla} \cdot (\vec{V}\varphi) = 0 \qquad (5\text{-}1)$$

or

$$\frac{\partial \varphi}{\partial t} + \vec{\nabla} \cdot \vec{F} = 0 \qquad (5\text{-}2)$$

where φ is the material substance which is to be advected through the model domain and F is the flux of this substance.

The flux-corrected transport technique separates the flux divergence calculation into two steps. First, a time-advanced solution is calculated using a low-order diffusive scheme, typically first-order upstream finite differencing. Then, in an attempt to restore the shape of the mass field to its pre-diffused form, antidiffusive fluxes are applied, which are defined to be the difference between the high (usually fourth or sixth)-order "ripple producing" fluxes and the original diffusive fluxes. Adding these antidiffusive fluxes at full strength is equivalent to replacing the low-order fluxes by those from the high-order scheme. If such a prescription creates new extrema (peaks or valleys) in the solution, then the antidiffusive fluxes are systematically reduced. Thus, it is possible to re-concentrate the mass at each grid point without causing overshooting. Because FCT virtually eliminates numerical diffusion, it is extremely effective in advecting even cusp-like features such as shocks of square waves without a serious degradation in their form. Mattocks and Bleck (1986) have successfully used FCT to prevent the generation of negative

layer thicknesses in an isentropic channel model and to accurately locate the intersection of the isentropes with the ground.

Smolarkiewicz (1983a, 1983b) developed a positive definite advection scheme which has small implicit diffusion and a lower computational cost than FCT. The scheme was further refined by Smolarkiewicz and Clark (1986) and was given the name of Multidimensional Positive Definite Advection Transport Algorithm (MPDATA). Smolarkiewicz realized that the conventional one-sided, upstream-differenced analog of the continuity equation (written in flux form for one spatial dimension):

$$\frac{\partial \varphi}{\partial t} = -\frac{\partial F}{\partial x} \quad \text{where} \quad F_{i+\frac{1}{2}} = \begin{cases} u_{i+\frac{1}{2}} \varphi_i \ , & \text{if} \quad u > 0 \\ u_{i+\frac{1}{2}} \varphi_{i+1} \ , & \text{if} \quad u < 0 \end{cases} \tag{5-3}$$

is actually a centered difference representation of the advection/diffusion equation:

$$\frac{\partial \varphi}{\partial t} = -\frac{\partial}{\partial x}(u\varphi) + \frac{\partial}{\partial x}\left(K_{impl} \frac{\partial \varphi}{\partial x}\right) \tag{5-4}$$

where K_{impl} is an "implied" diffusivity. Smolarkiewicz counteracts this implied diffusivity, without sacrificing positive definiteness, by following each advection step with a "negative diffusion" or corrective step:

$$\frac{\partial \varphi}{\partial t} = \frac{\partial}{\partial x}\left(-K_{impl} \frac{\partial \varphi}{\partial x}\right). \tag{5-5}$$

In order to ensure that the solution remains positive-definite, this can be re-formulated as an advection equation:

$$\frac{\partial \varphi}{\partial t} = -\frac{\partial}{\partial x}(u_d \varphi) \ , \tag{5-6}$$

with the "antidiffusive advection velocity" set to zero when the transported material is completely depleted at a grid point:

$$u_d = \begin{cases} -\dfrac{K_{impl}}{\varphi} \dfrac{\partial \varphi}{\partial x} & \text{if} \quad \varphi > 0 \\ 0 & \text{if} \quad \varphi = 0 \end{cases} . \tag{5-7}$$

Smolarkiewicz noted that the restorative, antidiffusive effect of the second step can be enhanced by multiplying the advection velocity by a "correction coefficient" slightly larger than 1 or by repeating the correction step during each iteration. He presented impressive results from solid-body rotation simulations for the multidimensional and time-splitting forms of the equations. The original mass field retained its shape while sharp gradients were maintained.

The third numerical technique which was considered for implementation into the MASS model was originally developed for simulating astrophysical phenomena. Known as the piecewise parabolic method (PPM), it consists of a rather unconventional approach: dependent variables are represented by monotonic parabolas fit to each grid interval instead of discrete grid point values. Unlike standard curve-fitting and global spectral techniques, each parabola is uniquely constructed for a specific grid box and each grid interface is considered to be a

discontinuity. Nonlinear fluxes across grid boundaries can therefore be calculated explicitly from the analytic (parabolic) functions using Riemann integration. An eloquent description of the method is provided by Carpenter et al. (1990). The authors first present an example which shows how parabolas are constructed for an analytic transcendental function (see Figure 5-1).

Essentially, this procedure requires that values for the three coefficients (φ_0, φ_1, φ_2) be determined so that a unique quadratic representation of the dependent model variable:

$$\varphi(x) = \varphi_0 + \varphi_1 x + \varphi_2 x^2 \qquad (5\text{-}8)$$

can be defined for each grid box. The first step is to generate lower-order piecewise linear functions by calculating slopes at the left edge, center, and right edge of each grid interval, then taking the slope with the smallest magnitude. If the grid box or "zone" average of the variable:

$$\langle\varphi\rangle = \frac{1}{\Delta x}\int_{x-\Delta x/2}^{x+\Delta x/2} \varphi\, dx \qquad (5\text{-}9)$$

is an extremum, then the slope is set to zero. After the set of connected lines is assembled, the second step is to construct a first-guess parabola with a unique cubic curve fit from the neighboring zone averages and slopes which surround the left and right edges of the grid interval. The first, second, and third derivatives of the provisional solution are then calculated to determine whether any "contact discontinuities" (hydraulic jumps) exist within each zone. If some are found, then the parabola is "steepened" to avoid smearing out sharp gradients. Finally, any undershooting or overshooting is eliminated by flattening out the parabola, if necessary, to prevent the creation of new extrema and preserve the monotonicity (positive definiteness) of the solution.

A schematic which shows how the PPM advection process works is displayed in Figure 5-2. First, zone (grid box) averages are determined by integrating the initial step function distribution over the width of each grid interval. Parabolas are constructed within each zone, as previously described, then the entire form is translated to the right during the advection. Next, the two parabolas which now lie within a given zone are integrated analytically to determine the new zone averages (step function distribution). These new zone averages are used as initial data for the subsequent time step, in which a new piecewise parabolic representation is calculated. Like its progenitors, the piecewise parabolic method is positive definite, retains the integrity of steep gradients, and is characterized by a nearly complete lack of computational diffusion. In addition, PPM yields solutions of similar accuracy at half the spatial resolution when compared with conventional finite difference methods.

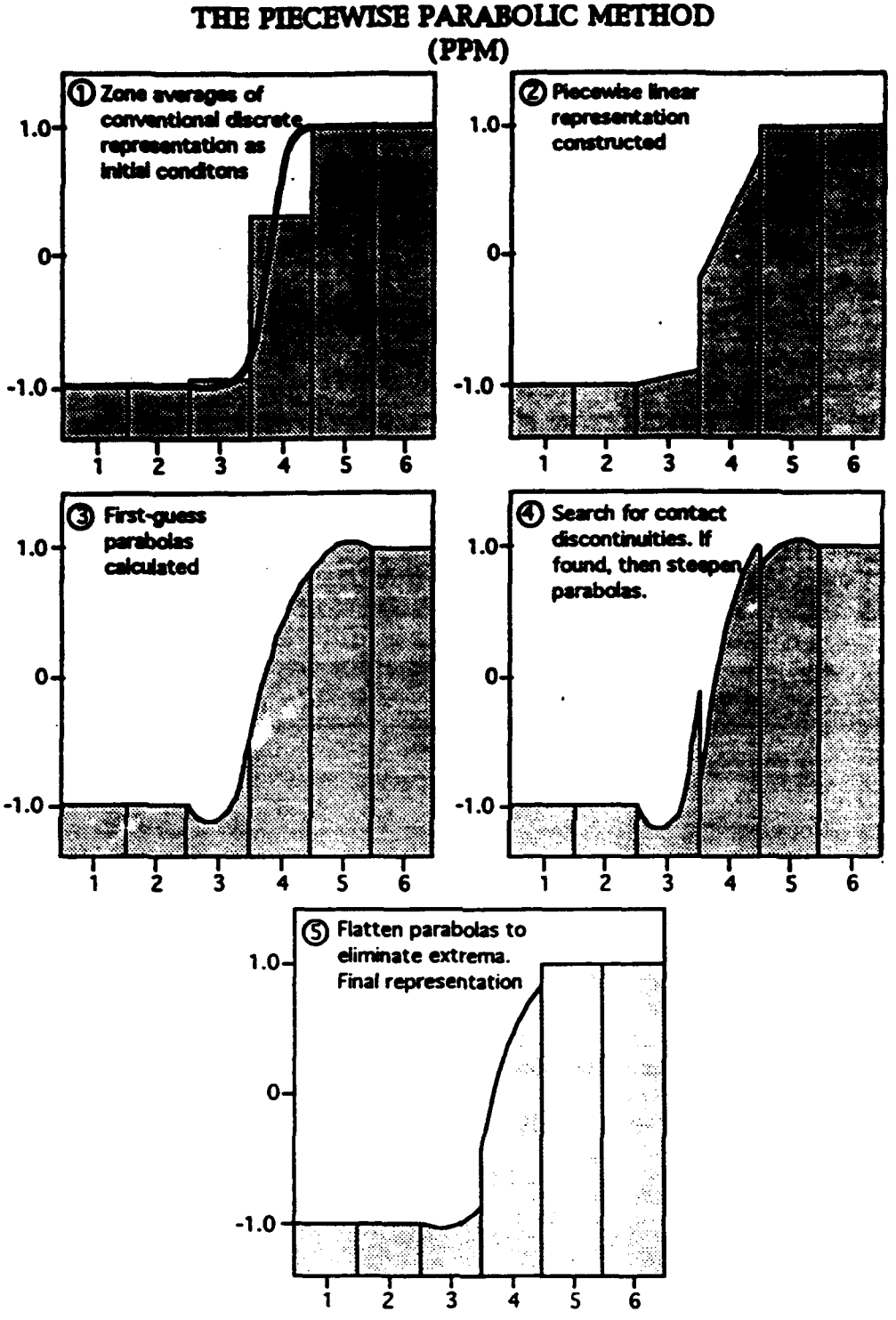

Figure 5-1. A graphical illustration which shows how unique parabolas are constructed for each grid box to numerically represent an analytical solution in the piecewise parabolic method (PPM). In this example the analytical solution is a hyperbolic tangent function. It is denoted by the heavy black line in the first panel of the figure (after Carpenter et al., 1990).

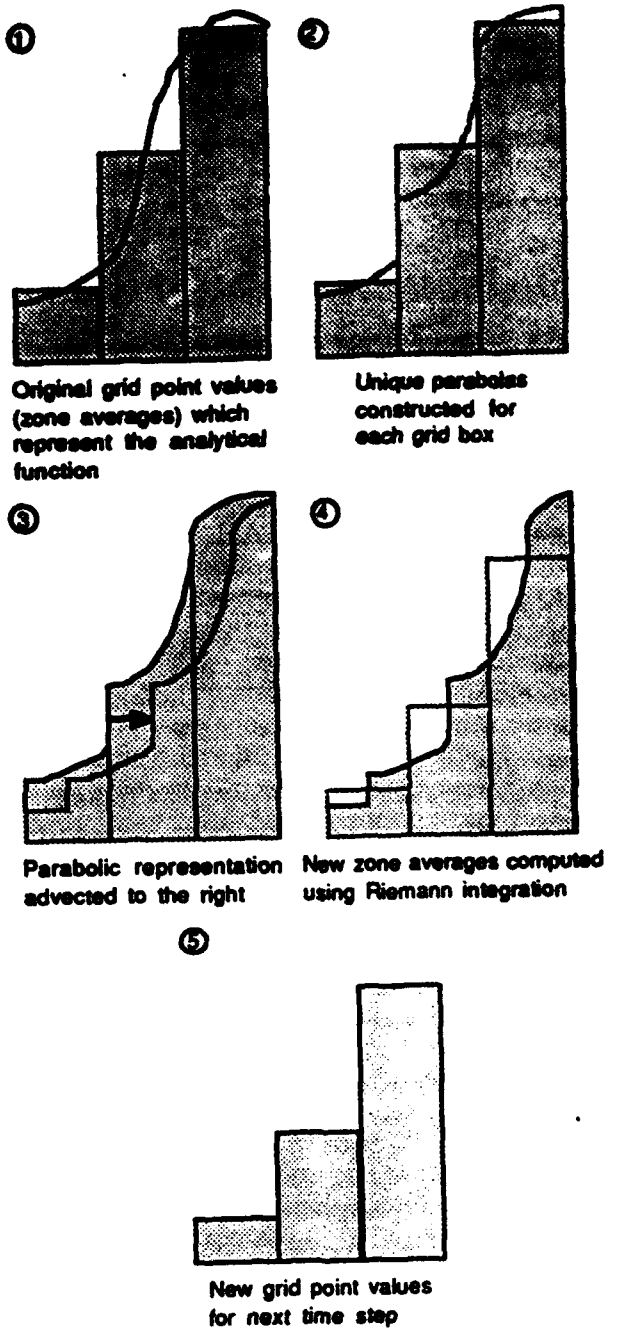

Figure 5-2. A schematic which illustrates how the piecewise parabolic method(PPM) advection process works. The initial analytical function is denoted by the heavy black line in the first panel of the figure (after Carpenter et al., 1990).

During the Phase II project, a survey of the scientific literature revealed that PPM was too computationally expensive and too time-consuming to code from scratch. Experience with the flux-corrected transport method (Mattocks and Bleck, 1986), a second possible choice, had shown it to be extremely effective in advecting shock waves or other contact discontinuities with minimal degradation in their form. However, FCT sometimes generates artificially steep gradients in regions where none should exist, typically at the leading edge of the waveform. Other numerical modelers, most notably Smolarkiewicz (1983a, 1983b), are critical of FCT because it can become computationally expensive, depending on how well the flux-limiting decision process is formulated. Therefore, MESO selected the MPDATA scheme as the positive-definite advection scheme to be implemented in the MASS model.

5.2 One and Two Dimensional Tests of MPDATA

Before the MPDATA scheme was implemented into the three-dimensional version of the MASS model, a number of one-dimensional and two-dimensional experiments were executed to test and evaluate the scheme under a simple set of conditions. The objective of these experiments was to: (1) acquire a comprehensive understanding of the scheme's performance, (2) determine the computational performance of each of the scheme's several options, and (3) ensure that the computer code used to implement the scheme was functioning properly.

The testing and evaluation of the MPDATA scheme began with the acquisition of the FORTRAN-77 code for a one-dimensional version of the MPDATA scheme from Dr. Piotr Smolarkiewicz at the National Center for Atmospheric Research (NCAR). A driver test program which advects a square-wave shaped mass perturbation through a domain ad-infinitum using cyclic lateral boundary conditions was written. The MPDATA code was then modified to increase and measure its computational efficiency. The Smolarkiewicz code permits the user to: (1) select the numerical order of the advection scheme (from a 1st-order donor cell scheme up to a 3rd-order MPDATA scheme); (2) specify whether a monotonicity constraint should be enforced; and (3) decide whether a special correction for divergent flows should be applied. The performance of the range of configurations was tested by executing one-dimensional advection experiments on an Apple Macintosh II microcomputer. The results of the simple advection experiments after 5000 timesteps are shown in Figure 5-3. It can be seen that the mass field was severely diffused and the amplitude of the square wave was reduced to 46% of its original amplitude when the mass was transported with an upstream-differencing (donor cell) scheme. The application of the higher order MPDATA scheme corrected these problems. The gradients of the mass field were sharpened dramatically by the higher order formulations. However, both the 2nd-order and 3rd-order versions of the scheme generated a square wave with an amplitude that was about 6% higher than its original value. Enforcing monotonicity on the 3rd-order solution eliminated the high frequency ripples and the overshooting. The application of this constraint resulted in less than a .08% error in the amplitude after 5000 timesteps. However, the computational price for the increased accuracy was substantial. The execution was 2.5 times slower with the monotonicity constraint than in the case of the 3rd-order scheme without the monotonicity constraint. A similar reduction in computational efficiency was also noted when the accuracy of the numerical scheme was increased from 2nd-order to 3rd-order.

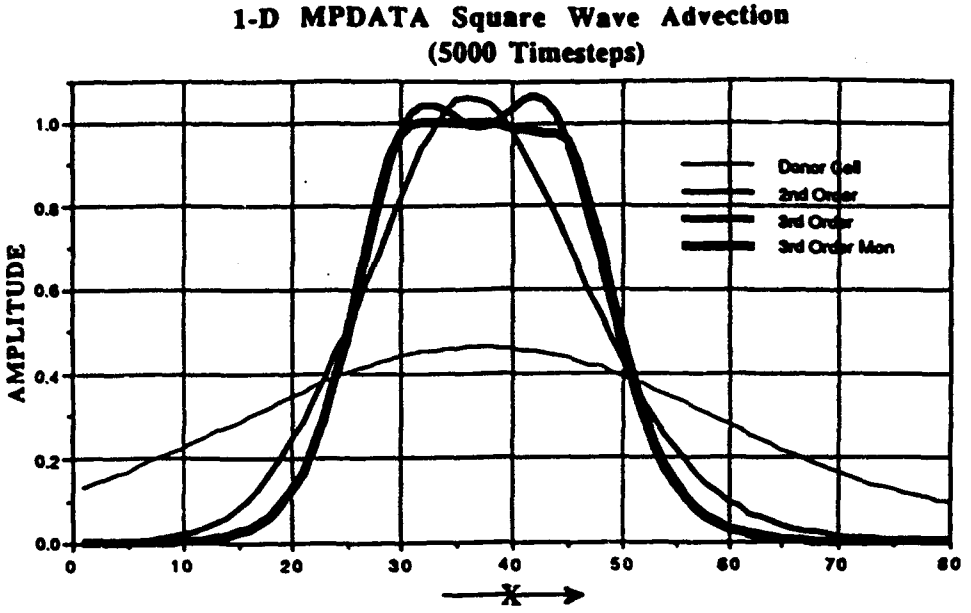

Figure 5-3. Plot of the mass field after 5000 timesteps for the one-dimensional square-wave advection experiments to test the set of configurations available in the Smolarkiewicz MPDATA scheme.

After the one-dimensional advection experiments were completed, the code for the two-dimensional version of the MPDATA scheme was obtained from Dr. Smolarkiewicz at NCAR. This code was inserted into a new test program which was designed to advect a conical-shaped chunk of mass through an "infinite" two-dimensional grid domain. The two-dimensional MPDATA code had the same configuration options as the one-dimensional code.

The initial conditions for the two-dimensional advection experiments consisted of a cone of mass with a height of 1 unit and a base radius of 5 grid units located near the left boundary of a 30 x 30 cartesian grid domain (Figure 5-4). The time integrations were carried out to 500 timesteps on an Apple Macintosh IIcx microcomputer running at a clock speed of 25 MHz. A depiction of the mass field at the end of each experiment is presented in Figure 5-5 and the maximum amplitude and relative computational efficiency of each scheme is listed in Table 5-1. Figure 5-5a illustrates the severe degradation of the shape of the mass perturbation by the upstream (donor cell) scheme. In this experiment the maximum value of the cone-shaped perturbation was reduced to 37% of its original value. The shape of the cone collapsed as strong numerical diffusion smeared the solution in the direction of the flow. The 2nd-order MPDATA algorithm retained 71% of the original peak but it was still somewhat diffusive in the alongstream direction (Figure 5-5b). The best results were obtained with the 3rd-order MPDATA scheme. Almost 94% of the original height remained at the end of the integration. (Figure 5-5c). With this version of the scheme the gradient in the mass field was quite sharp and only a small portion of the mass field was diffused near the base of the cone. The enforcement of the monotonicity constraint on the 3rd-order solution did not improve the results. In fact, the antidiffusive flux-limiting process "clipped" the peak of the cone (Figure 5-5d). This was not totally unexpected since Smolarkiewicz (1983a) had noted that the incorporation of a flux-limiter is extremely effective in preventing overshooting when advecting shocks or contact discontinuities as in the case of the square-wave used in the one-dimensional advection experiments, but it can diminish real peaks and valleys in smoothly varying distributions.

The "runtime" ratio presented in Table 5-1 is a measure of the amount of CPU time required for the computations of one of the higher order versions of MPDATA relative to the fast but highly diffusive donor cell scheme. The computational cost was increased by a factor of 4 and 14 when the accuracy of the numerical scheme was increased to 2nd-order and 3rd-order respectively. The execution was 63% slower when the monotonicity constraint was enforced. However, these comparisons are valid for scalar computations only. The results were expected to be significantly different for computers which have the capability to vectorize the computations.

Table 5-1. *Maximum amplitude of the mass field at the end of the two-dimensional advection experiments and the relative computational cost for each configuration of the MPDATA scheme that was tested.*

SCHEME	MAX AMPLITUDE	RUNTIME RATIO
Donor Cell	.372	1.00
2nd-order MPDATA	.712	4.43
3rd-order MPDATA	.939	14.25
3rd-order monotonic MPDATA	.864	23.23

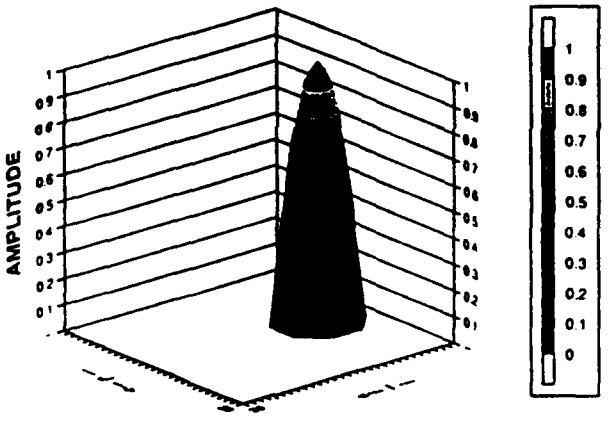

Figure 5-4. *Depiction of the initial conditions used in the two-dimensional advection experiments with the MPDATA scheme. A conical-shaped piece of mass is inserted near the upstream boundary of the grid domain. Cyclic lateral boundary conditions are employed in the time integrations.*

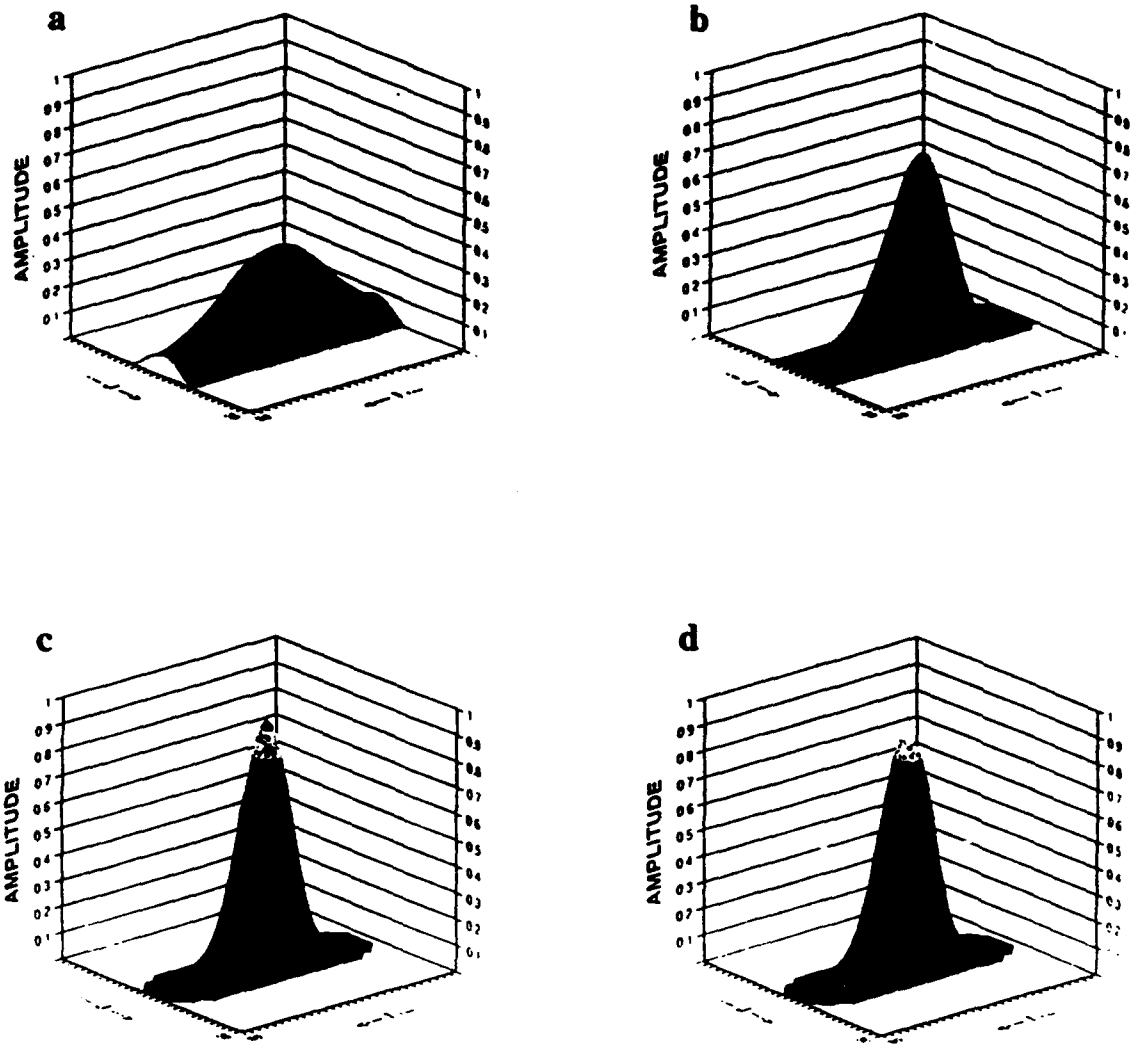

Figure 5-5. Depiction of the mass field after 500 timesteps with: (a) the upstream "donor cell" advection scheme; (b) 2nd-order MPDATA scheme; (c) 3rd-order MPDATA scheme; and (d) 3rd-order MPDATA scheme with monotonicity constraint.

Before the two-dimensional version of the MPDATA code was installed in the MASS model, two modifications were made to the original software. First, a new hybrid type of boundary condition was implemented. It consisted of the application of a constant time-tendency for the evolution of the mass field at the inflow boundary points and an upstream or donor cell advection scheme at outflow boundary points. The second modification was the incorporation of a curvilinear coordinate transformation "metric" term, "m", into the transport equation:

$$\frac{\partial \psi}{\partial t} + m^2 \left[\frac{\partial \left(\frac{u\psi}{m} \right)}{\partial x} + \frac{\partial \left(\frac{v\psi}{m} \right)}{\partial y} \right] = 0 \qquad (5\text{-}10)$$

to account for the distortions due to the map projection scale factor when the calculations are done on a map image plane.

A series of advection experiments to test the new boundary condition formulation was executed. The initial conditions consisted of a square block of mass with a height of 1 and a length/width of 5 grid units, located in the center of a 30 x 30 grid domain (Figure 5-6). The 3rd-order, monotonic version of MPDATA was selected as the transport algorithm. Time integrations were carried out to 300 timesteps on an Apple Macintosh IIcx microcomputer. The results are presented in Figure 5-7. The upstream-differencing advection scheme smoothly transported the mass through the outflow boundary. Because this upstream scheme is much more numerically diffusive than the antidiffusive flux-corrected MPDATA scheme, the leading gradient of the mass field became somewhat degraded. In particular, there is a slight artificial "ramping" in the solution after 80 timesteps, when the steepest slope approaches the boundary (Figure 5-7a). Also, the leading edge of the "flat top" of the block of mass is prematurely eroded at the outflow boundary gridpoints (Figures 5-7b and 5-7c). Nevertheless, the performance of this scheme was deemed to be satisfactory.

Before it was inserted into the three-dimensional MASS code, the two-dimensional MPDATA test program was ported to the Stardent 750 workstation and its computational efficiency was compared with the performance on the Apple Macintosh IIcx microcomputer. The 30 x 30 gridpoint run which required over 5 minutes to execute on the "Mac" required only 12 seconds on the Stardent 750 system when the vectorization option was turned on.

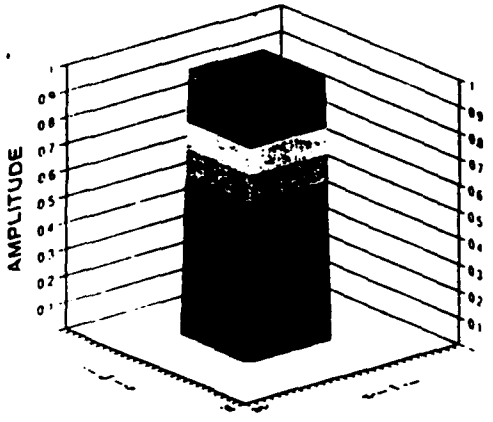

Figure 5-6. Depiction of the initial conditions used in the two-dimensional advection experiments to test the modified lateral boundary condition and the incorporation of the curvilinear metric term into the transport equation.

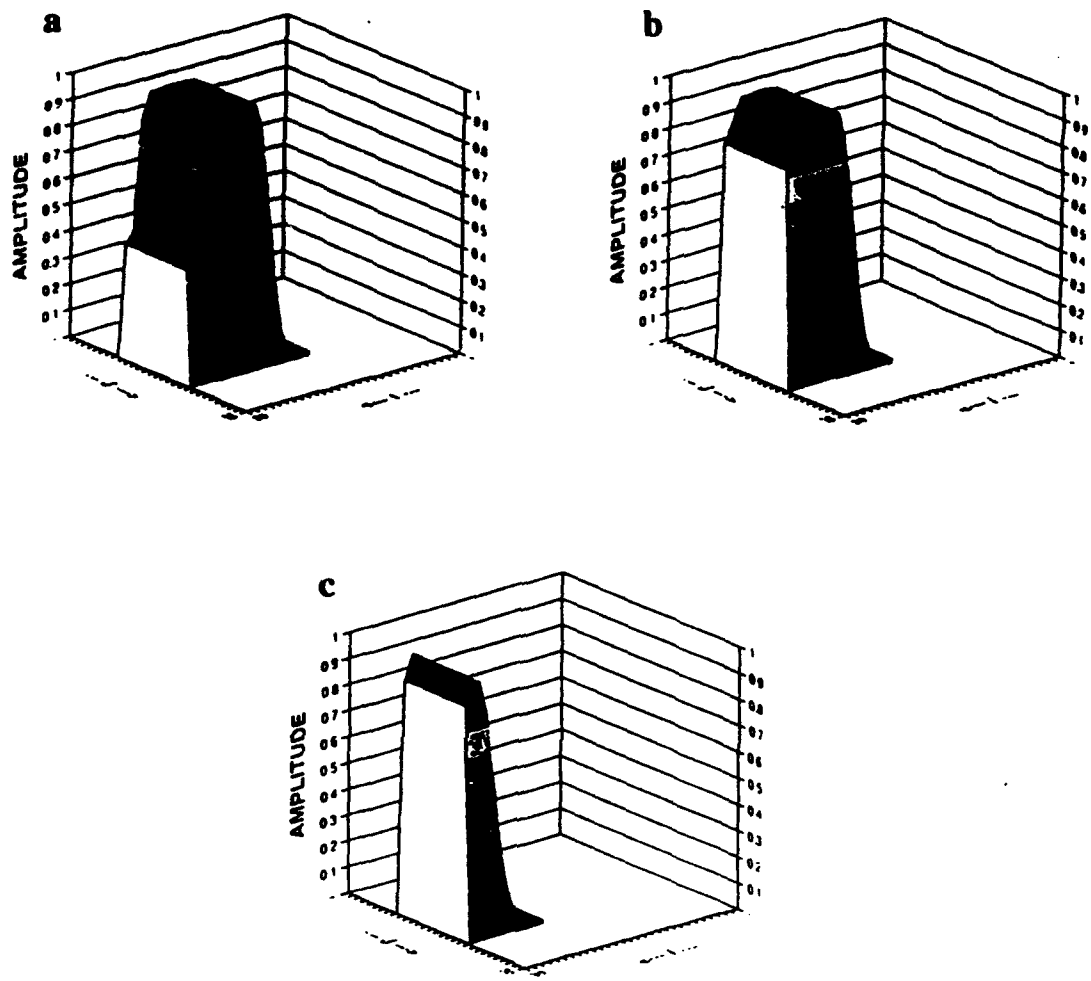

Figure 5-7. *Depiction of the mass field after: (a) 80 timesteps; (b) 100 timesteps; and (c) 150 timesteps in the simulation experiment used to test the hybrid inflow-outflow boundary conditions.*

5.3 *Implementation of MPDATA in the MASS model*

The original MPDATA code is based upon the upstream advection scheme on a grid in which the advecting velocities are placed at points which are located halfway between the points at which the quantity to be advected (ψ) is defined. A example of such a grid is shown in Figure 5-8. The arrangement of variables shown in Figure 5-8 is commonly referred to as the Arakawa "C" grid. However, the MASS model utilizes an unstaggered (Arakawa type "A") grid in which all of the prognostic variables are calculated at the same grid point. Thus, the wind components must be interpolated from their unstaggered positions to the locations depicted in Figure 5-8 before the MPDATA calculations can be performed. Once, the interpolation has been completed the remainder of the MPDATA calculations can be performed in the "C" grid environment.

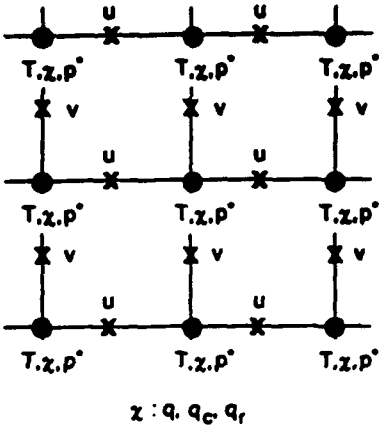

Figure 5-8. *A schematic depiction of the placement of variables on the Arakawa "C" grid utilized in the MPDATA scheme.*

The first step in the MPDATA calculations is to obtain an estimate of the advected variable at the next time step from an upstream calculation. In the x-coordinate direction the calculation can be written as,

$$\psi_i^* = \psi_i^n - \left\{ F\left(\psi_i^n, \psi_{i+1}^n, u_{i+1/2}^n\right) - F\left(\psi_{i-1}^n, \psi_i^n, u_{i-1/2}^n\right) \right\} , \qquad (5\text{-}11)$$

where the F's are the fluxes of the advected quantity at a location one half grid increment to the left and right of the point at which the advection calculation is being performed. The flux at these points is defined as

$$F(\psi_i, \psi_{i+1}, u) = \left[(u + |u|)\psi_i + (u - |u|)\psi_{i+1} \right] \frac{\Delta t}{2\Delta x} , \qquad (5\text{-}12)$$

where Δt is the time step and Δx is the grid spacing. If ψ^* were to be used as the updated quantity, the scheme would be a pure upstream advection scheme. Unfortunately, this scheme is a first-order accurate scheme in both time and space, and has strong implicit diffusion as shown by Smolarkiewicz (1983a). In order to remove the implicit diffusion in this scheme, MPDATA performs a second upstream advection step using an artificial "antidiffusion velocity" to advect the field in place of the actual velocity. The "antidiffusion velocity" is defined as

$$\tilde{u}_{i+1/2} = \frac{\left(|u_{i+1/2}|\,\Delta x - \Delta t\, u_{i+1/2}^2\right)\left(\psi_{i+1}^* - \psi_i^*\right)}{\left(\psi_i^* + \psi_{i+1}^* + \varepsilon\right)\Delta x}, \qquad (5\text{-}13)$$

where ε is a small value (e.g. 10^{-15}) which forces the antidiffusion velocity to be zero when the scalar quantity is zero at both the i and i+1 points. The antidiffusion velocity is then used to advect the scalar field in the second step of the scheme,

$$\psi_i^{**} = \psi_i^* - \left(F\left(\psi_i^*, \psi_{i+1}^*, \tilde{u}_{i+1/2}\right) - F\left(\psi_{i-1}^*, \psi_i^*, \tilde{u}_{i-1/2}\right)\right), \qquad (5\text{-}14)$$

and produce a revised estimate (ψ^{**}) of the advected quantity at grid point i. This value can be used as the final result of the advection process for grid point i. If this is the case then this would be the 2nd-order version of the MPDATA scheme. However, the process can be repeated again by using equation 5-13 to calculate a new antidiffusive velocity with the ψ^{**} values. This procedure yields a higher order version of MPDATA.

A limited implementation of the MPDATA scheme was made in the MASS model. In this implementation, MPDATA can be utilized only for the advection of cloud water (ice), rain water (snow) or tracer material. In principle, the scheme could be used for the advection of any of the prognostic variables. However, in order to assure dynamical consistency among the variables that are strongly coupled, the scheme must be used with all of these variables simultaneously. If it is implemented with only one variable (for example, the water vapor mixing ratio) the slight differences in phase speed between the MPDATA scheme and other schemes such as Adams-Bashforth can result in the generation of dynamically inconsistent fields and the generation of spurious features.

Once the installation of the MPDATA subroutine into the MASS model was completed, a series of simple simulations were executed to verify that the code was correctly installed and to test the performance of the scheme. The first experiment was the advection of a massless tracer with an idealized wind distribution on a 50 km grid. In this test, the wind was constrained to be 25 m s^{-1} from the west at all model grid points throughout the simulation. That is, the wind was spatially uniform and time invariant. The left column illustrates the total mass in kg m^{-2} that was instantaneously injected into the model atmosphere at the initial time (1200 UTC). This value was the result of instantaneously injecting 1.0×10^{10} kg of tracer mass per model grid cell per 500 meter vertical layer. As the illustrations in the left column of Figure 5-9 suggest, the tracer substance was injected into only 4 MASS model columns over southern California. The underlying geography in this depiction is used for reference purposes only. There was no terrain or other geography-related effects incorporated into the simulation. The use of only 4 horizontal points poses a severe test for an advection scheme since the lateral scale of the tracer pool is at the lower limit of what is resolvable on the grid system. The top row of Figure 5-9 (a-c) illustrates results from the 2nd-order version of MPDATA, the middle row (d-f) depicts the performance of the 3rd-order version of MPDATA while the bottom row (g–i) shows the performance of the 4th-order accurate space difference/Adams-Bashforth time integration advection scheme (the original MASS advection scheme). In this case, a good performance by an advection scheme would result in the translation of the injected mass downwind while preserving its shape and maximum concentration value. Figure 5-9 illustrates that all three of the schemes reduce the peak value significantly during the 6 hour simulation period. Surprisingly, the original MASS scheme produces a concentration value that is closest to the value at the time of the initial injection. The MPDATA scheme had been expected to preserve the shape and maximum value of the mass pool better than the original MASS scheme. These surprising results are most likely dependent on the scale of the tracer pool. Apart from this somewhat surprising outcome, the

results from these test simulations confirmed the expectations that: (1) the 3rd-order MPDATA is better at preserving the maximum value of the tracer pool than the 2nd-order scheme, (2) the original MASS scheme is much noisier than the MPDATA scheme; and (3) as advertised, the positive-definite MPDATA scheme produced no negative values of tracer mixing ration while the original MASS scheme produced some negative values in the vicinity of large tracer mixing ratio gradients.

The damping of the tracer pool in these initial experiments was examined more closely. It was determined that the scheme worked well when running advection experiments with an initial tracer field consisting of a square/sine wave resolved by 4 or more gridpoints in the direction of the flow. However, the initial distribution of tracer used in the initial experiments conducted with the MASS model was only 1 to 2 gridpoints wide in the direction of the flow.

This behavior was traced to the fact that numerical finite differencing schemes which use flux correction techniques (MPDATA and FCT, for example) calculate their flux limiters based on the minimum and maximum values at neighboring gridpoints. That is, they decide how much additional mass should be added to the diffused solution at a gridpoint in order to restore the mass field to its pre-diffused form by looking at peaks and valleys at surrounding gridpoints. If a "spike" of tracer is not adequately resolved, then the extrema can "fall through the grid mesh" during the advection process, never to be recovered by the flux limiters again. This numerical "clipping" process can often be remedied by using a "smarter" flux-limiting algorithm, one which "remembers" the values of the extrema for the previous timestep or one which calculates the minimum and maximum values at higher than grid mesh resolution. This type of approach was investigated by coding a version of Zalesak's (1979) flux limiter, which calculates the maxima and minima between grid points. by finding the intersection of two lines which approximate the shape of the mass field at half-gridpoints. A series of one-dimensional advection experiments was then made to assess the performance of the new flux limiter. The results of these experiments are shown in Figure 5-10. A one gridpoint wide disturbance of amplitude 1.0 was inserted into the initial mass field and transported with a constant, uniform velocity. The differences are quite apparent even after only 25 timesteps. The new Zalesak flux limiter, implemented in the flux-corrected transport (FCT) algorithm, recovered about 37% of the original amplitude, while the old limiter only retained 31%. The width of the mass field is also narrowed, which results in a more realistic, "spike-like" representation. The amplitude still falls short of the Adams-Bashforth scheme, which holds onto 59% of the original peak value. However, it should be noted that the two FCT solutions are much less noisy in the originally unperturbed regions than the Adams-Bashforth solution. The latter advection algorithm leaves a long wake of trailing ripples (numerical noise or Gibbs oscillations) due to numerical wave dispersion, with amplitudes as high as 37% of the original height.

Dr. Piotr Smolarkiewicz was consulted to see if he had developed a better algorithm for transporting such "spike-like" distributions of tracer. He indicated that he had tried customized flux limiters in the past, but had concluded that once there is a very narrow spike in a field, finite difference methods are simply inadequate. He indicated that the reason for this can be understood by expanding the finite difference form of the governing advection equation in the form of a Taylor series. He indicated that the result be that the expansion will approximate the original analytical equation plus some extra terms (i.e. error terms). The error terms scale as NP, where N is the number of grid points per scale of interest and P is the order of the term. Therefore, no matter how accurate the scheme is, if the number of grid points per scale of interest is 1, the Reynolds-like number will be 1 too. In other words, if a one-gridpoint perturbation is to be simulated, even a super accurate, say, 100th-order scheme will suffer from errors comparable to the analytic terms. Thus, finite-difference techniques are not appropriate for under-resolved features. There are techniques which claim the ability to treat under-resolved features, for example moments methods. But all they do is store more variables (values per gridpoint) which is, in essence, an increase in the resolution of the grid.

Furthermore, the Zalesak flux limiter is customized to handle isolated extrema. It creates artificial overshooting when the initial tracer is more uniform in shape, as shown in Figure 5-11. In general, specialized flux limiters should not be implemented unless the shape of the initial tracer field is known beforehand. This is clearly not the case in the general application of a three-dimensional mesoscale model.

Advection experiments were conducted with more realistically shaped tracer distributions in order to evaluate the relative accuracy of the FCT and MPDATA schemes. Transport simulations using initial square wave and sine wave distributions all produced similar results with the MPDATA scheme retaining more of the initial disturbance amplitude and preserving steep gradients better than flux-corrected transport (Figure 5-12). The higher numerical diffusion in the FCT algorithm became especially apparent in runs which extended beyond 1000 timesteps.

These results suggested that the MPDATA scheme without the Zalesak flux limiter was the best choice for use in the MASS model. The scheme was then configured to advect the water vapor mixing ratio in the three-dimensional version of the MASS model. In order to test the scheme in a complex wind pattern the model was initialized with a data matrix of $85 \times 55 \times 15$ points from 1200 UTC April 10, 1979 (the day of the infamous Wichita Falls tornado). Three 6-hr simulations were executed from this initial dataset. In order to have a pure comparison of the performance of each of the horizontal advection schemes, all other processes (e.g. vertical advection of vapor, condensation, etc.) which act on the water vapor field were omitted from the simulation. The first simulation employed the 4th-order accurate centered space difference and the Adams-Bashforth time integration scheme (i.e. the original MASS advection scheme) to horizontally advect water vapor. The second simulation was identical to the first except that the donor cell version of MPDATA was used for the horizontal moisture advection. The third simulation used the 3rd-order version of MPDATA with the monotonicity constraint and a correction for divergent flow. The dew point for the lowest model layer (approximately 30 mb above the surface) for each of the simulations is shown in Figure 5-12. A comparison of the field produced by the either of the MPDATA schemes (Figures 5-12b and 5-12c) with that produced by the Adams-Bashforth scheme (Figure 5-12a) immediately reveals that MPDATA produces much sharper gradients and maxima and minima that are more extreme. In fact, in certain areas the extreme values appear to be slightly excessive. This is probably due to the absence of other processes which offset the advection effects in a full physics simulation. Another difference between the simulations can be seen by examining the dew point pattern over southwestern Texas and adjacent Mexico. In this area, the Adams-Bashforth simulation (Figure 5-12a) produces noticeable high-frequency oscillations in proximity to the large moisture gradient over Texas while no trace of oscillations can be found in either of the MPDATA simulations. A second simulation which utilized the complete moisture physics was also executed. In this simulation the temperature was advected with the Adams-Bashforth scheme and the water vapor was advected with the 3rd order MPDATA scheme. This simulation generated spurious areas of saturation, latent heating and precipitation due to the differences in numerical dispersion and phase speeds between the two advection schemes. This experiment supported the notion that it is not wise to utilize different advection schemes for prognostic variables that are strongly coupled.

In order to test the ability of the MPDATA scheme to advect a mass of particles injected into the atmosphere in a real-world situation, a three-dimensional simulation of the ash cloud generated by the eruption of Mt. St. Helens on May 18, 1980 was executed. A version of MASS which used a $90 \times 60 \times 17$ matrix and a 15 km grid increment was used for this experiment. The vertical profile and rate of injection of ash was estimated from data published by Sarna-Wojcicki et al. (1982) and Carey and Sigurdsson (1982). A 3rd-order version of MPDATA without any lateral numerical diffusion was used for this simulation experiment. A depiction of the time evolution of the vertically integrated (surface to the top of the model domain) airborne ash for the 8 hr period after the initial eruption is shown in Figure 5-13. The bold dashed lines in this figure indicate the outline of the satellite-observed ash cloud at each time as diagnosed by Sarna-

Wojicki et al. (1982). The transport simulated by the MASS model with the MPDATA advection scheme seems quite reasonable. The small discrepancies between the simulated ash distribution and the satellite-observed ash cloud pattern are probably attributable to: (1) errors in the model wind forecast because of: (a) the customary limitations in the amount and distribution of initialization data, and (b) limitations in model resolution and the physics; (2) imprecise specification of the vertical profile and rate of ash injection into the atmosphere from the eruption; and (3) the unknown value of the vertically integrated ash content that corresponds to the boundary of the ash cloud in the satellite imagery.

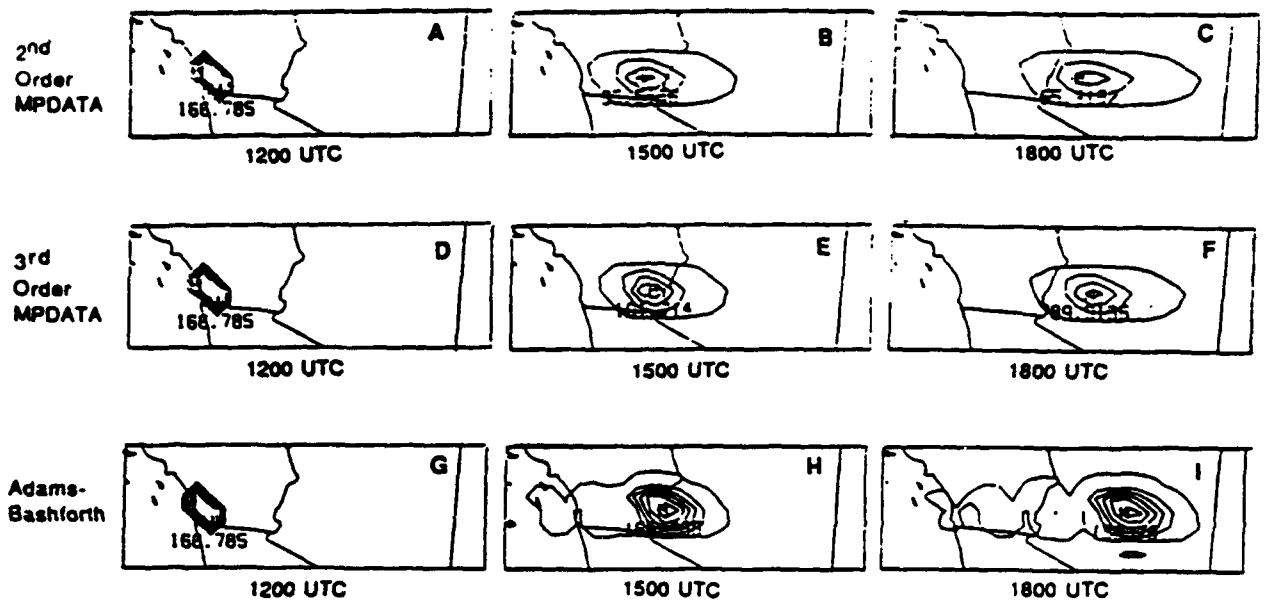

Figure 5-9. The concentration (kg m^{-2}) of a massless tracer integrated from the surface to 609 m (2000 ft) from three advection experiments. The winds are spatially uniform and time invariant at a value of 25 m s^{-1}. Tracer distributions at the initial time (1200 UTC), 3 hours (1500 UTC) and 6 hours (1800 UTC) after initialization are shown for each experiment. (a-c) 2nd-order MPDATA; (d-f) 3rd-order MPDATA; (g-i) Adams-Bashforth with fourth order spatial finite differencing.

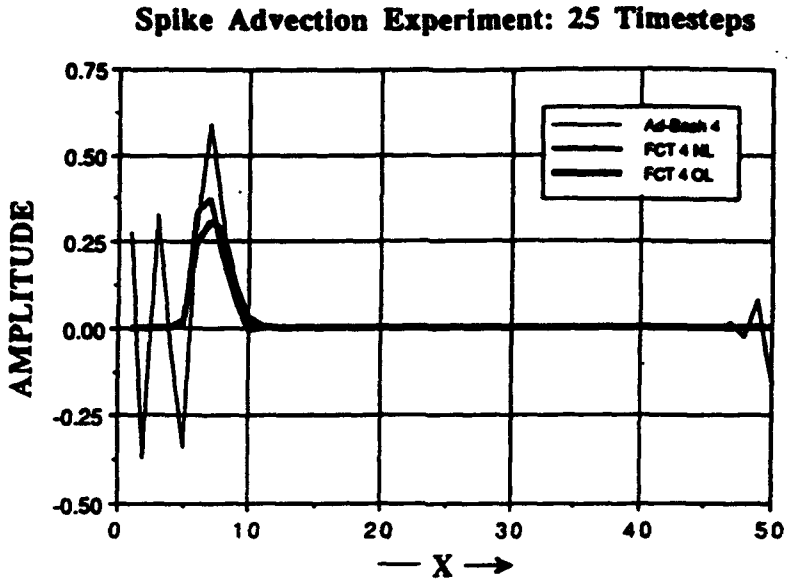

Figure 5-10. The results from a series of one-dimensional advection experiments executed to test the performance of the Zalesak one-point extremum flux limiter. A 4th-order version of the flux-corrected of the flux-corrected transport (FCT) algorithm was used to transport a one-gridpoint "spike" of tracer with an amplitude of 1.0 through a uniform flow field. The simulations show that the Zalesak limiter, denoted by NL for "new limiter", is able to retain more of the initial amplitude of the disturbance and replicate the narrowness of the spike-like representation more faithfully than the old flux limiter (OL). The results of he 4th-order Adams-Bashforth scheme, which is currently used in the MASS model, are also presented. Cyclic boundary conditions were used for all experiments.

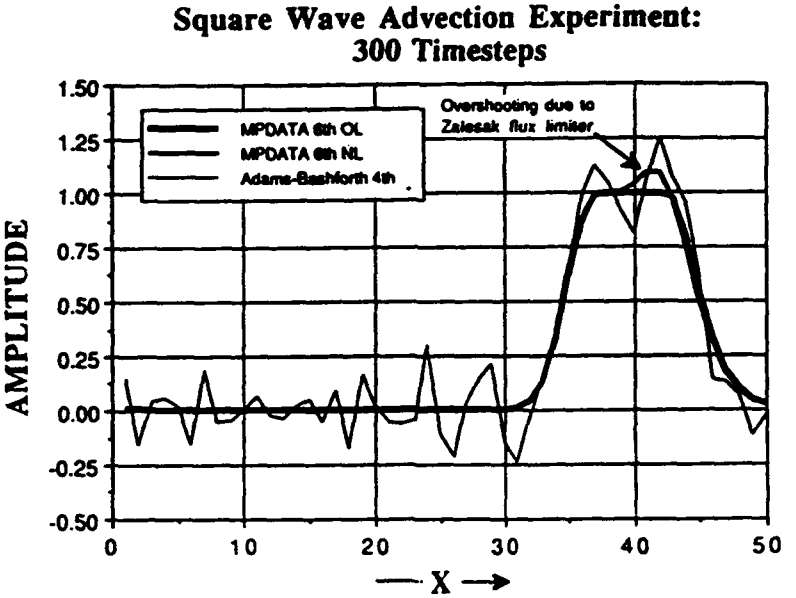

Figure 5-11. The results from of a 1-D square-wave advection experiment which show how the Zalesak one-point extremum flux limiter (NL for "new limiter"), designed to recover unresolved minima/maxima, "overshoots" the amplitude of the initial tracer field when it is uniform in shape. Also notice the long trailing wake of Gibbs oscillations (noise) due to numerical wave dispersion present in the Adams-Bashforth scheme, which is currently used in the MASS model.

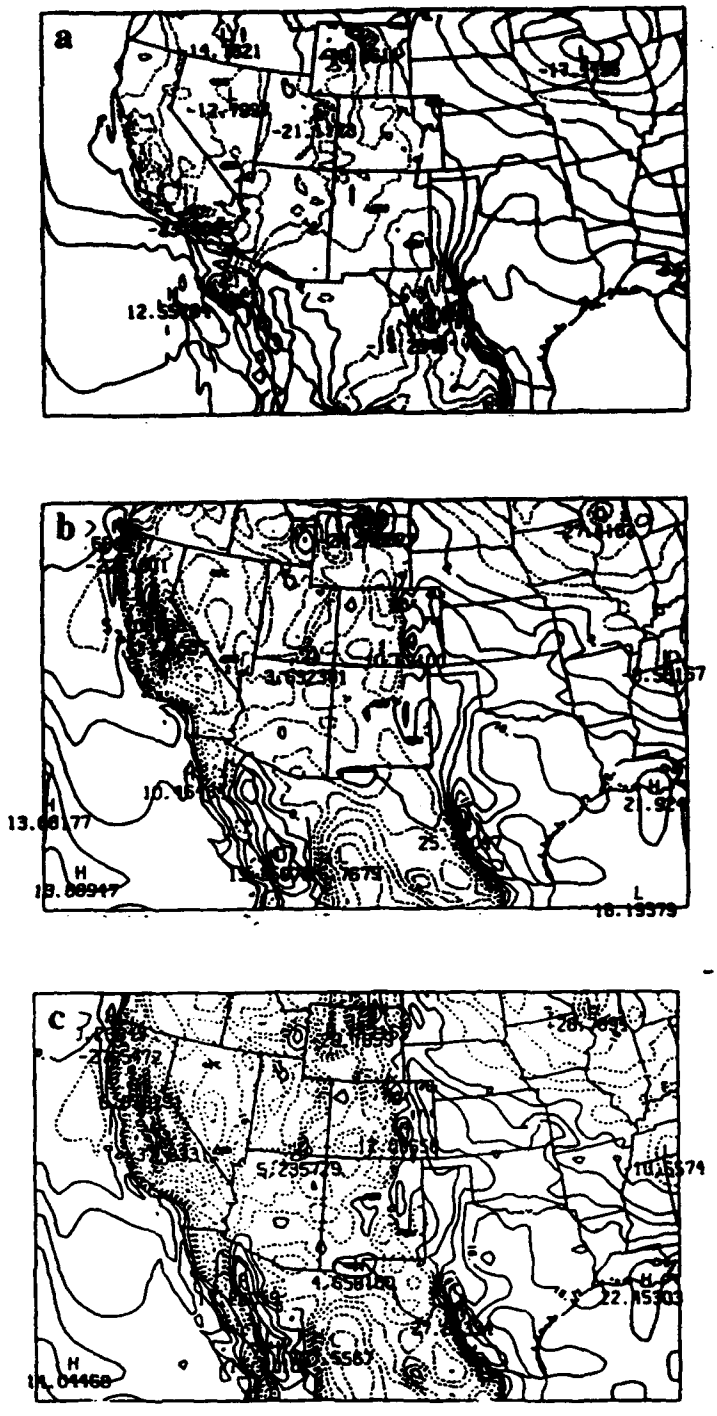

Figure 5-12. Dew point in the lowest model layer from three six-hour MASS simulations initialized at 1200 UTC April 10, 1979. The contour interval is 4 °C. All of the simulations are identical with the exception that the advection of water vapor mixing ratio is computed by: (a) the fourth order space difference / Adams-Bashforth time difference scheme, (b) the donor cell version of MPDATA, and (c) the 3rd-order MPDATA scheme with monotonicity constraint and correction for divergent flow.

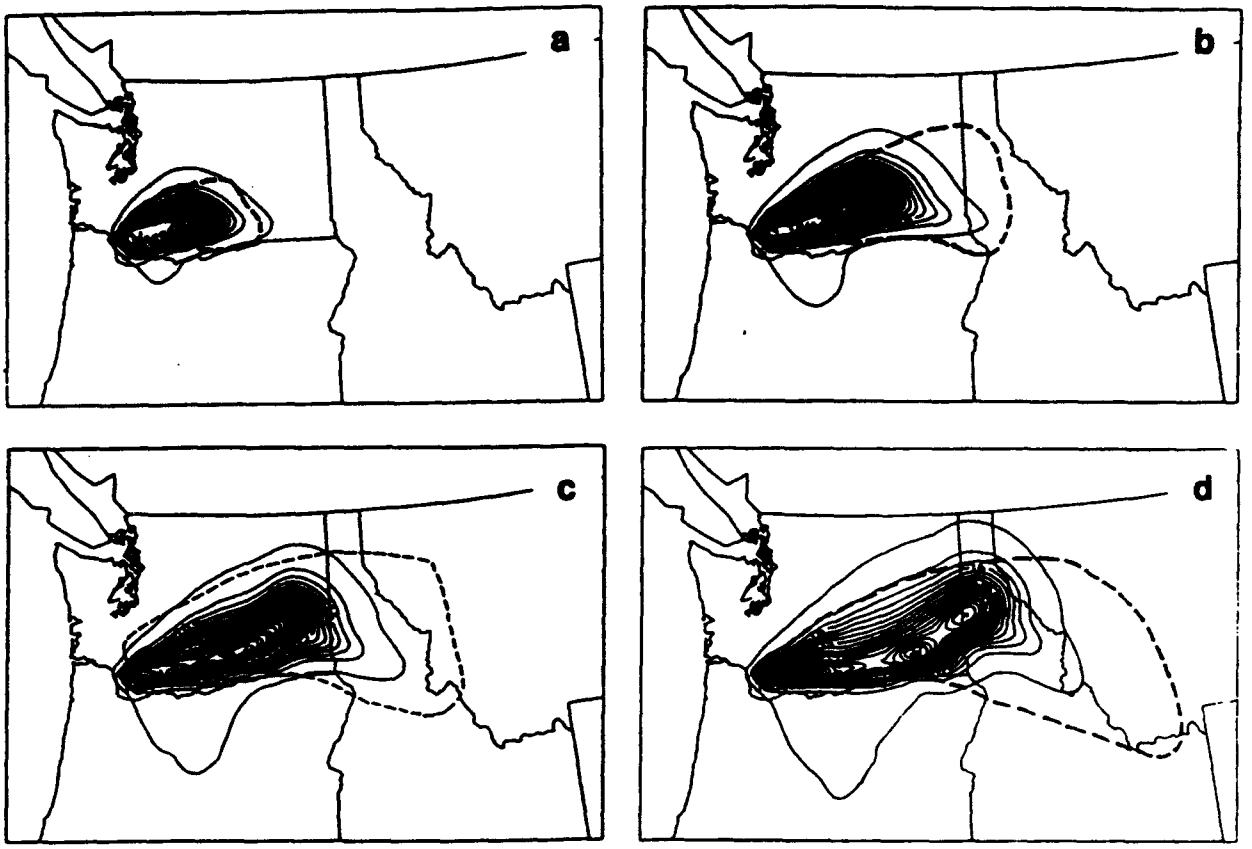

Figure 5-13. *Vertically-integrated airborne ash per unit area (kg m^{-2}) from a 15 km MASS simulation with the 3rd-order MPDATA scheme used for ash transport. The ash depictions are for: (a) 1745 UTC; (b) 1945 UTC; (c) 2145 UTC; and (d) 2345 UTC. The first contour at each time is .05 kg m^{-2} and the contour interval is 0.5 kg m^{-2}. The bold dashed lines indicate the outline of the satellite-observed ash cloud at each time as reported by Sarna-Wojicki et al. (1982).*

6. Data Assimilation System

The initialization of mesoscale numerical models in a battlefield environment is a significant challenge. In such an environment, observational data is typically available from a variety of sources, each with its own strengths and weaknesses. Any single data source may be available in only a portion of the area of interest, may not measure all dependent atmospheric variables or may contain individual observations, each valid at a different time. The challenge is to combine the information available from each data source into a well-balanced model initialization that includes all mesoscale features which are resolvable by the model.

In order to take the best possible advantage of the various types of data, modelers have developed various methods of continuously inserting current and past data into a numerical model during a specified pre-forecast period. This method, now known as four dimensional data assimilation (FDDA), allows the model initialization to take maximum advantage of data sources available at asynoptic times as well as data with high temporal resolution. FDDA was pioneered by Charney et al. (1969) who suggested that the model's prognostic equations would provide time continuity and dynamic coupling between the various fields.

The MASS model uses several types of FDDA and an innovative method of static moisture initialization, in addition to the standard static objective analysis with a first guess. These include: (1) Newtonian relaxation or nudging of gridded rawinsonde, surface or profiler observations (Hoke and Anthes, 1976) in which the model state is relaxed towards an analysis of observations; (2) the use of Manually Digitized Radar (MDR) data to specify moisture convergence (precipitation rates) in areas which are (are not) subject to convection according to the Kuo-MESO cumulus parameterization scheme; and (3) the enhancement of the three dimensional moisture analysis with surface observations of clouds, pilot reports, MDR data and infrared satellite images.

6.1 Surface Data

The assimilation of surface data is based on the techniques of Stauffer et al., (1991). The scheme is described in depth in the MASS Reference Manual (MESO, 1993a). It was initially implemented in a manner identical to that of Stauffer et al., (1991). As the scheme was tested though, several improvements were made. These include:

1) The use of an Ekman wind profile to nudge winds in the planetary boundary layer (PBL) in regions where a profile can be found that achieves a reasonable fit with both the gridded surface wind analysis and the model winds at the top of the PBL. This is superior to assuming a constant wind velocity in the PBL.
2) The adjustment of gridded surface wind analysis to reflect the model-defined surface roughness at each individual grid point. This was done mainly in response to the tendency of surface nudging to spuriously reduce wind speeds over water, since most observations are land-based.
3) The nudging of gridded surface temperature in the PBL. Temperature is nudged most strongly in the lowest model layer. The strength of nudging decreases until it reaches 0 at the top of the PBL. Stauffer et al., (1991) did not nudge surface temperature because of its potentially harmful interaction with the PBL parameterization (i.e., the PBL parameterization will be forced into another regime). Surface temperature nudging in the MASS model, however, has produced mostly positive effects. Perhaps this is due to the fact that errors in the representation of cloudiness along with incomplete knowledge of the

distribution of soil types, soil moisture and vegetation can sometimes lead to significant temperature errors in the model PBL. While nudging temperature will not prevent these limitations from leading to temperature errors after the forecast period has begun, it can minimize the propagation of PBL temperature errors. Another reason for nudging temperature is that in regions with large errors in the simulated temperature field, the model PBL is likely to be in a different regime than the actual atmosphere anyway.

4) Numerous modifications were made to the Barnes objective analysis scheme to improve the analysis in the vicinity of coastlines. Coastlines are frequently collocated with sharp discontinuities in low-level wind, temperature and moisture fields. Most objective analysis schemes do not resolve these discontinuities. This problem is especially compounded by the fact that the vast majority of surface observations are land-based. With a simple objective analysis scheme, the values of surface variables are often heavily influenced by land-based observations at grid points which are located just offshore. The improved Barnes scheme eliminates this problem. See Section 7.1 of the MASS Reference Manual (MESO, 1993a) for details on the modifications made to the Barnes scheme.

5) The method of calculating confidence factors was improved so that the confidence factor would fall sharply to 0 where there were discontinuous changes in data density such as at a coastline. The differentiation between land and water observations also contributes to sharp changes in the confidence factor at coastlines. See Section 7.1 of the MASS Reference Manual (MESO, 1993a) for details.

6.2 *Rawinsonde Data*

The assimilation of rawinsonde data is described in depth in the MASS Reference Manual (MESO, 1993a). As for the surface data, the rawinsonde nudging scheme was initially implemented in a manner identical to that of Stauffer et al., (1991). As the scheme was tested though, several improvements were made. These include:

1) Changes in the method of calculating the confidence factor so that it would fall sharply to 0 on the sparse-data side of discontinuities in data density. The confidence factor is also calculated at each level in the vertical and for each variable. Before these changes were implemented, the nudging of gridded data just on the sparse-data side of a data discontinuity, or in other regions of low data density, often caused large oscillations in the mass field.

2) The nudging of rawinsonde data only within 4 hours of a rawinsonde observation time and nudging with full weight only within 2 hours of an observation time. Rawinsonde data is available only every 12 hours which is too infrequent to resolve the finer scale structure that a mesoscale model can simulate. For this reason, a linear interpolation in time is not sufficient mid-way between observation times.

6.3 *Profiler Data*

The assimilation of profiler data is based on the techniques used by Stauffer et al., (1991) to nudge rawinsonde data. Height-based wind profiler observations are interpolated to pressure

surfaces by using a recent model initialization file to estimate the height field. Temperatures are derived through the inversion of the divergence equation as in Cram et al., (1991). The scheme is described in depth in the MASS Reference Manual (MESO, 1993a).

Wind profiler data provides accurate and frequent 3-dimensional data that seems to be ideal for assimilation into a mesoscale model. However, there are several drawbacks including a lack of direct information on the mass field, a lack of any data within about 1 km of the earth's surface, and poor spatial resolution relative to the temporal resolution. The development of the profiler nudging scheme focused on efforts to overcome these drawbacks.

The first challenge was to interpolate the wind information to pressure coordinates so that it could be analyzed. This was done by assuming that a MASS output file at or near the profiler observation time would provide a reasonably accurate height-pressure relationship. Once this was accomplished, the next step was to derive some sort of mass field information from the wind field, since accurate mesoscale forecasts typically require an accurate representation of both the mass and the wind field. Cram, et al., (1991) inverted the divergence equation to derive the 3-dimensional temperature field when only the wind field was known. This technique was adapted to the MASS model, but a few changes needed to be made to the nudging scheme. First, MASS output was used to provide a first guess for the profiler wind analysis. This produced a reasonable wind field throughout the model domain and prevented the divergence technique from producing ridiculous temperatures in and near data sparse regions. The MASS output was also used to provide the height field at the domain boundaries, which the technique requires. Second, the time derivative term was ignored (term H in Cram et al.'s equation (1)). This term had little effect on the temperature derivation, and ignoring it simplified the process by eliminating the need for a second profiler wind analysis. Finally, the temperature confidence factor was set to 0 within 1750 m of the earth's surface. This was done because it was discovered that frictional effects which are not included in the divergence equation, but are present in the PBL, contaminate the temperature analysis at lower levels.

6.4 Manually Digitized Radar (MDR) Data

MDR data and reports of areal coverage of radar echoes are used to estimate the precipitation rate at each model grid point. This data is then inserted into the model by specifying a parabolic latent heating profile at grid points which are ineligible for convection, according to the Kuo-MESO cumulus parameterization scheme or by specifying the moisture supply parameter at points which are eligible for convection. The scheme is described in depth in the MASS Reference Manual (MESO, 1993a). The implementation of the MDR data assimilation scheme is described below.

The development of the MDR assimilation scheme went through several phases. First, VIP levels and reports of areal coverage were used to estimate cloud top levels and mean relative humidities. The RH information was then nudged into the model simulation. This scheme performed reasonably well in regions where stable grid scale precipitation was falling, but not so well where convection was occurring. The next phase was to derive precipitation rate estimates from the MDR and areal coverage data. Estimates were fine tuned through trial and error. Then, rather than nudging RH in convective regions, the precipitation rate estimate was used to specify the moisture convergence field in the Kuo-MESO convective parameterization scheme. This produced a significant improvement in the representation of convection during the data assimilation period. The final phase was in response to the fact that nudging RH in regions of precipitation was ineffective in regions where the model incorrectly forecasted downward vertical motions. This often occurred where mesoscale precipitation regions were not resolved by the observing network. To help improve the simulation in such regions, the precipitation rate and cloud top height estimates were used to specify a parabolic latent heating profile in regions of grid scale precipitation. This was done in place of nudging RH. Below an assumed cloud base of

about 1000 m above the ground, RH was nudged as it had been. This final change resulted in a substantial improvement in the representation of grid scale precipitation areas that were not well resolved by the observing network.

Experience has shown that the assimilation of MDR data helps to accurately define both the grid scale and subgrid scale precipitation field at the time of model initialization. The benefits of MDR assimilation typically last for about 6 to 9 hours. They are most dramatic during the initial three hours due to the elimination of the precipitation spin-up problem that is common to all numerical models.

6.5 Synthetic Relative Humidity

The synthetic RH retrieval scheme uses visual observations of clouds, infrared (IR) satellite data and MDR data to enhance the rawinsonde moisture analysis. The scheme is described in depth in the MASS Reference Manual (MESO, 1993a). The implementation of the synthetic RH analysis scheme is described below.

The main challenge in the implementation of the synthetic RH scheme was to determine just what information about the RH field could be gleaned from the various data sources and how the different data sources could be combined to provide the best estimate of RH.

The derivation of vertical RH profiles from visual observations of clouds underwent several changes during development. First, the mean RH at each level above the ground was simply averaged from all of the soundings associated with each observation in a given cloud weather category. Next, statistical correlations were determined based on the height and extent of coverage of each cloud layer. Finally, statistical correlations were stratified into layers so that a different set of regression equations existed for levels that were below the lowest cloud layer, between the lowest and the next highest cloud layer, between the middle and the highest layer, and above the highest cloud layer. Each of these improvements helped to reduce the root mean square errors of the RH estimates. This resulted in more statistical soundings with a small enough error to be included in the RH analysis. Whenever relative humidity fields derived from visual cloud observations are available, they are blended with the model RH analysis through an objective analysis before any other adjustments are made. MDR and satellite data are then used to provide the finer structure of the RH field.

Several data sources were combined to determine the best possible distribution of cloud coverage, base and height. IR satellite data is ideal for determining cloud top height and areal coverage of clouds. Cloud base information can be determined by visual observations. The presence of MDR echoes or the detection of a convective tower by Adler and Negri's (1988) IR satellite technique indicates that a moist layer likely extends from cloud top to the ground. When satellite data is missing, MDR data can also be used to estimate cloud top height and areal coverage, as is done in the MDR data assimilation scheme (see Section 14.5 in the MASS Reference Manual, MESO, 1993a). Since IR satellite data has higher resolution and provides a more reliable estimate of cloud coverage, it overrides MDR data in the determination of cloud top height and coverage. When an MDR echo is not present, it is impossible to determine whether or not a cloud layer is continuous between the satellite determined cloud top and the visually determined cloud base. Experimentation shows that when both the satellite and the visual observation indicate extensive cloud coverage, it is wise to err on the side of over-moistening the atmosphere and assume the cloud is continuous in the vertical. When either a cloud base or cloud top height, but not both can be determined, the cloud is assumed to be thin. After extensive trial and error, the synthetic RH scheme evolved into the quite complicated, but effective algorithm that is described in Chapter 5 of the MASS Reference Manual (MESO, 1993a).

The synthetic RH scheme is most valuable when simulating cases with weak or nonexistent synoptic forcing and strong boundary layer forcing. In these situations, convection is

often triggered by differential heating due to meso-β scale variations in cloud cover. The synthetic RH scheme is the component of the model data assimilation system which is most effective at adding such fine scale variations in cloudiness.

7. The Observing System Simulation Experiment (OSSE)

The data assimilation process raises many issues which must be understood in order to optimize the performance of the model. The final design, tuning and intelligent use of the assimilation-forecast system requires knowledge of:

1) the relative merits of different assimilation strategies.
2) the cost/benefit ratio of an extensive data assimilation cycle versus a "cold-start" initialization.
3) a method to estimate the optimal value for each of the nudging coefficients.
4) the error growth in MASS simulations during the forecast period.
5) the relative impact of each data type on the MASS mesoscale forecasts.

An observing system simulation experiment (OSSE) is an excellent tool for addressing these issues. An OSSE makes use of a high resolution numerical model simulation to provide a dynamically consistent "surrogate atmosphere simulation" (SAS). Simulated observational data is then extracted from the SAS and objectively analyzed to create a model initialization dataset and/or gridded data to be assimilated through nudging. Experimental simulations are then run on a coarser grid which is entirely contained within the SAS grid. The main advantage of OSSEs over conventional experimental simulations is that the state of the "surrogate atmosphere" is known exactly while the state of the real atmosphere is not. Therefore, OSSE simulations can be rigorously compared to the "true" state of the atmosphere. This allows for the careful evaluation of the performance of various data assimilation schemes. Unfortunately, there are also several disadvantages to OSSEs. For example, many errors which find their way into actual observations cannot be included in OSSEs. These include errors introduced through the aliasing of small scale features that are not resolved on the OSSE grid, occasional large errors related to equipment malfunction, and systematic errors at one or more observing locations. In addition, the nature of data extraction in an OSSE makes it very difficult to produce certain types of simulated data, such as satellite and radar data and visual cloud observations. Finally, the "surrogate atmosphere" only resembles the real atmosphere to the extent that the numerical model effectively simulates all atmospheric processes. The net result is that OSSE experimental simulations are expected to parallel the SAS more closely than conventional simulations parallel the real atmosphere. Still, the possibility of detailed comparisons between the experimental simulations and a well known "verification" make an OSSE a worthwhile endeavor.

Stauffer et al., (1991) point out that precipitation is the best variable for verifying the effects of nudging because it is not assimilated into the model itself and it is sensitive to many dynamic and thermodynamic processes on all scales of motion. Therefore, precipitation will be the primary verification variable. However, since the simulations presented in Stauffer et al., (1991) consist of only a pre-forecast period, they have no reason to use any variable which is directly assimilated for verification. Since the simulations presented here include a short pre-forecast period followed by a forecast, other variables including winds, temperature and sea level pressure will prove useful for verification during the forecast period.

7.1 Experimental Design

The case of the Midwestern squall line of 5-6 September 1992 was selected for the OSSE. A brief review of the case is presented in Section 7.2. The period of interest is the 12 hour period

beginning at 0000 UTC 6 September. The grid selected for the "surrogate atmosphere" simulation (SAS) measures 77 x 70 with 28.65 km resolution and is shown in Figure 7-1a. The simulation was initialized at 0000 UTC 5 September and integrated for 36 hours.

The experimental simulations were initialized from the SAS at 0000 UTC 6 September or at 1200 UTC 5 September (see Table 7-1 and Figure 7-2). All experimental simulations were integrated until 1200 UTC 6 September on a 41 x 38 grid with 40 km resolution. The grid is entirely contained within the SAS grid and is shown in Figure 7-1b.

Simulated data was extracted from the SAS at standard observing station locations and times. Locations of the simulated surface, rawinsonde and profiler observations are shown in Figure 7-3a, b and c, respectively. Surface and profiler stations are assumed to report on an hourly basis and rawinsonde stations at 0000 and 1200 UTC. It is assumed that any given observing station has a 2.5% chance of not reporting at a given time. In order to more accurately simulate real observing systems, a random, normally distributed error with a standard deviation similar to that of the actual observing system was added to each observation. The standard deviation for each variable and observing system are shown in Table 7-2.

Table 7-1. Experimental Simulations performed in the OSSE.

Simulation	Init.	G (s^{-1})	Data Assimilated
C1	00/6	------	Static initialization
C2	00/6	------	Same as C1, but constant boundary conditions
C3	12/5	------	Same as C1, but 24 hour simulation
S1	00/6	.0003	Surface u, v, T, q 0000 - 0200 UTC
S2	12/5	.0003	Surface u, v, T, q 1900 - 0200 UTC
U1	12/5	.0003	Rawinsonde u, v, T, q 2000 - 0000 UTC
U2	12/5	.0009	Rawinsonde u, v, T, q 2000 - 0000 UTC
U3	12/5	.0001	Rawinsonde u, v, T, q 2000 - 0000 UTC
U4	12/5	.0003	Rawinsonde T, q 2000 - 0000 UTC
U5	12/5	.0003	Rawinsonde u, v 2000 - 0000 UTC
P1	12/5	.0003	Profiler u, v, derived T 1900 - 0200 UTC
P2	12/5	.0003	Profiler u, v 1900 - 0200 UTC
P3	12/5	.0003	Profiler derived T 1900 - 0200 UTC
P4	12/5	.0003	same as P1, but fill domain with profilers
P5	12/5	.0003	same as P4, but time-smooth data
P6	12/5	.0003	error-free wind observations at every grid point
P7	12/5	.0003	same as P6 but nudge surface u, v, T and q 1900-0200 UTC

Table 7-2. RMS errors for simulated observations.

Surface winds	5%	Rawinsonde height (500 mb)	10 m
Surface temperature	0.3°C	Rawinsonde height (250 mb)	20 m
Surface RH	0.02	Rawinsonde temperature	0.4°C
Surface pressure	100 Pa.	Rawinsonde winds	12%
Profiler winds	5%	Rawinsonde RH	0.025
Profiler heights	0.5%		

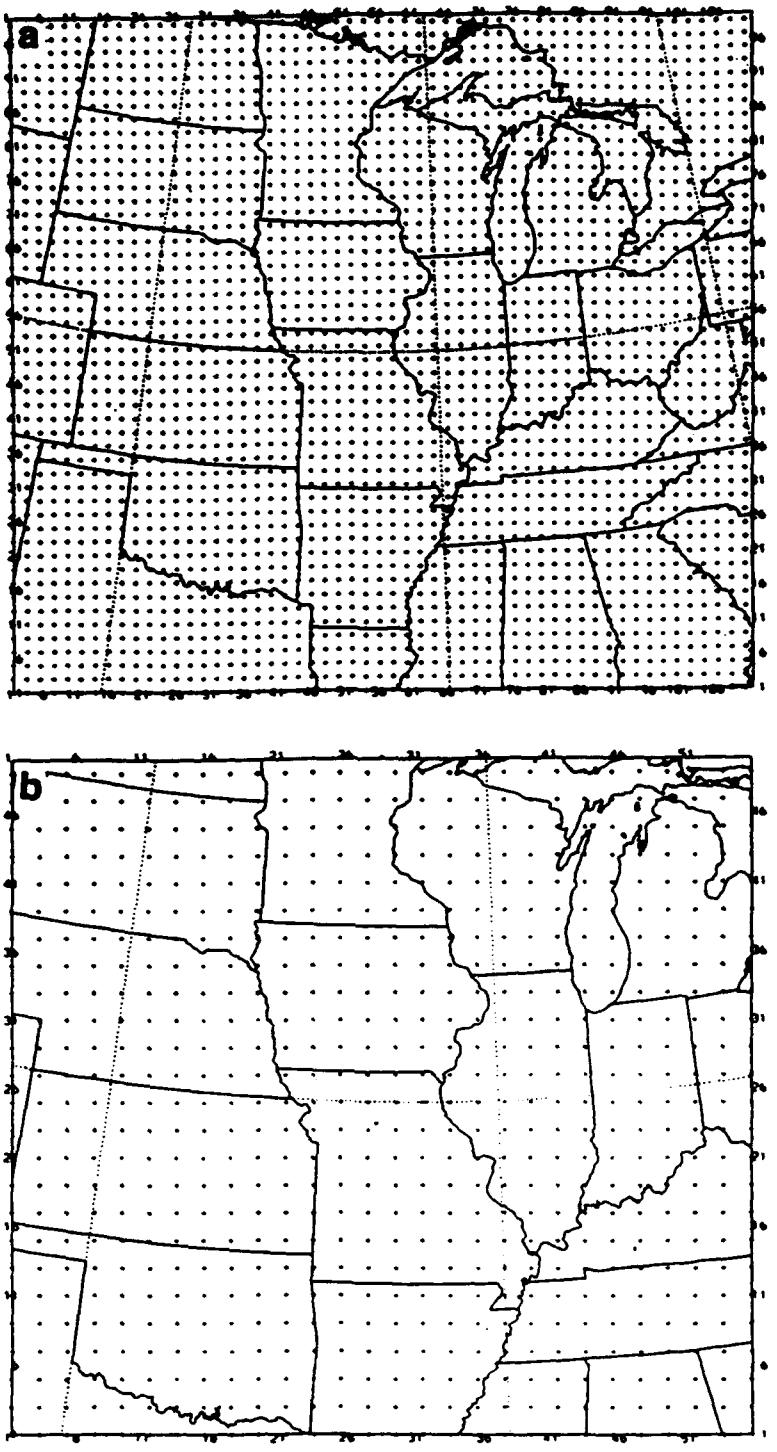

Figure 7-1 A depiction of the geographic area covered by the (a) coarse mesh and (b) fine mesh components of the OSSE.

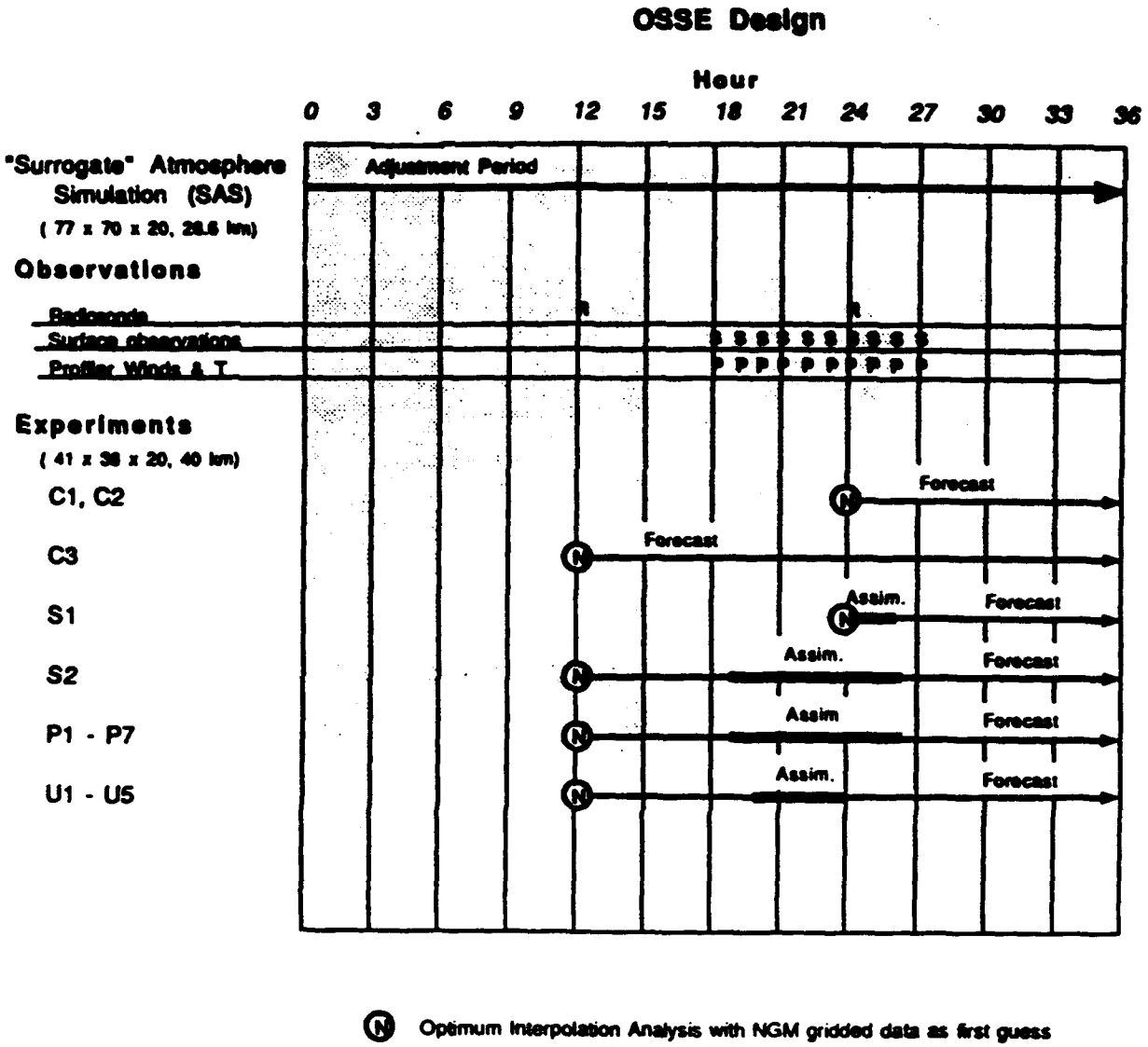

Figure 7-2 Schematic depicting OSSE design. A timeline chart which shows the types of data and a schedule for assimilating them into the MASS model during the Observation System Simulation Experiment (OSSE).

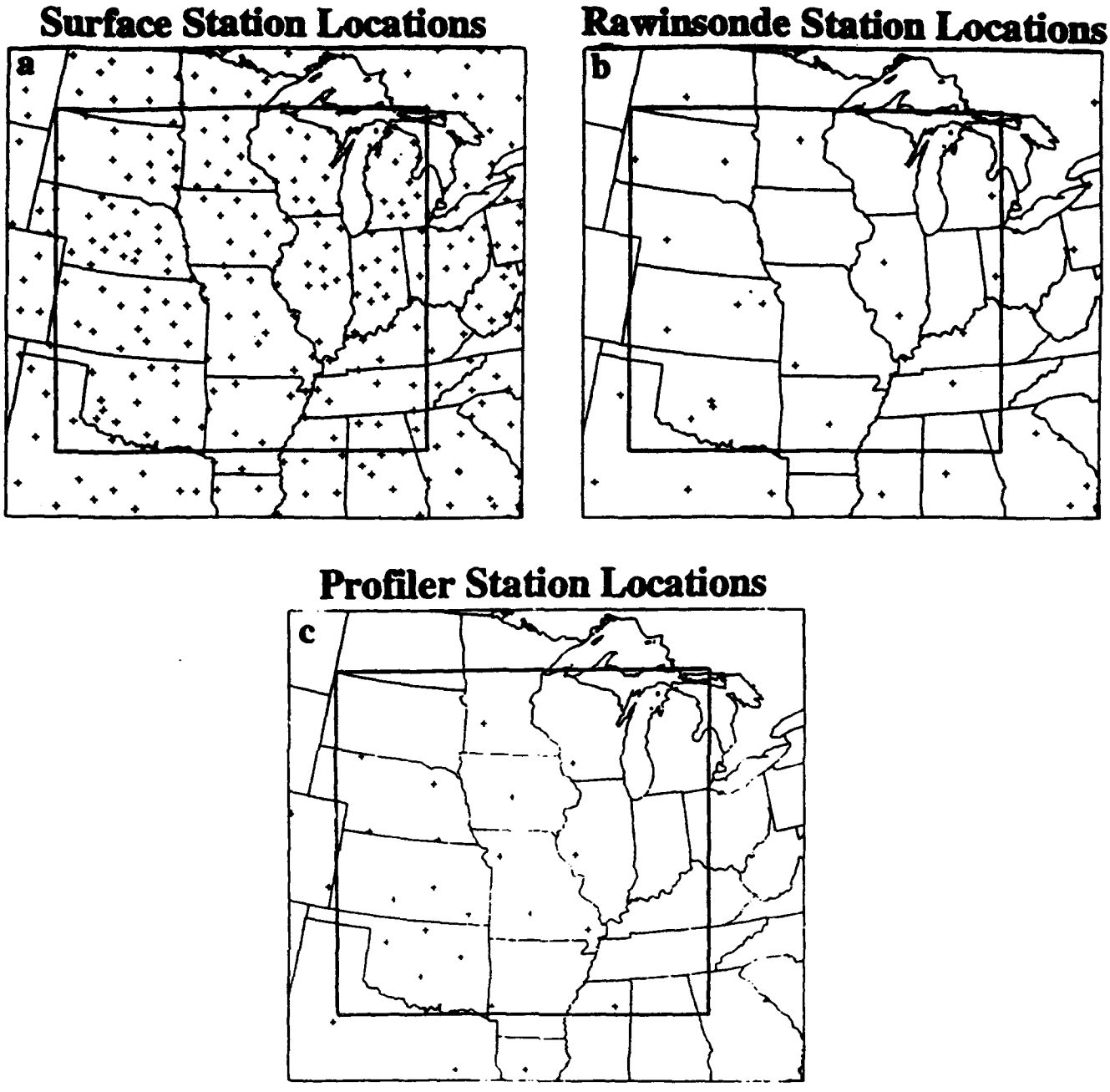

Figure 7-3 Locations of simulated (a) surface, (b) rawinsonde and (c) profiler observations used in the OSSE. Box encloses the 41 x 38 inner grid.

The experimental simulations were initialized with the simulated rawinsonde and surface data only. The first guess field for the data analysis was created from the observations themselves rather than from NGM or MASS model gridded data. This prevented the introduction of information other than that contained in the simulated observations. All experimental simulations used the 1200 UTC 5 September NGM simulation for boundary conditions.

Simulated rawinsonde, profiler and surface data were also objectively analyzed for the purpose of nudging. Gridded rawinsonde data was created at 1200 UTC 5 September and 0000 UTC 6 September. Simulated profiler winds were analyzed each hour between 1900 UTC 5 September and 0200 UTC 6 September. 3-D temperature fields derived from profiler winds (Cram, et al. 1991) were also available at those times. Finally, gridded surface data were analyzed at the same times as profiler data.

Seventeen experimental simulations were run and are detailed in Table 7-1 and Figure 7-2. Column 2 in the table refers to the initialization time (0000 UTC 6 September or 1200 UTC 5 September) and G in column 3 refers to the assimilation coefficient. Simulation C1 is the control simulation with only a static initialization at 0000 UTC 6 September. Simulation C2 tests the impact of the boundary conditions on the simulation. Simulation C3 is identical to simulation C1 except that it is initialized at 1200 UTC 5 September. Simulations S1 and S2 are 12 and 24 hour simulations, respectively, which assimilate surface data. Simulations U1, U4 and U5 assimilate various combinations of rawinsonde data (u, v, T, q). Simulations U2 and U3 test the effect of varying the data assimilation coefficient. G = .0003 implies an e-folding time of just under 1 hour for the relaxation of the model state to the "observed" state. Simulations P1, P2 and P3 test the assimilation of various combinations of profiler winds and derived heights. Simulations P4, P5 and P6 are attempts to improve the assimilation of profiler data including, adding profiler observations in regions which are not covered by the current network (P4), smoothing the profiler winds in time (P5) and creating a database of error free or "perfect" profiler observations at each model grid point (P6). Finally, simulation P7 assimilates all surface data, in addition to "perfect" profiler winds and temperature. The output from each simulation will be verified against the "true" values of the variables from the SAS.

The performance of the various experimental simulations were evaluated for a 12 hour period beginning at 0000 UTC 6 September. Because they are not directly assimilated, precipitation and surface pressure were used to assess the performance of each simulation. For purposes of simplicity, 0000 UTC 6 September will be referred to as 0 hours, 0600 UTC will be referred to as 6 hours, etc.

7.2 Review of the 6 September 1992 case

The case of the Midwestern squall line of 5-6 September 1992 was selected for the OSSE. A squall line developed ahead of a cold frontal boundary during the afternoon of 5 September and propagated eastward through the eastern plains states before dissipating by about 1200 UTC 6 September (Figure 7-4). At 0035 UTC (Figure 7-4a) the squall line extended from northwest Wisconsin to west Texas. It was unbroken along its northern and central sections while the southern part was broken. At 0035 and 0635 (Figure 7-4a, b), an unbroken line of precipitation extended from the Upper Peninsula of Michigan to Oklahoma. By 0935 (Figure 7-4c) the northern part of the squall line propagated to the western shore of Lake Michigan and began to dissipate, while intense convection developed in eastern Oklahoma at the southern end of the line. At 1235 (Figure 7-4d) only remnants of the squall line remained.

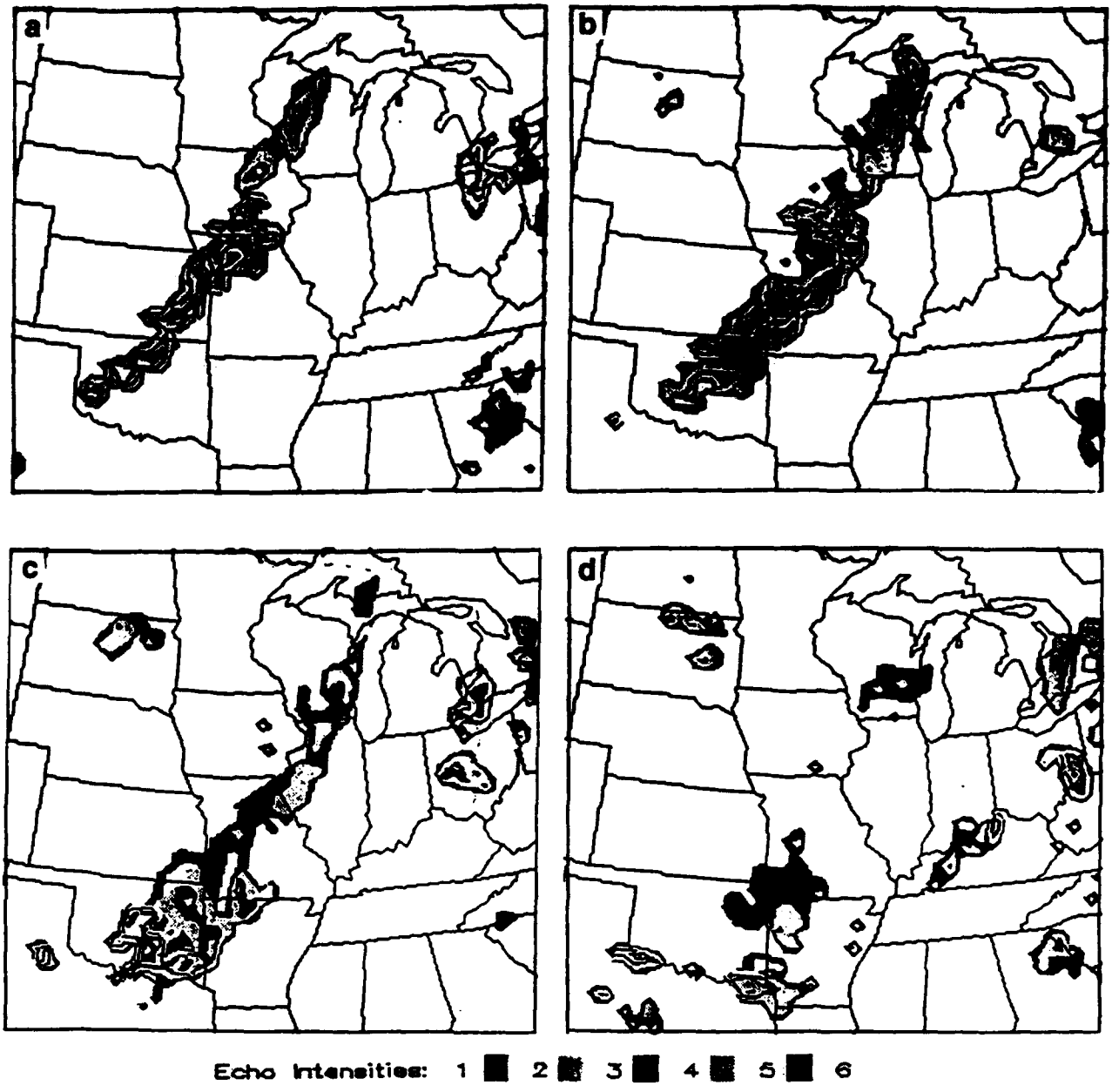

Figure 7-4 Manually-digitized radar plots for the OSSE. The times are (a) 0335, (b) 0635, (c) 0935, and (d) 1235 UTC 6 September. Each level of shading represents one VIP level.

7.3 The Surrogate Atmosphere Simulation

Figure 7-5 shows 3-hourly precipitation totals from the SAS during the period of interest. During the 12 hour period a squall line propagated eastward through the domain ahead of a cold front. Initially, the squall line was located along an axis which ran approximately from extreme southwestern Oklahoma to northwestern Wisconsin. Over the course of the simulation, the squall line propagated eastward several hundred kilometers while the northern part of the line dissipated after about 0600 UTC. A comparison of Figure 7-5 with Figure 7-4 shows a remarkable agreement between the SAS and Manually Digitized Radar plots for the same period.

7.4 Results

Several statistical scores are used to compare the various simulations. They include the 0.25 cm threshold precipitation threat scores for each 3 hour period and for the entire 12 hour period, and the root mean square (RMS) surface pressure, temperature and wind (average of u and v) errors at 0, 6 and 12 hours. Threat scores and RMS errors are calculated using a subset of the inner grid that does not include the four rows (or columns) of grid points nearest to each boundary. The threat score is determined by

$$TS = \frac{CFA}{(FA + OA - CFA)} \qquad (7\text{-}1)$$

where FA is the area where the precipitation is forecast to equal or exceed the threshold, OA is the area where the observed precipitation equals or exceeds the threshold, and CFA is the correctly forecast area or the region where both forecast and observed values exceed the threshold. Since the threat score penalizes a simulation for erroneously predicting precipitation either above or below the threshold value, a perfect score of 1.0, or even a near perfect score, is nearly impossible to attain. The relatively short 3 hour verification period in this study, combined with relatively high horizontal resolution, increases the challenge further. The 3 hour threat score presented here effectively test the model's skill at predicting meso-ß scale precipitation events in space and time.

7.4.1 Influence of boundary conditions

Figure 7-6 shows the surface pressure difference between simulations C1 and C2. At 3 hours, differences are relatively small except near the boundaries. By 6 hours, significant differences in surface pressure and in surface pressure gradient, as shown by gradients in the difference field, are evident throughout most of the model domain. These differences continue to increase through 12 hours. An examination of Table 7-3 shows that threat scores for the two simulations are similar through 6 hours. After that, simulation C2 deteriorates at 9 hours, although it outperforms simulation C1 during the final 3 hour period. Since the constant boundary conditions in C2 are certainly inferior to the boundary conditions in simulation C1, this can only be attributed to pure chance. At 6 hours, RMS wind and pressure errors for simulation C2 are somewhat larger than those for simulation C1. By 12 hours they are significantly larger. Surprisingly, temperature errors are smaller than for simulation C1. If any conclusion can be drawn from this information, it is that up until 6 hours differences between the experimental simulations are primarily due to differences in data assimilation. The influence of the boundary conditions becomes significant after 6 hours and continues to increase until 12 hours.

Surrogate Atmosphere Simulation

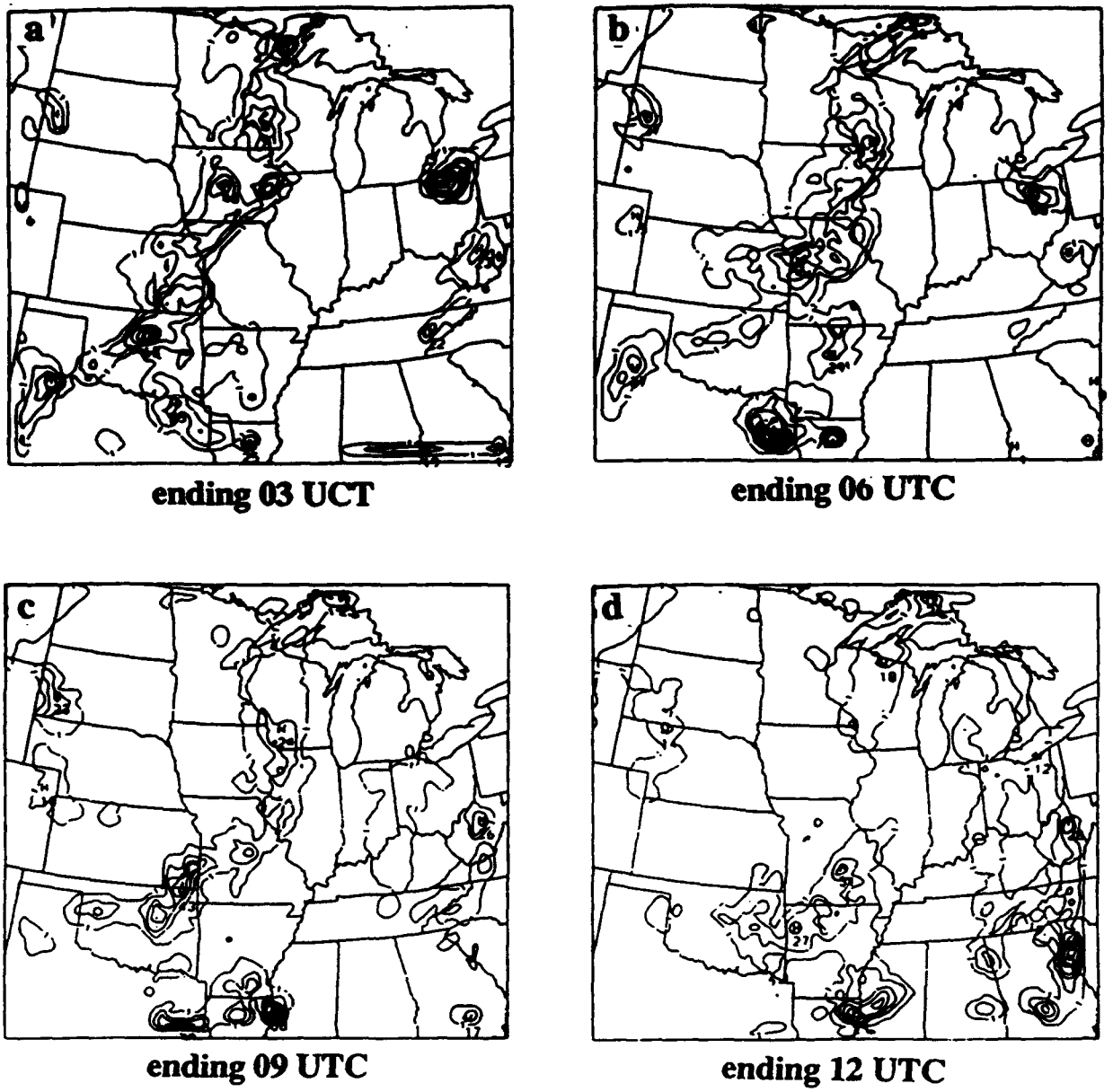

Figure 7-5 Three hour accumulated precipitation in hundredths of an inch ending at (a) 0300 UTC, (b) 0600 UTC, (c) 0900 UTC and (d) 1200 UTC 06 September 1992 for the surrogate atmosphere simulation. Contour interval is 0.10 in. starting at 0.01 in.

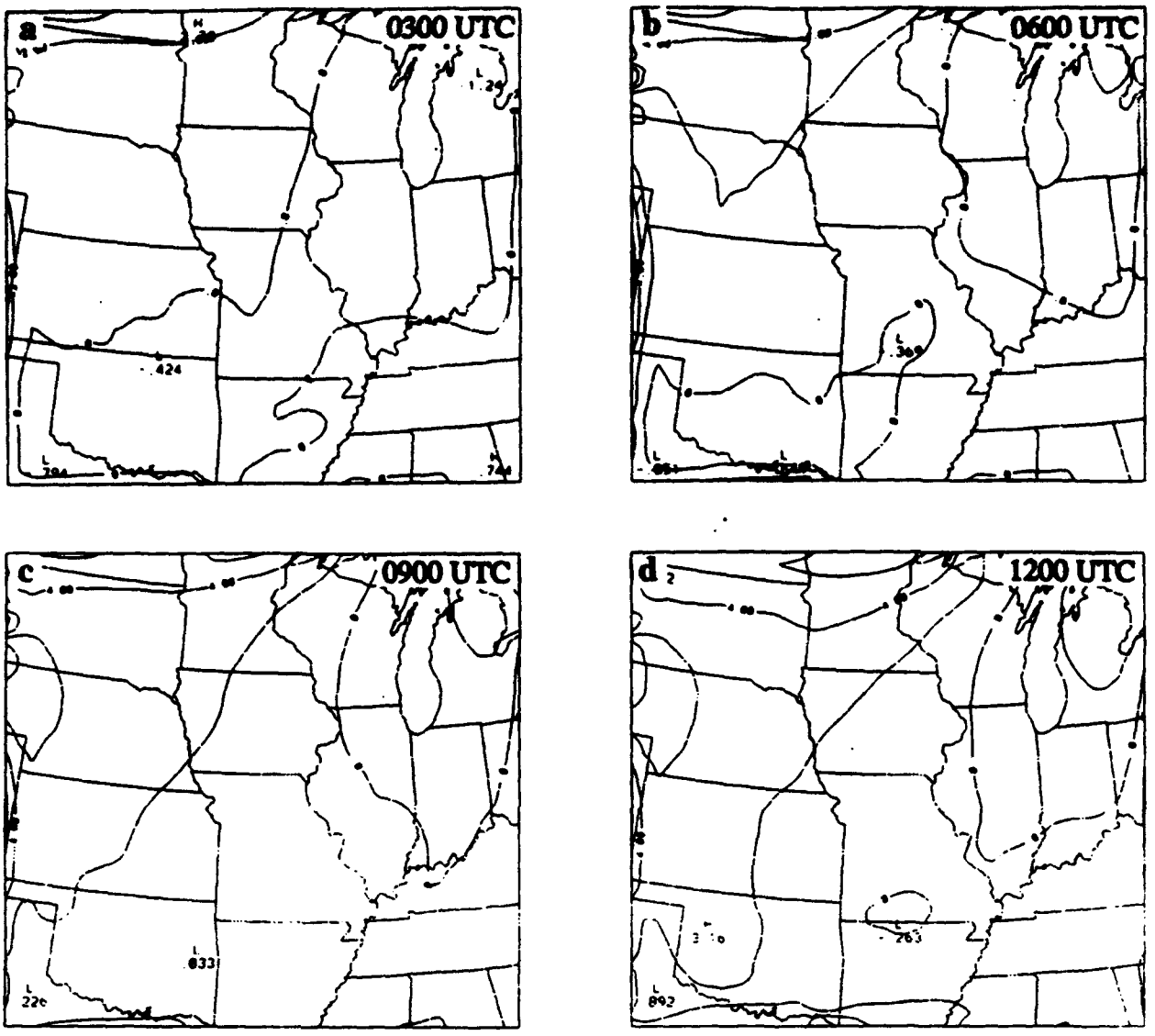

Figure 7-6 Surface pressure difference between simulations C1 and C2 at (a) 0300 UTC, (b) 0600 UTC, (c) 0900 UTC and (d) 1200 UTC 6 September 1992. Positive values indicate that pressure is higher in simulation C1.

7.4.2 Statistical evaluation

An examination of Table 7-3 shows that simulation S1 is virtually identical to simulation C1. The same can be said for simulation S2 and simulation C3. The assimilation of surface data has virtually no impact on the model's performance, at least for the case examined here. If simulation S1 is ignored, simulation C1, the control simulation, has the best overall threat scores. After 6 hours, simulation C1 outperforms all other experimental simulations. Before 6 hours however, several experiments which assimilate rawinsonde data are superior to simulation C1. These include simulation U1 and U2. Simulation U2 has the best overall performance during this period. Simulations U3, U4 and U5 performed poorly relative to simulation C1 except during the first period. These three simulations did produce a better forecast than simulation FC which was initialized at the same time but did not include any nudging. This indicates that the assimilation of data with a weaker nudging coefficient (0.0001) or the assimilation of only wind or only mass data, *do* improve the simulation of precipitation slightly, although not enough to outperform simulation C1 which is initialized 12 hours later. Simulations P1 through P6 showed little, if any, improvement over simulation C3. Simulation P7 was substantially better than simulation C3, although the precipitation was not simulated as well as simulation C1, U1 or U2.

7.4.3 Discussion

An examination of Table 7-3 and Figure 7-7 shows that simulation C1 (the control simulation) suffers from a precipitation spin-up problem. Bias scores for the first 3 hour period (not shown) confirm that the total area of precipitation is significantly smaller (0.66 for 0.1 cm threshold and 0.53 for 0.25 cm) than for the SAS, while for many of the nudged simulations the bias scores are significantly closer to 1.0. After the first period, simulation C1 generally performs as well as or better than any of the other simulations, especially after 6 hours when the threat scores for simulations with upper air nudging drop to near 0. A subjective comparison of the precipitation field from simulation C1 (Figure 7-7) with that from the SAS (Figure 7-5) shows that

Table 7-3. Threat scores and RMS errors for experimental simulations.

Exp.	0.10 in. Threat Scores					RMS Errors								
						0 h			6 h			12 h		
	0-3 h	3-6 h	6-9 h	9-12 h	0-12 h	u, v ms^{-1}	T K	P mb	u, v ms^{-1}	T K	P mb	u, v ms^{-1}	T K	P mb
C1	0.10	0.30	0.24	0.27	0.57	1.80	0.58	0.48	2.31	0.92	0.91	2.47	1.15	1.37
C2	0.10	0.29	0.19	0.34	0.54	1.80	0.58	0.48	2.71	0.90	1.01	3.71	1.05	1.82
C3	0.13	0.10	0.03	0.00	0.22	2.39	1.20	0.83	2.95	1.44	1.13	3.93	1.58	1.72
S1	0.10	0.31	0.23	0.24	0.58	1.80	0.58	0.48	2.31	0.93	0.91	2.47	1.14	1.37
S2	0.13	0.12	0.02	0.00	0.20	2.28	1.13	0.76	-----	-----	-----	-----	-----	-----
U1	0.26	0.31	0.07	0.00	0.41	2.21	0.88	0.69	2.68	1.07	0.84	3.63	1.42	1.50
U2	0.28	0.39	0.08	0.01	0.46	2.33	0.86	1.01	2.68	1.02	0.84	3.64	1.40	1.47
U3	0.24	0.14	0.02	0.00	0.27	2.14	0.95	0.64	2.75	1.24	0.96	3.73	1.50	1.57
U4	0.18	0.18	0.09	0.00	0.38	2.38	0.85	0.53	2.76	1.18	0.92	3.70	1.45	1.50
U5	0.15	0.15	0.01	0.00	0.20	2.18	1.26	1.20	3.06	1.30	0.94	3.83	1.55	1.62
P1	0.11	0.10	0.06	0.00	0.20	2.06	1.20	0.93	2.82	1.27	0.97	3.70	1.53	1.60
P4	0.15	0.12	0.01	0.00	0.32	2.02	1.28	0.86	2.92	1.22	1.01	3.65	1.49	1.61
P5	0.16	0.12	0.02	0.00	0.32	2.02	1.27	0.88	2.91	1.22	1.01	3.65	1.49	1.61
P7	0.06	0.26	0.12	0.00	0.24	1.08	0.87	0.77	2.46	1.03	0.96	3.64	1.41	1.51

Simulation C1

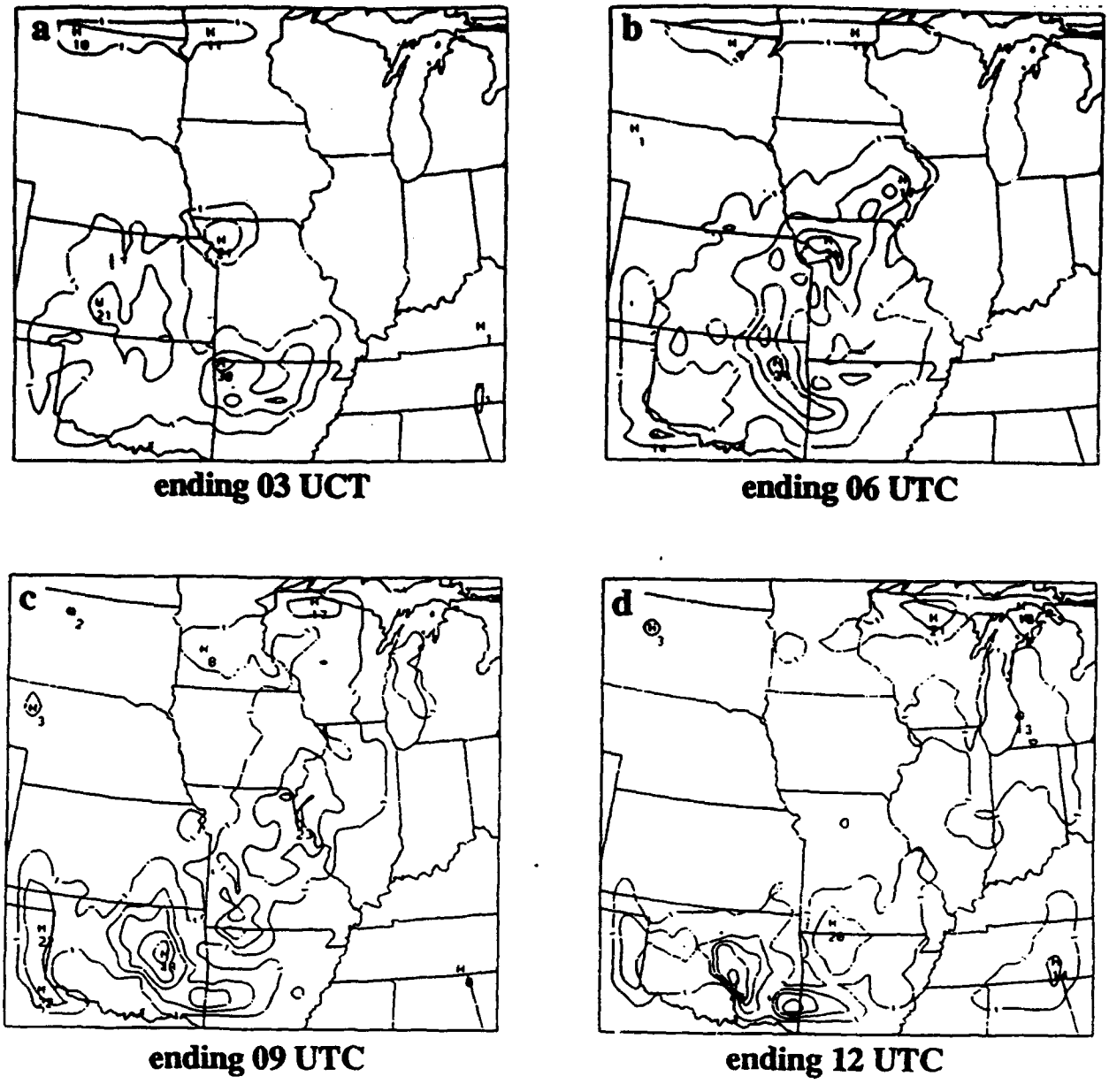

Figure 7-7 Three hour accumulated precipitation in hundredths of an inch ending at (a) 0300 UTC, (b) 0600 UTC, (c) 0900 UTC and (d) 1200 UTC 06 September 1992 for simulation C1. Contours as in Figure 7-5.

during the first 6 hours, simulation C1 fails to generate precipitation along the northern part of the squall line. After 6 hours, the general representation of the precipitation field is good, although specific details such as the heavy precipitation in southeast Kansas between 6 and 9 hours, or in southeast Missouri between 9 and 12 hours, are missed by simulation C1.

Simulation S1, which assimilates surface data, is nearly identical to simulation C1. The same is true for simulations S2 and C3. This implies that in this case and others where the majority of the forcing is on the synoptic scale, surface nudging alone has little or no beneficial effect.

Unlike surface nudging, upper air nudging (simulations U1 through U5) has a considerable effect on the simulations. The precipitation field from simulation U2 is shown in Figure 7-8. Up until 6 hours, simulation U2 does a remarkable job of simulating the precipitation from the SAS. Simulation U1 (not shown) does nearly as well. The stronger nudging coefficient in simulation U2 results in a less balanced state at 0 hours as evidenced by larger RMS pressure and wind errors. By 6 hours though, errors for the two simulations are similar. Still, it is not inconceivable that under some circumstances, the stronger nudging coefficient in simulation U2 may cause problems by pushing the simulation too far out of balance. Threat scores for simulation U3 indicate that a nudging coefficient of 0.0001 is too small to adequately introduce rawinsonde data into the simulation. Simulation U4 which assimilates temperature and moisture only and simulation U5, which assimilates winds only, both perform rather poorly. It seems that, at least for the present case, *both* the wind and mass fields need to be assimilated to improve the simulation.

After 6 hours, simulations U1 and U2 weaken the squall line too quickly and develop phase errors. In fact, simulation C1 outperforms all nudged simulations after 6 hours. In fact, RMS errors for simulations U1 through U5 are larger throughout the period of interest, except in the case of surface pressure at 6 hours. It seems that rawinsonde nudging improves the simulation during the first 6 hours by eliminating the spin-up problem. Simulation U1 also provides a more balanced initial state as shown by the fact that the RMS surface pressure error increases by only 0.13 mb in the first 3 hours compared to 0.50 mb for simulation C1. After 6 hours, larger initial RMS wind and mass field errors contribute to a degradation of simulations U1 and U2.

The assimilation of simulated profiler data produced disappointing results. The squall line lagged several hundred kilometers behind its "observed" position in simulation P1 (not shown). Threat scores are poor throughout the simulation. RMS errors are larger than for simulation U1 except for winds at 0 hours.

Two possible explanations for the poor performance are: (1) the profiler network extends over only a portion of the model domain (Figure 7-2c). The only result of profiler nudging for the regions outside the profiler network is that there are 12 additional hours during which error growth can occur. (2) the profiler network suffers from an inconsistency between low spatial and high temporal resolution. This problem is exacerbated because the simulated profiler data was created from a single observation time, unlike the actual profiler network which averages 5 minute data to produce hourly observations. The result is a temporally noisy analysis which is then nudged into the simulation.

Several experimental simulations were run to test these possibilities. In simulation P4, additional simulated profiler stations were added so that the entire model domain was adequately covered by the data. Simulation P5 was identical to simulation P4, but a time smoother was applied to the data to remove features which occurred on a time scale of less than three hours. Neither produced any significant improvement over simulation P1 (see Table 7-3). As a final test, simulated profiler data was extracted at each model gridpoint (simulation P6). For this simulation, the RMS errors were set to 0 (see Table 7-2), and the time tendency term was not ignored in the derivation of temperatures from the wind field. Even with "perfect " profiler data at every model gridpoint, there was no significant improvement on simulation P1. Simulation P7 was identical to simulation P6 with the addition of nudging to surface wind, temperature and moisture. This simulation was the only one for which profiler nudging produced a squall line in approximately the same location as for the SAS. Even so, the statistics for simulation P7 are considerably worse than

Simulation U2

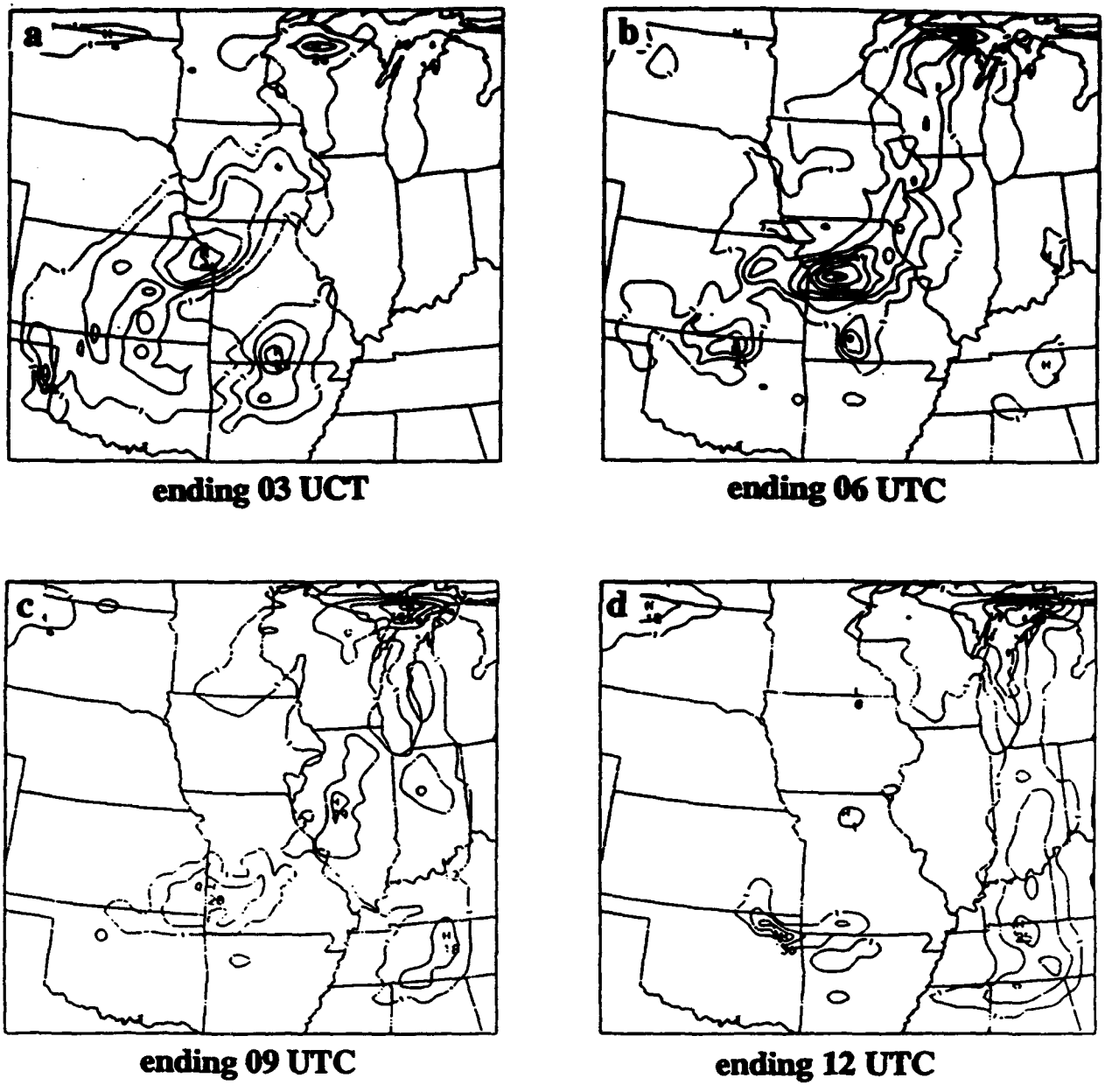

Figure 7-8 Three hour accumulated precipitation in hundredths of an inch ending at (a) 0300 UTC, (b) 0600 UTC, (c) 0900 UTC and (d) 1200 UTC 06 September 1992 for the simulation U2. Contours as in Figure 7-5.

those for simulation U1.

Given that the simulated profiler wind field was essentially perfect, the one remaining explanation for the poor performance of profiler data assimilation relative to rawinsonde data assimilation is the method of deriving the temperature field from the wind field. Figure 7-9 shows the 700 mb temperature analyses from the simulated rawinsonde temperature observations, the temperature fields derived from the simulated "standard" profiler wind observations used in simulation P4 and from the "perfect" profiler wind observations used in simulations P6 and P7. The figure also shows the "verification" from the SAS. At 700 mb, all of the analyses underestimate the temperature in the warm tongue which extends from Oklahoma into Wisconsin. The standard profiler analysis underestimates the temperature the most followed by the perfect profiler analysis and the rawinsonde analysis. The temperature field derived from the "perfect" profiler analysis resolves the small scale feature from the SAS very well, although the temperatures are everywhere about 2 K colder than the SAS. The temperature field from the standard profiler observations resolves the details of the SAS temperature field substantially better than the rawinsonde analysis, but does not show some of the smaller scale features evident in the perfect analysis. It too is generally several degrees too cold. The rawinsonde analysis is the smoothest of the three; however, it underestimates temperatures the least, especially in the tongue of warm air which extends from Oklahoma to Wisconsin. At 350 mb (not shown), the profiler analyses tend to overestimate the temperature relative to the SAS while the rawinsonde analysis, although it doesn't reveal as many details, shows no bias in the temperature field. The net result of the bias introduced into the temperature field by nudging to derived profiler temperature field is that the lapse rate is reduced in and around the squall line (Figure 7-10) which may explain the poor performance when profiler data is assimilated.

What is the reason for the excellent representation of small scale features in the derived profiler temperature field, but the large overall bias? When the temperature field is derived from the profiler wind fields, the technique of Cram et al. (1991) actually calculates the height field. Two possible sources of error are (1) the source of the height field used for boundary conditions and (2) the amplification of small height errors when the temperature field is calculated from the thickness equation. In the derivation of temperatures from the perfect profiler data, model output from the SAS was used for boundary conditions. This rules out (1). (2), however, deserves some consideration. Three dimensional nudging data was analyzed on pressure surfaces spaced every 50 mb (about 500-1000 m) in the vertical. Therefore, a 5 to 10 meter error in the height field at any one pressure level would produce about a 1% error in the thickness between analysis levels or about a 2 to 3 K error in the temperature field! It appears that the technique for deriving the temperature field from the wind field produces a temperature analysis that is considerably poorer than the rawinsonde temperature analysis. Perhaps there is a way to merge profiler wind data with rawinsonde temperature data, although initial attempts at this have not produced good results.

The addition of surface nudging is all that distinguishes simulation P7 from simulation P6, but there is a significant difference between the two simulations. Simulation P7 is the only "P" series simulation in which the squall line is well represented during any part of the verification period (not shown). One possible explanation is that the nudging of surface temperature observations into the PBL helps to overcome the tendency of profiler temperature nudging to stabilize the atmosphere. When surface temperature nudging is added, all gridpoints within the model-defined PBL are nudged to surface data rather than to the "perfect" profiler data. Of course, wind or moisture nudging in the PBL may have also played a role. In any case, the combination of surface nudging and rawinsonde nudging (not shown) produces nearly identical results to that of rawinsonde nudging alone. So it appears that the surface data is helpful only because it compensates for a weakness in the profiler nudging and not because it contains any information which enhances a situation in which the upper level dynamics are well represented.

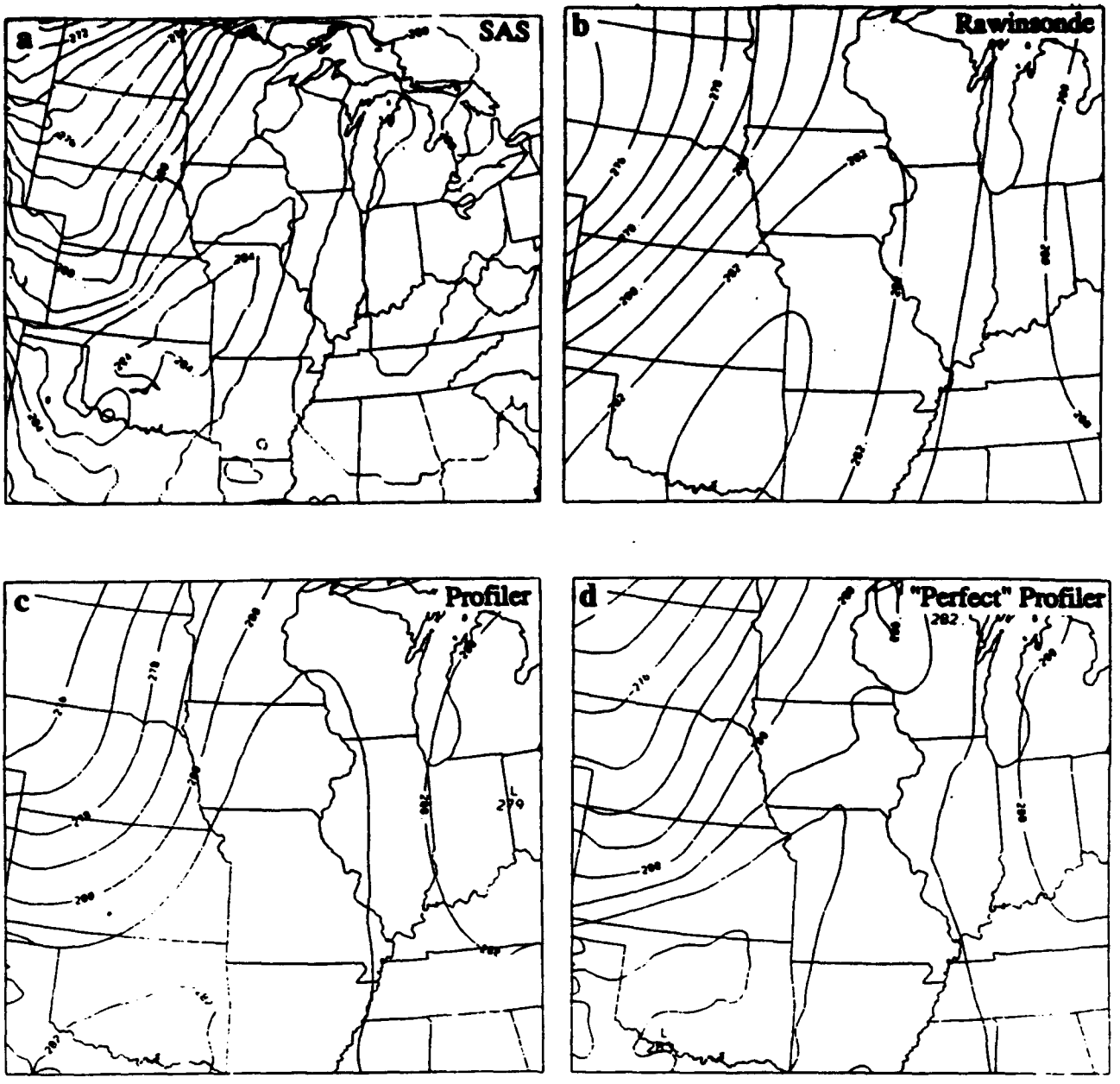

Figure 7-9 700 mb temperature (K) valid at 0000 UTC 06 September 1992 (a) from SAS, (b) from simulated rawinsonde analysis, (c) derived from simulated wind profiler analysis and (d) derived from simulated "perfect" wind profiler analysis. Contour interval is 1 K.

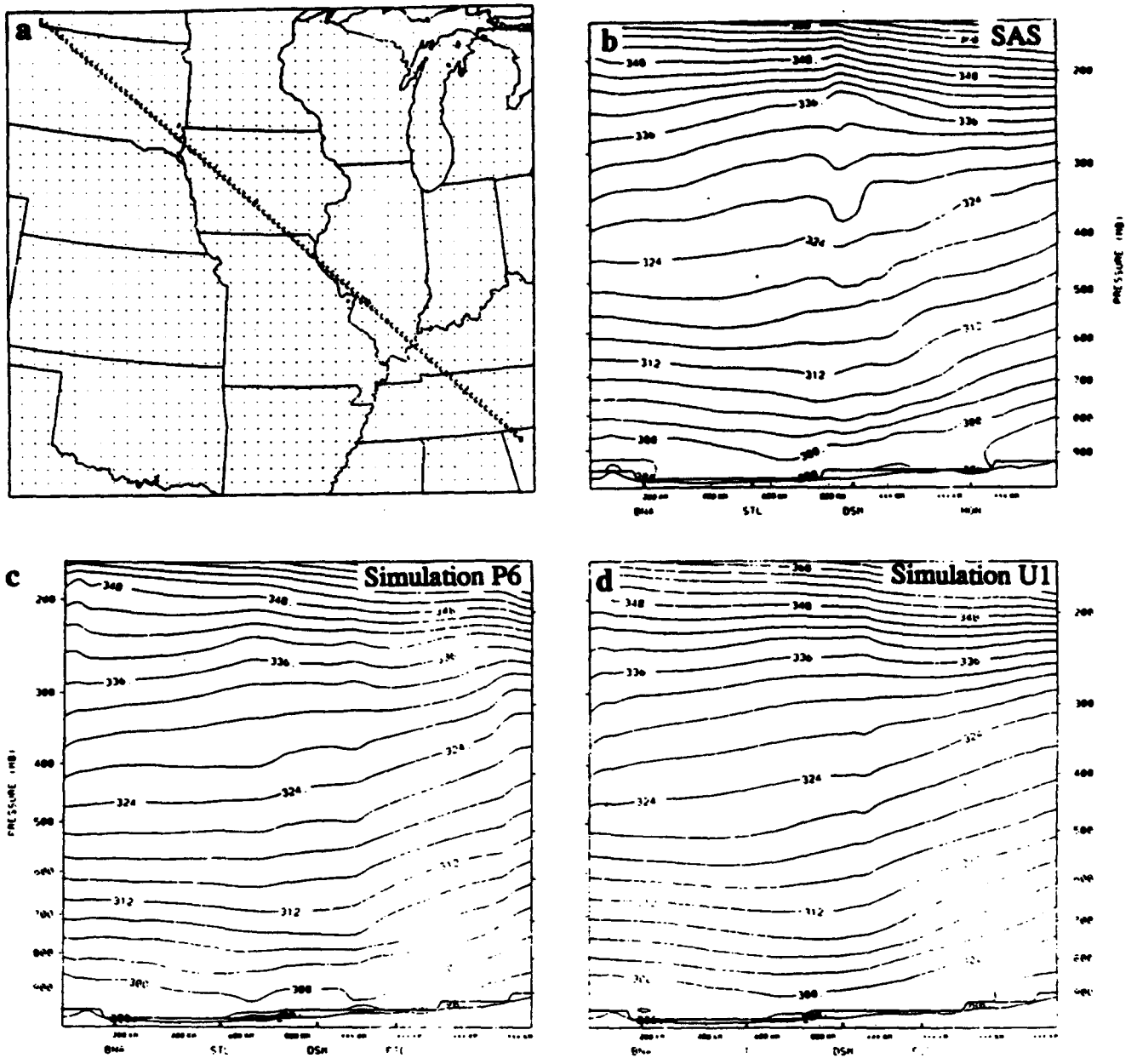

Figure 7-10 Vertical cross section of potential temperature (K) at 0000 UTC 6 September 1992 along the path indicated in (a). Cross-sections are from (b) the SAS, (c) simulation P6, and (d) simulation U1. The left edge of (b), (c) and (d) correspond to the southeast edge of the path in (a). Contour interval is 3 K.

7.5 *Conclusions*

The results of the OSSE indicate that the main benefit of nudging is in the reduction of the spin-up problem during the initial 3 to 6 hours of a simulation. After this time, nudged simulations are inferior to a statically initialized simulation because the nudged simulation must be initialized 12 hours earlier, at least with the current availability of complete 3-dimensional observational datasets. The results of the case of 5-6 September 1992 indicate that the assimilation of rawinsonde data produces the greatest improvement, while surface data is less valuable and profiler data suffers from a lack of information about the mass field. Since the OSSE consisted of only 1 case, these results are not necessarily true for all conceivable situations. For cases with weak forcing, the assimilation of rawinsonde data may be less important while surface data assimilation may have a greater impact. Stauffer et al. (1991) found this to be true in their weak synoptic forcing case.

An important consideration in the assimilation of surface data is that the state of the PBL, especially temperature, responds to external forcing on very short time scales. For this reason, if the forcing functions in the PBL are not properly simulated, the assimilation of surface data into the PBL may improve the surface representativeness of the model PBL only until the nudging period ends. It may be more valuable to concentrate on accurately representing atmospheric transmissivity, soil moisture and other variables which determine the surface forcing function. The assimilation of Manually Digitized Radar (MDR) data and the synthetic relative humidity scheme (see Sections 6.4 and 6.5), which unfortunately could not be tested in an OSSE, may help to improve the model's representation of cloud cover which implies a better representation of the radiative component of the surface forcing function. It may also be useful to adjust the vertical structure of the assimilation of surface data into the PBL to the particular PBL structure (free convection, stable, etc.) assigned by the Blackadar PBL scheme at each gridpoint. This would be consistent with Stauffer et al., (1991) who emphasized that the method of assimilation of surface data must not conflict with the model PBL physics.

The assimilation of profiler data could prove to be quite valuable if a method of removing the temperature bias in the derived temperature field could be derived. One such method is to use rawinsonde temperature observations to anchor the profiler derived temperature field. Unfortunately, rawinsonde data is typically available only every 12 hours compared to every hour for profiler data. Still, if the temperature biases are relatively constant with time, it may be possible to remove the temperature bias from the 1200 and 0000 UTC profiler observations and then apply the same corrections to other times. If this technique is not successful, it will be necessary to wait until 3-dimensional temperature data is available at the same frequency as profiler wind data.

Given an abundance of time an other resources, OSSEs have the potential to expand understanding of data assimilation much more than the limited experiment presented here. Several potentially valuable experiments must wait for another opportunity. They include:

1) The use of observations from the SAS, rather than output from a numerical model, to provide boundary condition information. This may help to reduce the degradation of the simulation which occurs when forecast boundary condition data propagates into the domain during the data assimilation period.
2) Creating a technique to simulate MDR, IR satellite and other non-standard data from the SAS so that the MDR assimilation scheme and the synthetic RH scheme could be tested.
3) Testing the effects of temporal and spatial distribution of the simulated observations on the simulation.

8. Results of 36-Case Evaluation

Many significant changes to the model physics have been made in the course of this project. In order to evaluate the state of the entire MASS system at the end of the project, a large sample of mesoscale simulations were carried out. The simulations have been evaluated both objectively (Section 8.2), and on a subjective basis (Section 8.3).

8.1 Design of Evaluation Sample

Since the objective was to evaluate the preprocessor and model in general, a set of experiments was designed to examine the model using a broad sample of cases. There were two factors which were varied to achieve the desired diversity: time of year and geography. First, three sets of dates were selected for simulation. Table 8-1 lists the dates for the 36-case simulations. One winter and two summer cases were chosen to test the model under different meteorological regimes. The criteria for choosing these dates were that MESO possessed relatively complete sets of raw data, and that meteorologically-interesting events occurred. For each of the nine dates, simulations were conducted over four different regions of the country. Each simulation involved a 24 hr large scale run with a grid spacing of 50 km, beginning at 0000 UTC on the day of simulation, followed by a 12 hr nested simulation with a grid spacing of 15 km, beginning at 1200 UTC. Table 8-1 lists the names assigned to the various model domains, and Figures 8-1 through 8-4 show these grids. In order to closely examine the performance of the model (especially various aspects of the surface parameterization), five diagnostic points were chosen for each region (also listed in Table 8-1 and shown in Figure 8-5). At each of these points, the model's SRPH scheme diagnostics were turned on so that a large set of surface information was printed to files as the runs progressed. This data is used in the discussions of individual cases below.

Table 8-1 Characteristics of the 36-Case Sample

Dates of Simulations	
Dates (all 1992)	Key Meteorological Event
August 22, 23, 24	Hurricane Lester in Southwest
September 13, 14, 15	MCC in Iowa
December 10, 11, 12	Big Northeastern Snowstorm
Domain Names	
Large Scale	Nest
Northeast	New York
Southeast	Gulf
Southwest	New Mexico
Great Plains	Illinois
Diagnostic Locations	
Domain	Locations
Northeast-New York	Albany, NY (ALB) Bradford, PA (BFD) Boston, MA (BOS) New York, NY (LGA) Rochester, NY (ROC)
Southeast-Gulf	Greenwood, MS (GWO) Macomb, MS (MCB) Montgomery, AL (MGM) New Orleans, LA (MSY) Pensacola, FL (PNS)
Southwest-New Mexico	Carlsbad, NM (CNM) El Paso, TX (ELP) Holloman AFB, NM (HMN) Los Cruces, NM (LRU) Truth-or-Consequences, NM (TCS)
Great Plains-Illinois	Columbia, MO (COU) Chicago, IL (MDW) Evansville, IN (EVV) Moline, IL (MLI) West Lafayette, IN (LAF)

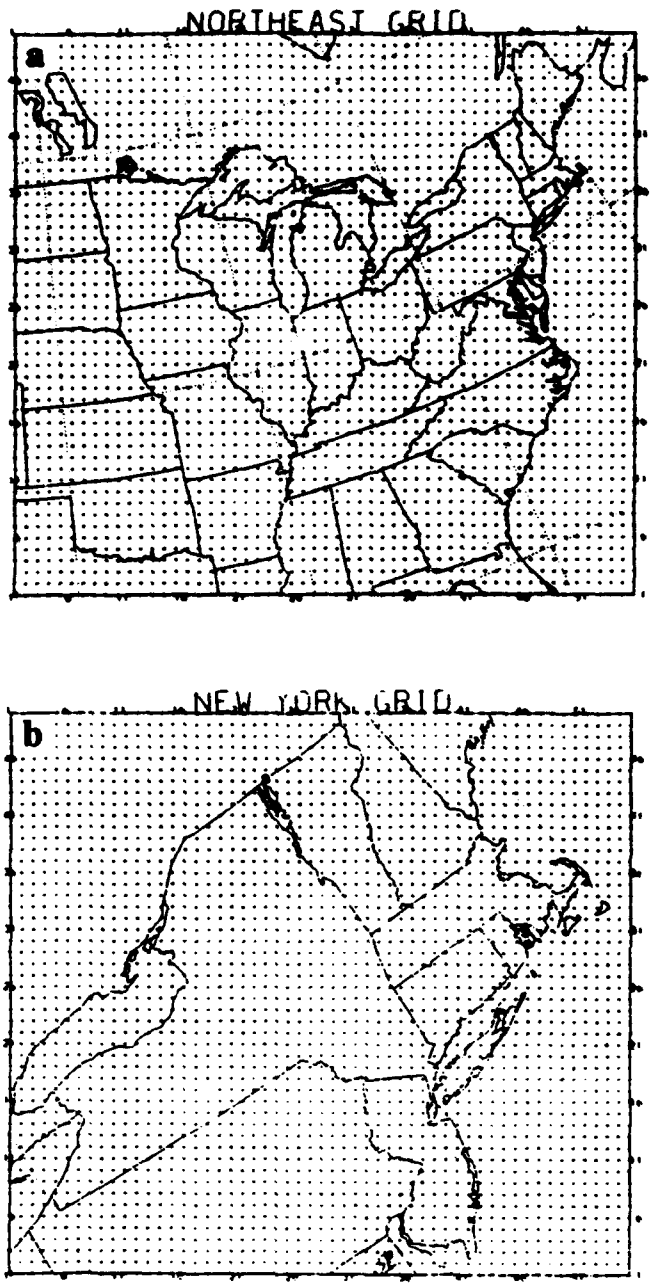

Figure 8-1 (a) Large scale and (b) nested grid domains for the Northeast and New York grids.

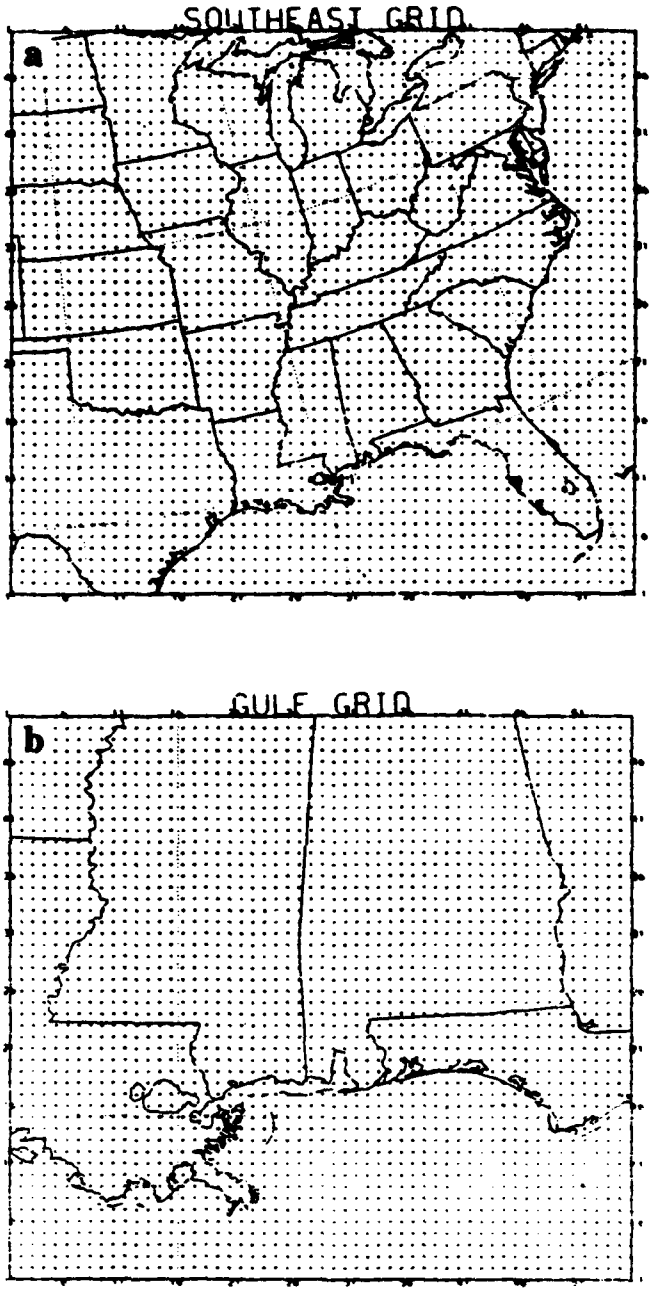

Figure 8-2 (a) Large scale and (b) nested grid domains for the Southeast and Gulf grids.

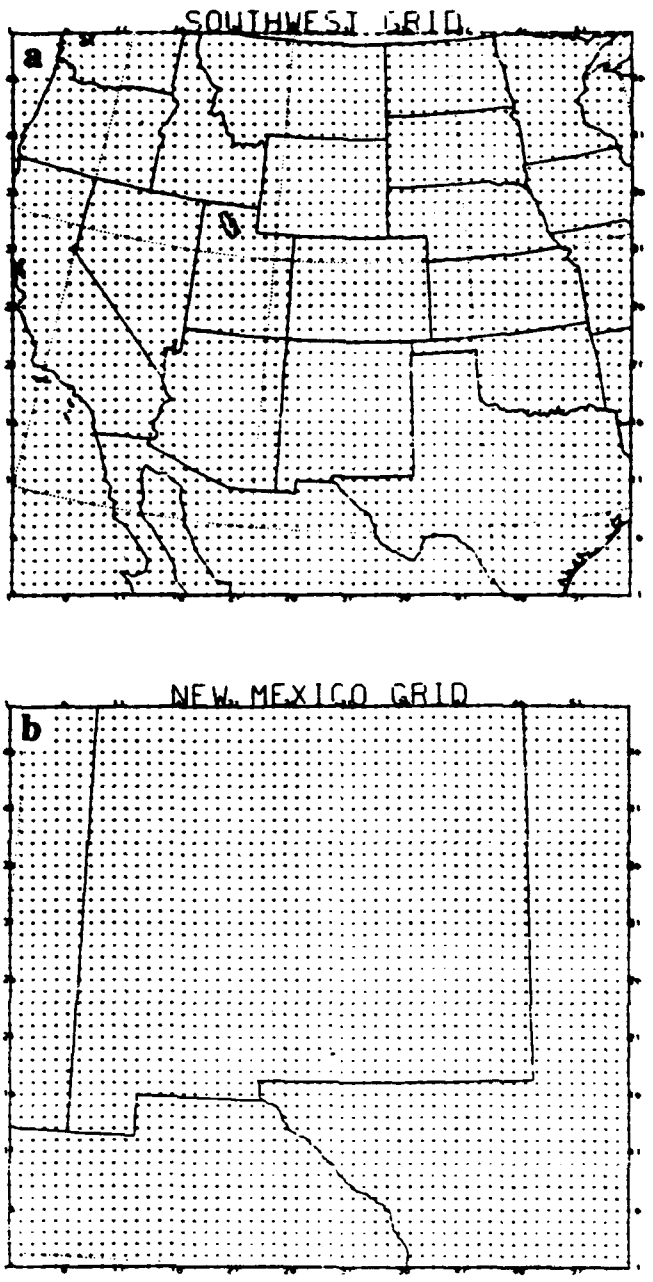

Figure 8-3 (a) Large scale and (b) nested grid domains for the Southwest and New Mexico grids.

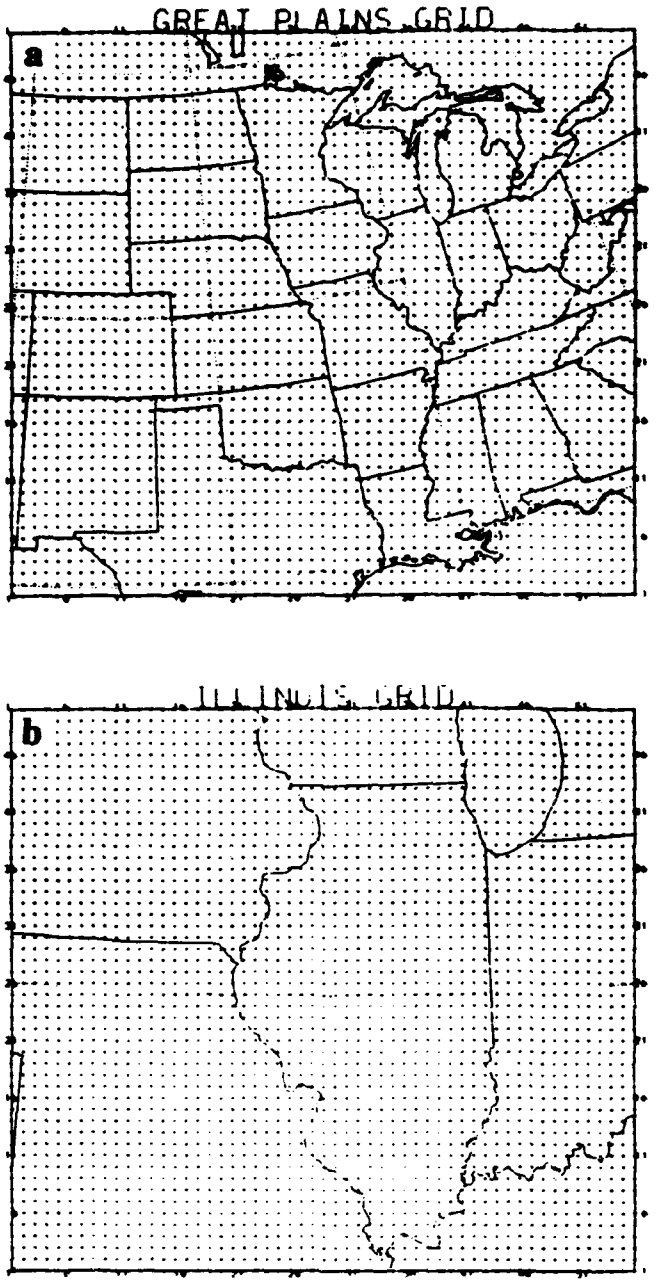

Figure 8-4 (a) Large scale and (b) nested grid domains for the Great Plains and Illinois grids.

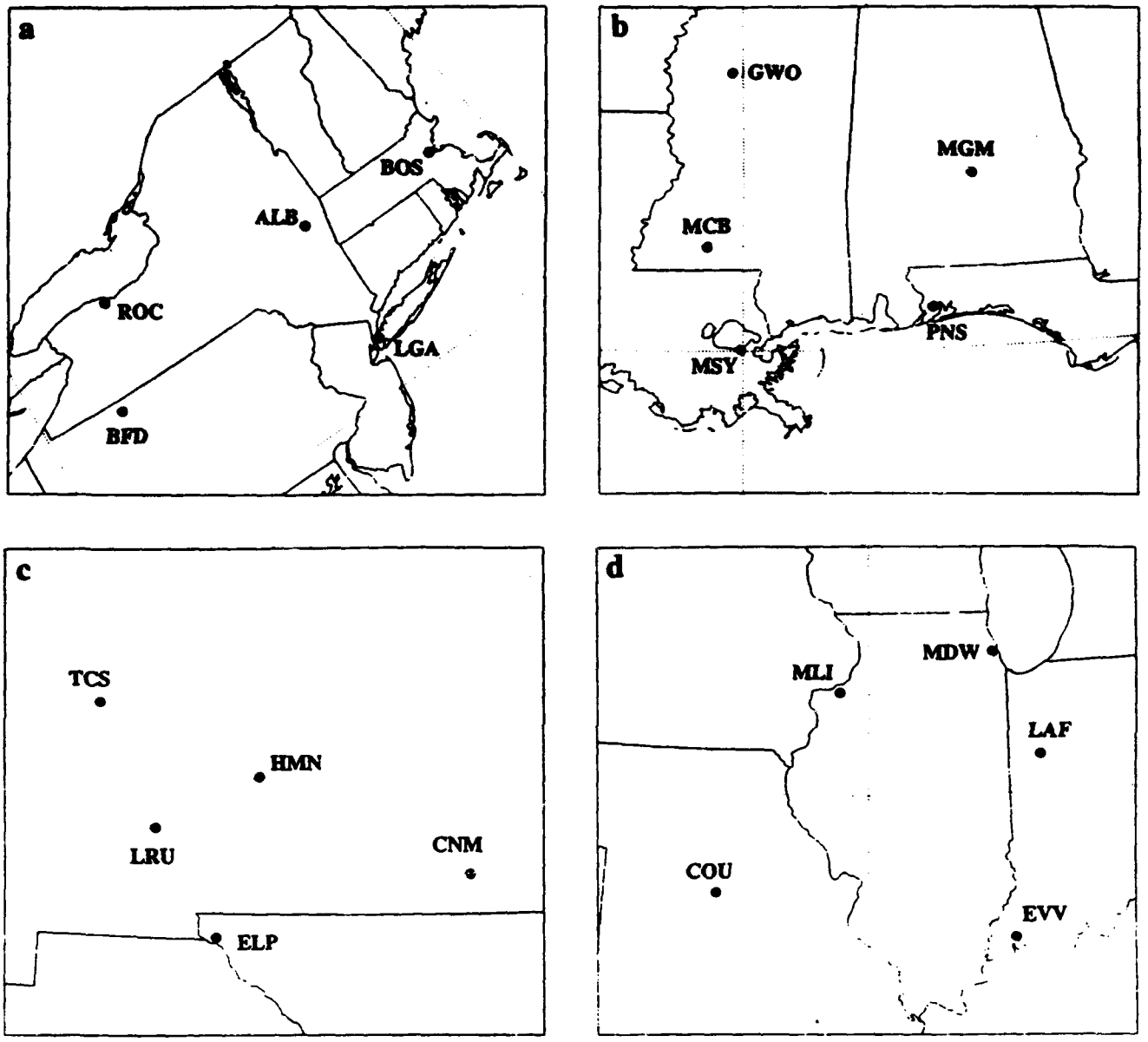

Figure 8-5 Location of diagnostic points for (a) Northeast-New York, grid, (b) Southeast-Gulf grid, (c) Southwest-New Mexico grid, and (d) Great Plains-Illinois grid.

8.2 *Statistical Evaluation*

In order to provide an objective picture of the performance of the entire MASS preprocessor and modeling system, a statistical analysis of the 36-case sample was conducted. The parameters used for evaluation are the root-mean-square (RMS) and bias errors of various meteorological variables (pressure, temperature, dew point, wind speed and wind direction), and precipitation THREAT scores. The THREAT score is computed by comparing observed station precipitation with model precipitation at nearby points. It is given as

$$\text{THREAT} = \frac{\text{CF}}{\text{O} + (\text{F} - \text{CF})} , \qquad (8\text{-}1)$$

where CF is the number of station locations (THREAT scores are often calculated from areas or numbers of model grid points rather than station locations) at which the model has correctly forecasted a given amount of precipitation over a specified time period, O is the observed number of stations which meet the same criteria, and F is the total number of stations which the model predicts to meet the criteria (both correctly and incorrectly). The THREAT score both rewards correct forecasts and penalizes incorrect forecasts (the term in parentheses in the denominator), so it is a stringent test of forecast ability. A THREAT score of one would represent a perfect forecast.

The data was compiled in various ways in an attempt to give insight into the characteristics of the model. First, the statistical data from each of the case studies was averaged for each of the eight different grids (four large scale and four nested). Figure 8-6 shows the RMS and BIAS errors for pressure for each of the eight grids. The BIAS plot shows that the pressure is systematically decreasing on every grid. This represents a loss of mass over the entire grid; it is a characteristic problem in limited area models. The problem is especially significant for the nested grids, because the mass flux across the domain boundaries is very sensitive to the formulation of the lateral boundary conditions. Figure 8-7 shows the temperature characteristics of the model. The Southwest and New Mexico grids have the largest errors, and also tend to be too cold. The probable reason for this is that in mountainous terrain, meteorological stations tend to be located in population centers which are usually at lower elevations than the average of the local terrain (at the foot of mountains, in river valleys). The model terrain is averaged over an area large enough that the nearest model point to a station location is almost always higher than the station, and is normally cooler as a result. In addition, the lateral diffusion of temperature (to maintain numerical stability) results in some systematic temperature errors in complex terrain. Figure 8-8 shows the average dew point errors. The model clearly has a moist bias, which is probably due to a systematic overestimation of evapotranspiration in the model's surface energy budget, especially in the winter simulations. More work is needed to make the evapotranspiration scheme more accurate. The dry bias on the New Mexico grid probably is caused by a too-dry soil moisture assumption on the grid (0.1 compared to 0.2 for the other grids). Figure 8-9 shows the wind speed characteristics. The low errors on the Great Plains grid is probably due to the fact that the surface is quite uniform for that grid, with very little coastline and no terrain to produce complicated local wind circulations.

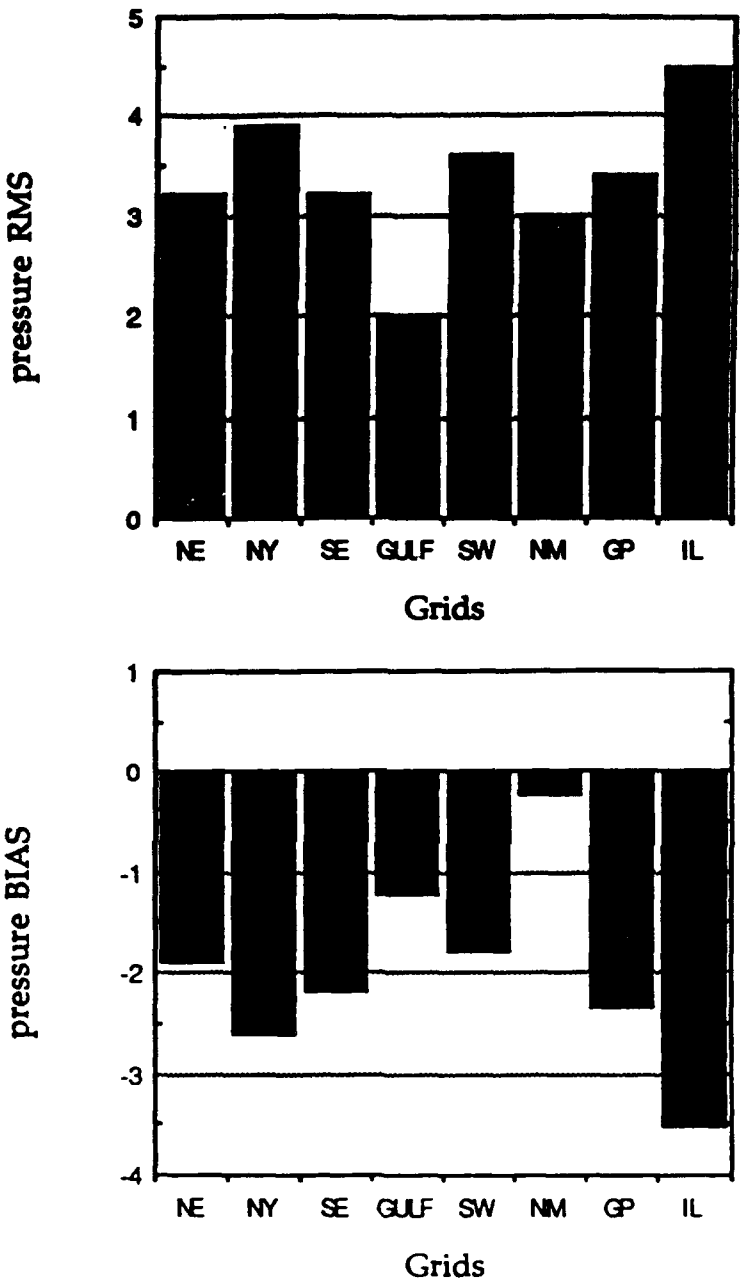

Figure 8-6 RMS and BIAS errors for pressure (mb) averaged over all of the simulation dates.

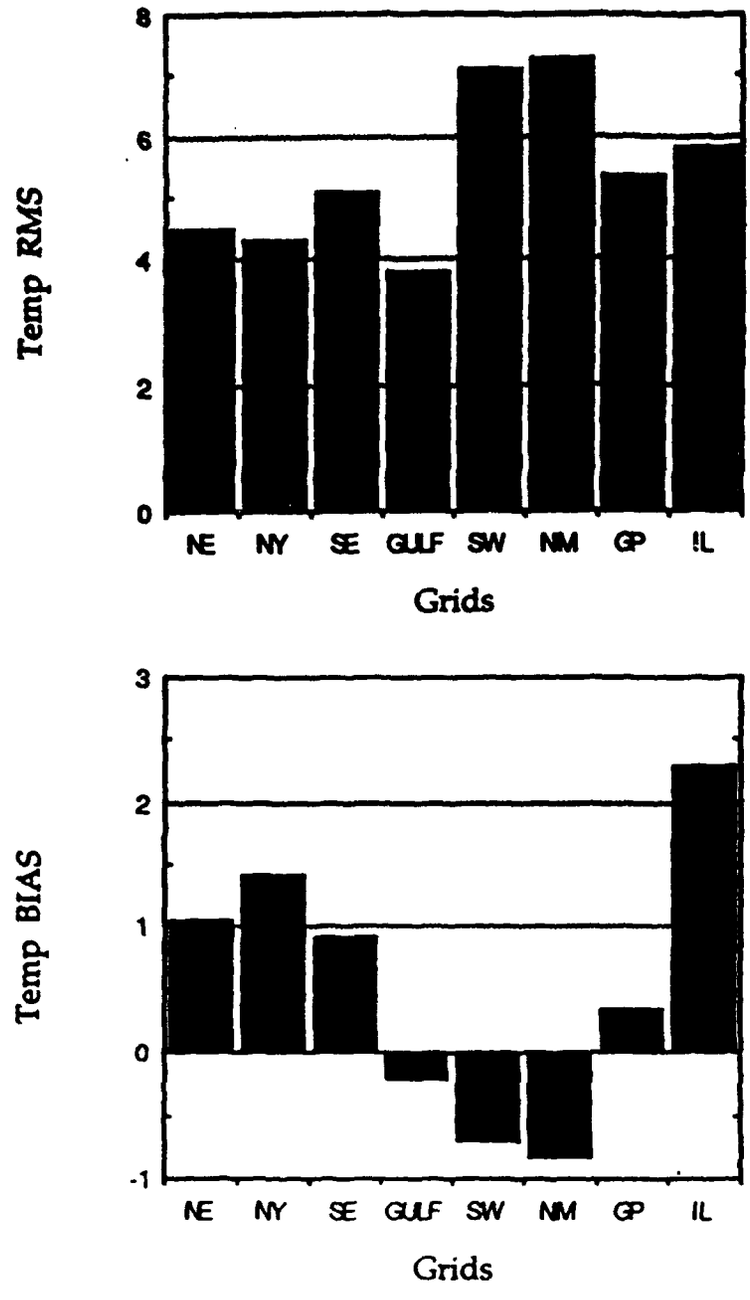

Figure 8-7 RMS and BIAS errors for temperature (F) averaged over all of the simulation dates.

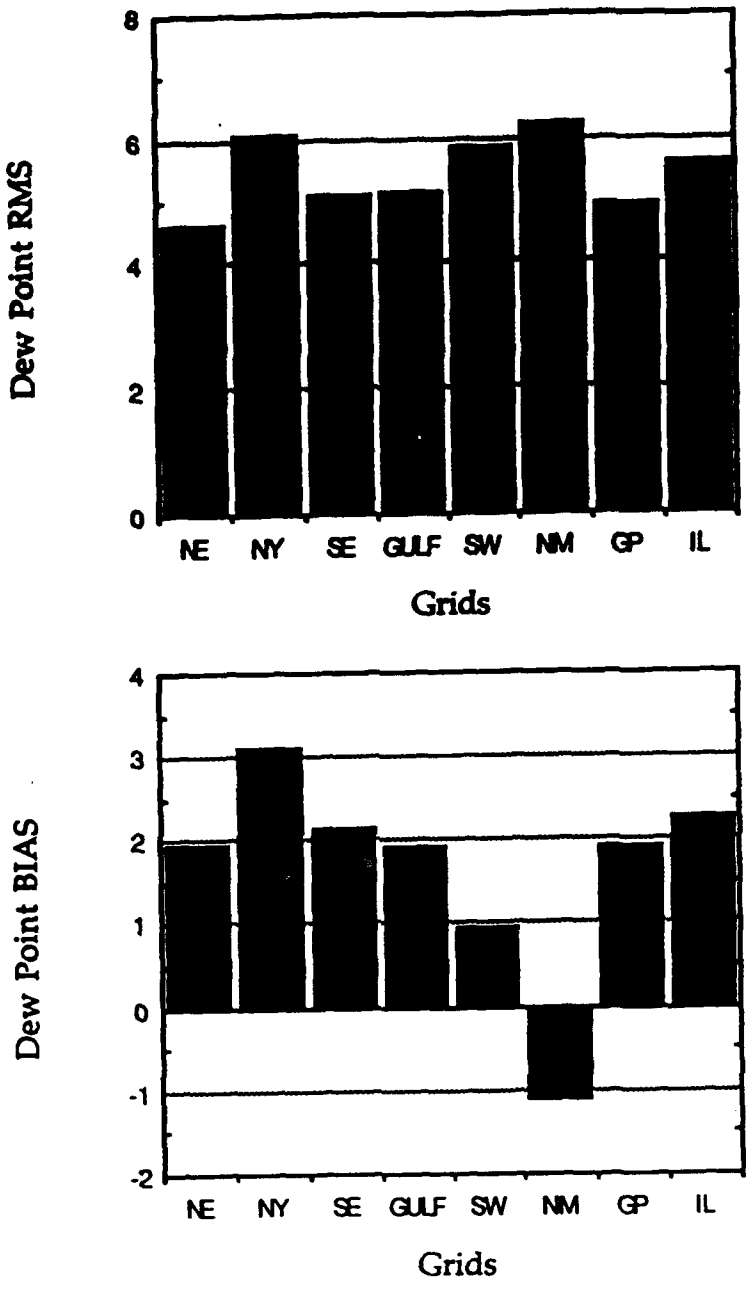

***Figure 8-8** RMS and BIAS errors for dew point (°F) averaged over all of the simulation dates.*

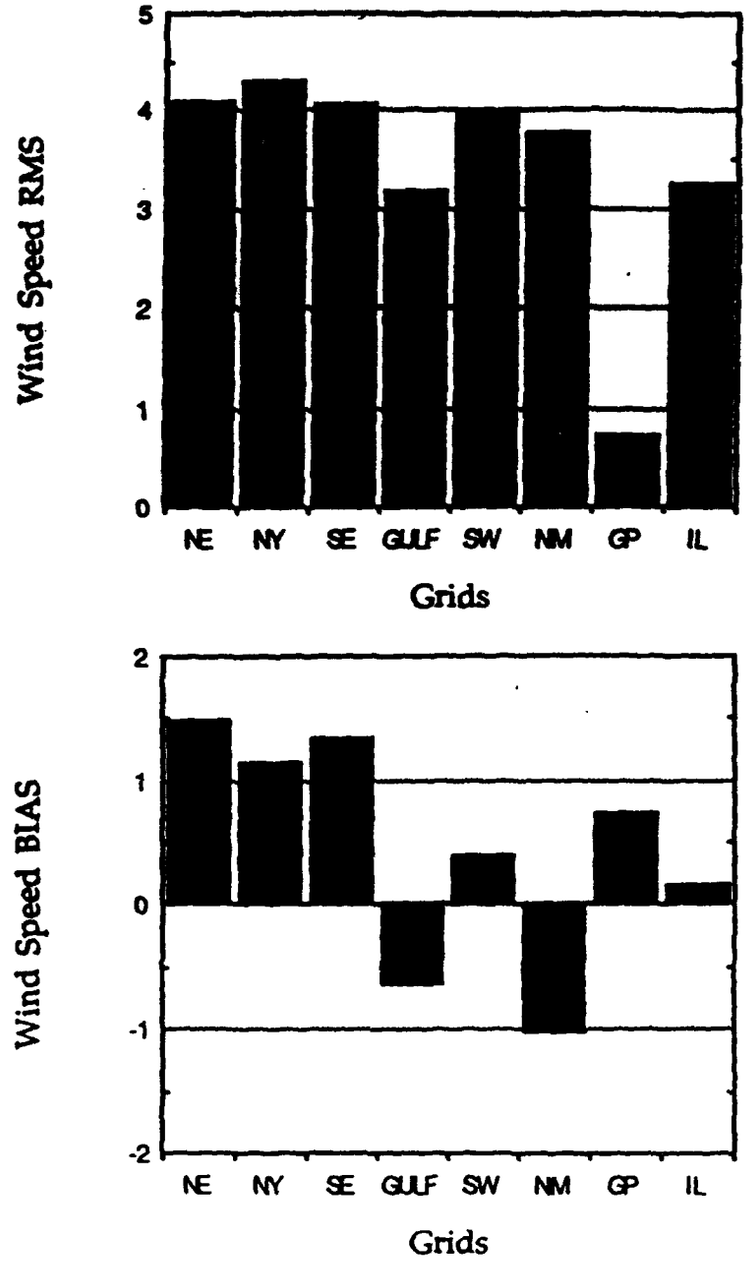

***Figure 8-9** RMS and BIAS errors for wind speed (kts) averaged over all of the simulation dates.*

Figure 8-10 shows the 0.01 inch THREAT scores for each of the large scale grids (many of the nested grids had completely dry simulations, which made it difficult to compute meaningful precipitation statistics). The THREAT scores are good in general, although there are wide variations between simulations, and at various times in the simulations. Precipitation remains the most difficult meteorological variable to predict. There were both very good and very poor precipitation forecasts in the 36-case sample. The Northeast snowstorm was mostly well-predicted, but the mesoscale convective complex (MCC) over Iowa in the September series of runs was poorly handles, even when the nested grid was shifted to be centered over the storm. The main reason was that the forcing for the MCC was not well-resolved by conventional observations, even when supplemented by surface and radar nudging, while the synoptic scale forcing responsible for the Northeast storm was well-captured by the initial and boundary conditions.

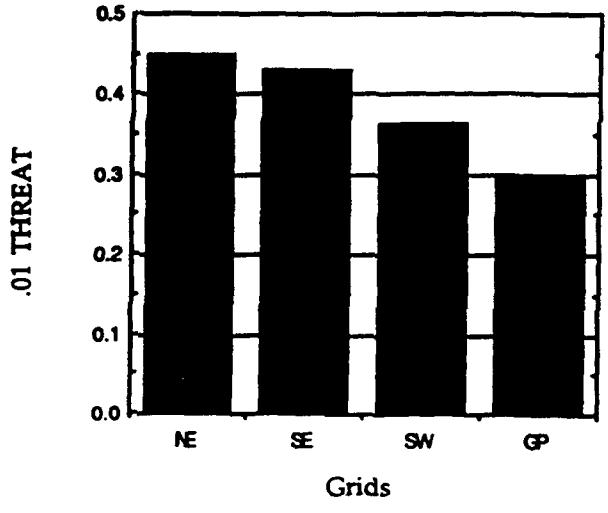

Figure 8-10 Precipitation THREAT scores (.01 inch) for each of the large scale grids, averaged over all the simulation dates.

Second, the statistical data was divided by time in the simulation, to see the evolution of errors in a set of similar simulations. The August 24 case was selected for analysis, as a summertime example with a relatively complete dataset. Figure 8-11 shows the development with time of the temperature RMS and BIAS errors for the large scale grids on August 24. The temperature errors grow with time, and the BIAS has an interesting evolution. The temperatures are systematically warm in the early morning hours, peaking at about the expected time of the morning temperature minimums, while the model is too cool by several degrees in the afternoon. At least a part of the reason for this is the fact that the model's first layer is higher than the level where standard observations are taken (about 7 or 8 m vs. 2 m for observations). This means that level 1 in the model does not see the more extreme values observed during strong radiative heating or cooling. The excess of evaporation during the afternoon may also be a part of the explanation.

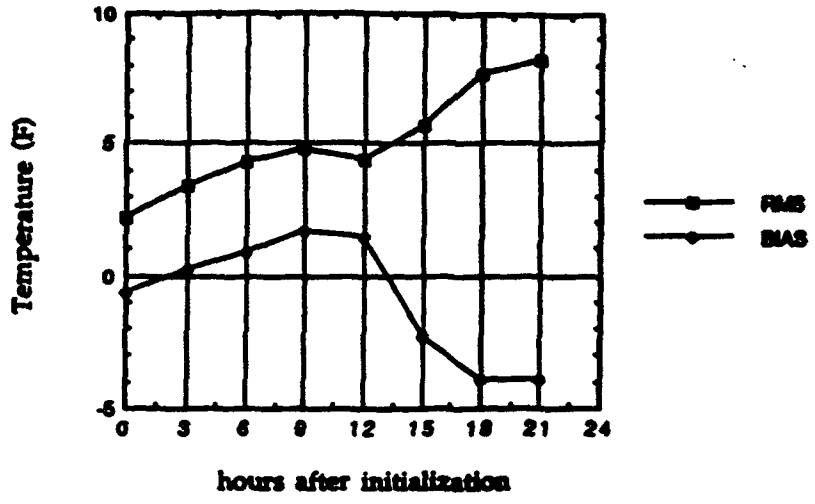

Figure 8-11 Temperature RMS and BIAS errors for large scale simulations on August 24, 1992.

Figure 8-12 shows the dew point errors, and Figure 8-13 shows wind speed errors. The wind speed biases show that there is a pronounced tendency in the model for winds which are too strong at night and slightly too weak during the afternoon. The above discussion of temperature errors is also relevant to the wind speed. The first layer needs to become more decoupled from the rest of the atmosphere at night, so that radiative cooling can drive the temperature minimum a few degrees lower.

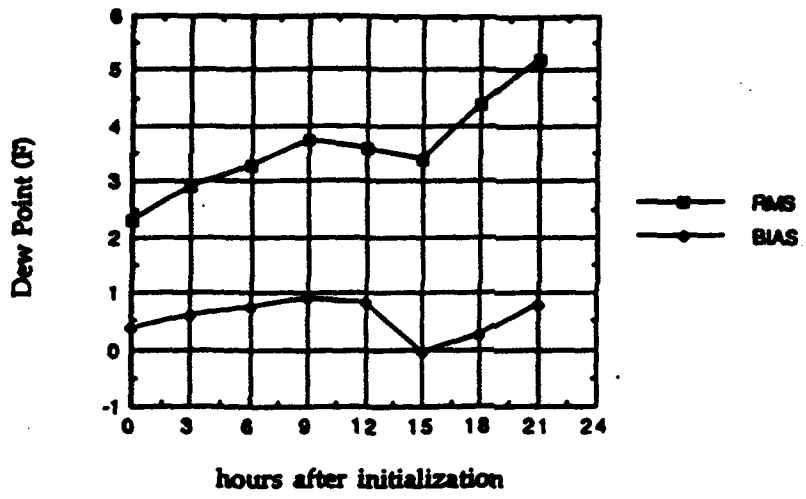

Figure 8-12 Dew point RMS and BIAS errors for large scale simulations on August 24, 1992.

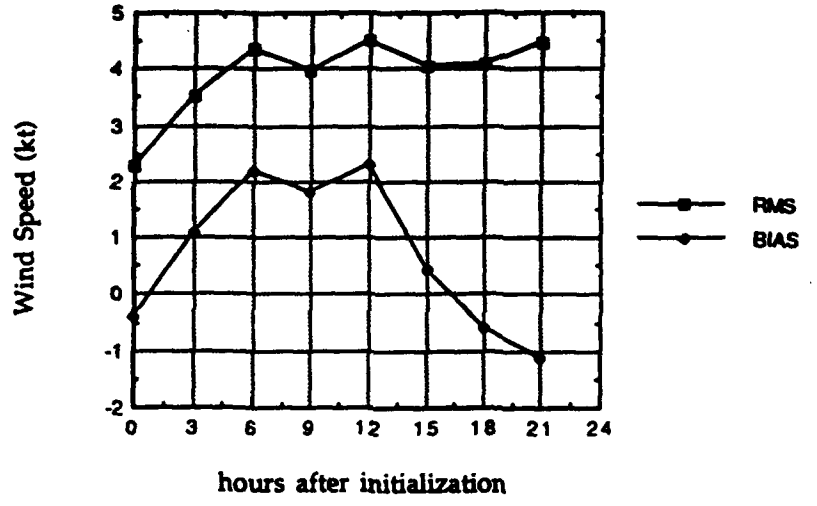

Figure 8-13 Wind speed RMS and BIAS errors for large scale simulations on August 24, 1992.

A close examination of the December 11 winter case revealed some interesting features. The evolution of temperature errors (Figure 8-14) is quite different than in the summer case (Figure 8-11). The temperature errors are smaller in general, because the situation is more controlled by large scale processes such as advection, than by local boundary layer processes.

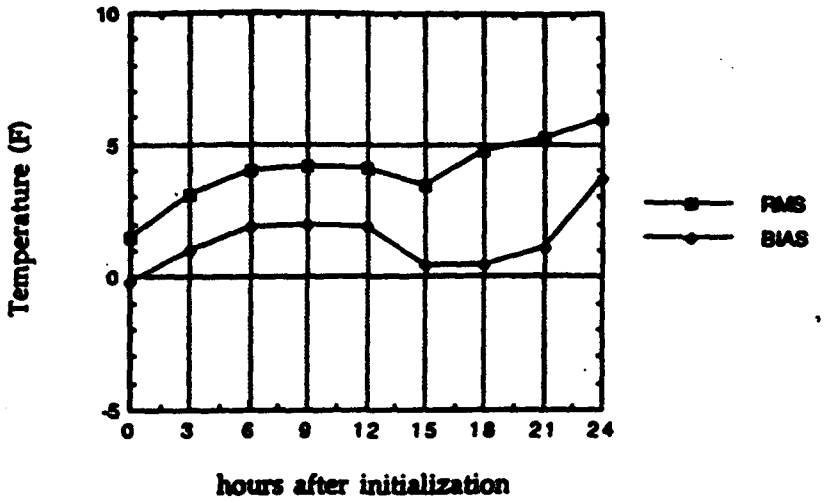

Figure 8-14 Temperature RMS and BIAS errors for the two northern large scale simulations (Northeast and Great Plains) on December 11, 1992.

Figure 8-15 shows the dew point errors for the same December 11 case. The overestimation of evaporation is especially troublesome in the winter, when very little evaporation should be taking place.

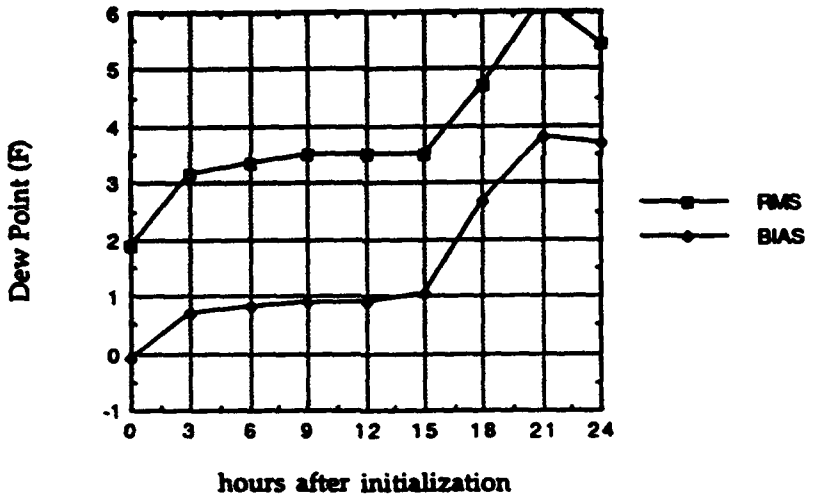

Figure 8-15 Dew point RMS and BIAS errors for the two northern large scale simulations (Northeast and Great Plains) on December 11, 1992.

8.3 Simulation Examples

8.3.1 December 11 Northeast Case: The *First* "Storm of the Century"

A major storm which was called by some the "Storm of the Century" hit the northeastern U.S. over the period from December 10 to December 12, 1992. This storm was later

overshadowed by an even stronger storm which battered the entire East Coast in March, 1993; this storm was also dubbed the Storm of the Century, with somewhat more justification.

In the December storm, a strong surface low pressure center just off the East Coast associated with a vigorous upper level baroclinic wave produced heavy rainfall and coastal flooding in New Jersey and New York City, and heavy snowfall inland, especially in Pennsylvania, New York State and Massachusetts. In addition to the cases for this same period which were a part of the 36-case sample, a special set of MASS simulations was performed in order to focus the nested simulation on a different twelve hour period. A 40 km simulation began at 1200 UTC 10 December and ran for 36 hr. A nested 15 km simulation used lateral boundary conditions from the 40 km run. It began at 0000 UTC 11 December and ran for 15 hr. These simulations were interesting because of both the size and strength of the storm, and because of some mesoscale features of the storm.

Figure 8-16 shows the modeled evolution of the surface pressure field during the 40 km simulation. Multiple areas of low pressure which were initially large and diffuse merged into one much deeper (991 mb) low off the coast of Virginia by about 0900 UTC 11 December. The actual position of the low was a little further north. The evolution of model-produced precipitation is shown in Figure 8-17. The heavy precipitation to the north of the low pressure center was observed, although the precipitation pattern is also shifted somewhat to the south of were it was observed. Central and northwestern Pennsylvania received heavy snowfall through the middle part of the simulation. Pittsburgh, Johnstown, Erie, Bradford, Altoona, and State College all received very heavy snowfall during this period. The precipitation maximum north of Lake Ontario was also verified; the area around Toronto, ON experienced heavy snowfall.

Precipitation distributions from the 15 km simulation are shown in Figure 8-18. The precipitation pattern is strongly related to the local terrain, with a strong maximum developing over the Catskill Mountains in New York and extending southwestward into elevated areas in northeastern Pennsylvania. A distinct minimum occurs along the Hudson River valley, which was observed to occur as a result of downsloping flow down the lee side of the Berkshire Mountains in western Massachusetts. Figure 8-19 demonstrates that the downslope flow was well simulated by the MASS model. The vertical velocity field ($\omega = dp/dt$) in Figure 8-19b clearly shows that the easterly winds have induced strong upward motion (negative ω) on the windward sides of the Berkshires and the Catskills and subsidence (positive ω) on the lee sides. This interpretation is supported by rain and snowfall data from hydrological observations, which are plotted in Figure 8-20. The lack of snow in the Hudson Valley contrasts with the observation of 15 inches of new snow in the Catskills. Table 8-2 lists 12 hr precipitation amounts for selected standard surface stations. The 15 km simulation properly simulated the heavy precipitation in the New York City area, and the lack of precipitation in Albany and Glens Falls. Neither simulation produced rainfall as heavy as the greater than two inch amounts reported in New Jersey and eastern Pennsylvania.

***Table 8-2** Observed and simulated precipitation (inches) for selected cities from 0000 UTC to 1200 UTC 11 December 1992*

Location	Observed	MASS 40 km	MASS 15 km
Windsor Locks, CT (BDL)	.07	.14	.14
Bridgeport, CT (BDR)	.42	.13	.57
Albany, NY (ALB)	.03	.06	.02
Poughkeepsie, NY (POU)	.23	.20	.30
Glens Falls, NY (GFL)	.01	.05	.16
Binghampton, NY (BGM)	.07	.13	.19
LaGuardia Arpt., NY (LGA)	.83	.23	.75
John F. Kennedy Arpt., NY (JFK)	.86	.27	.68
Allentown, PA (ABE)	.38	.65	1.26
Scranton-Wilkes-Barre, PA (AVP)	.23	.50	.80

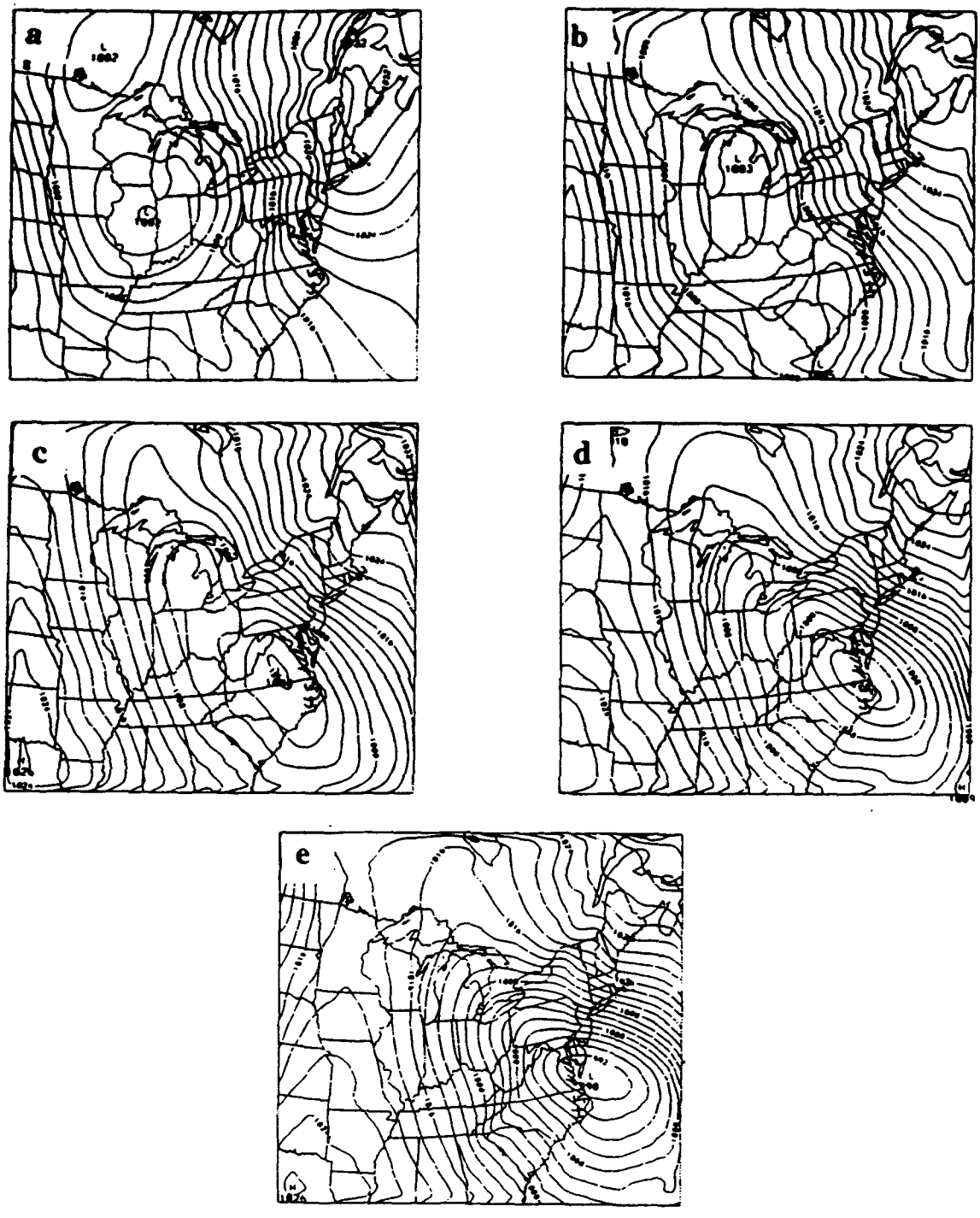

Figure 8-16 *Mean sea level pressure (mb) from MASS 40 km simulation at (a) 1200 UTC and (b) 1800 UTC 10 December, (c) 0000 UTC, (d) 0600 UTC, and (e) 1200 UTC 11 December.*

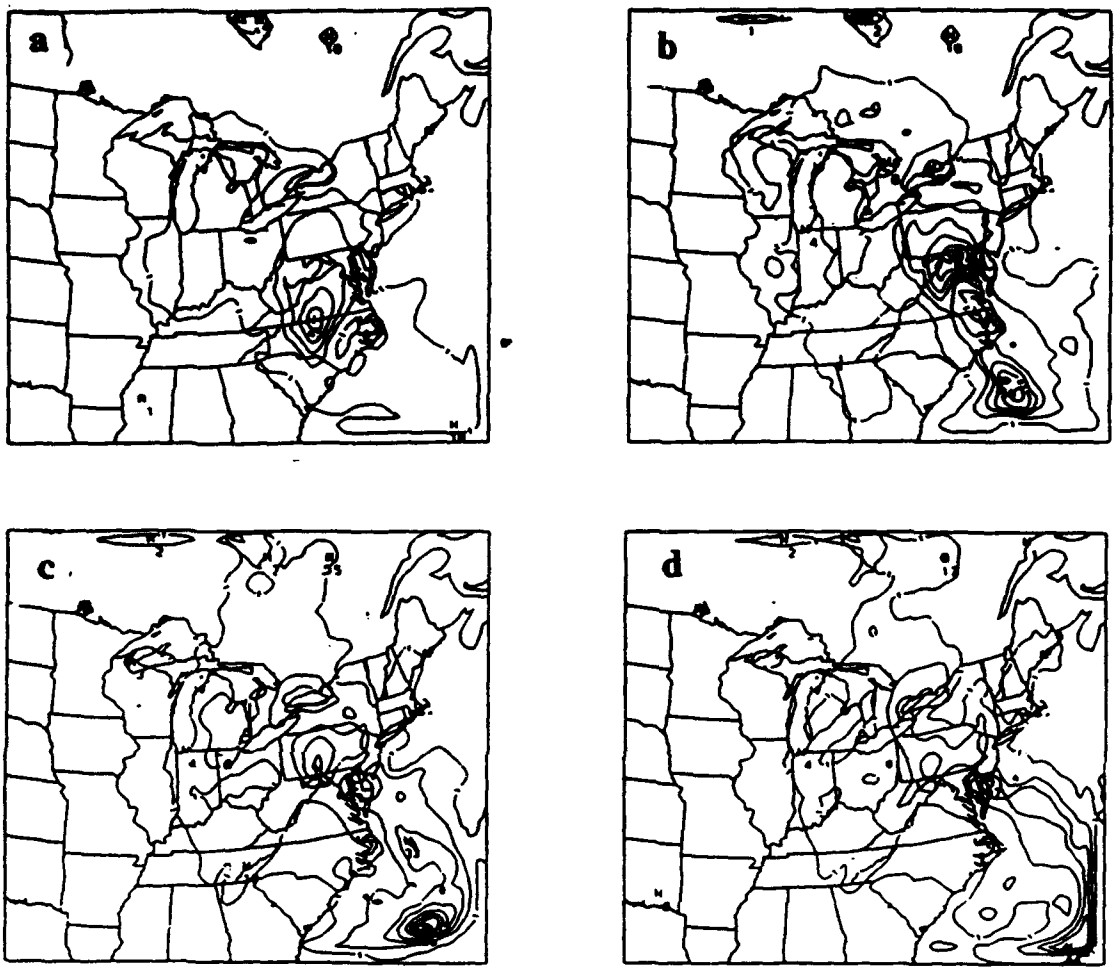

Figure 8-17 Precipitation (inches of liquid water) from the 40 km MASS simulation for 3 hr periods ending at (a) 1800 UTC 10 December, (b) 0000 UTC, (c) 0600 UTC, and (d) 1200 UTC 11 December.

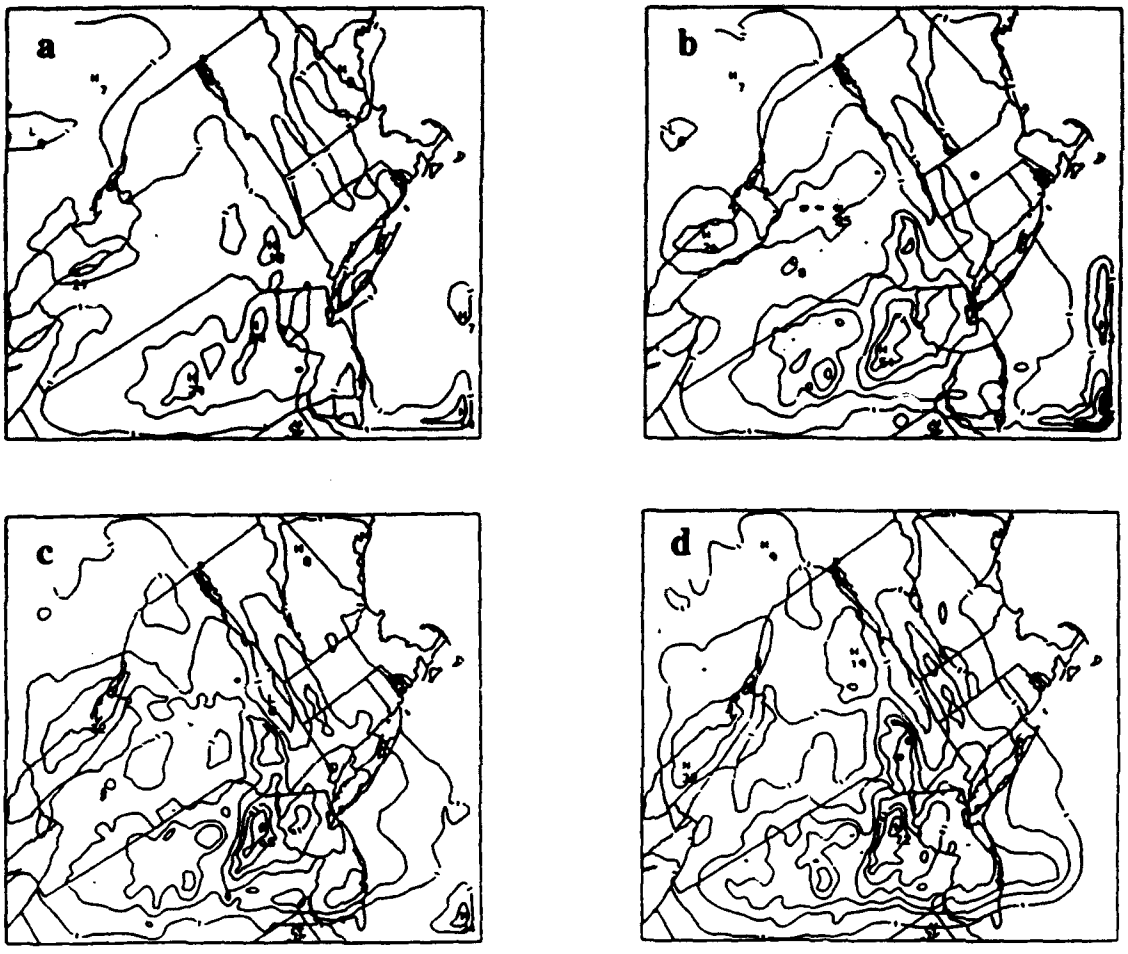

Figure 8-18 *Precipitation (inches of liquid water) from the 15 km MASS simulation for 3 hr periods ending at (a) 0300 UTC, (b) 0600 UTC, (c) 0900 UTC, and (d) 1200 UTC 11 December.*

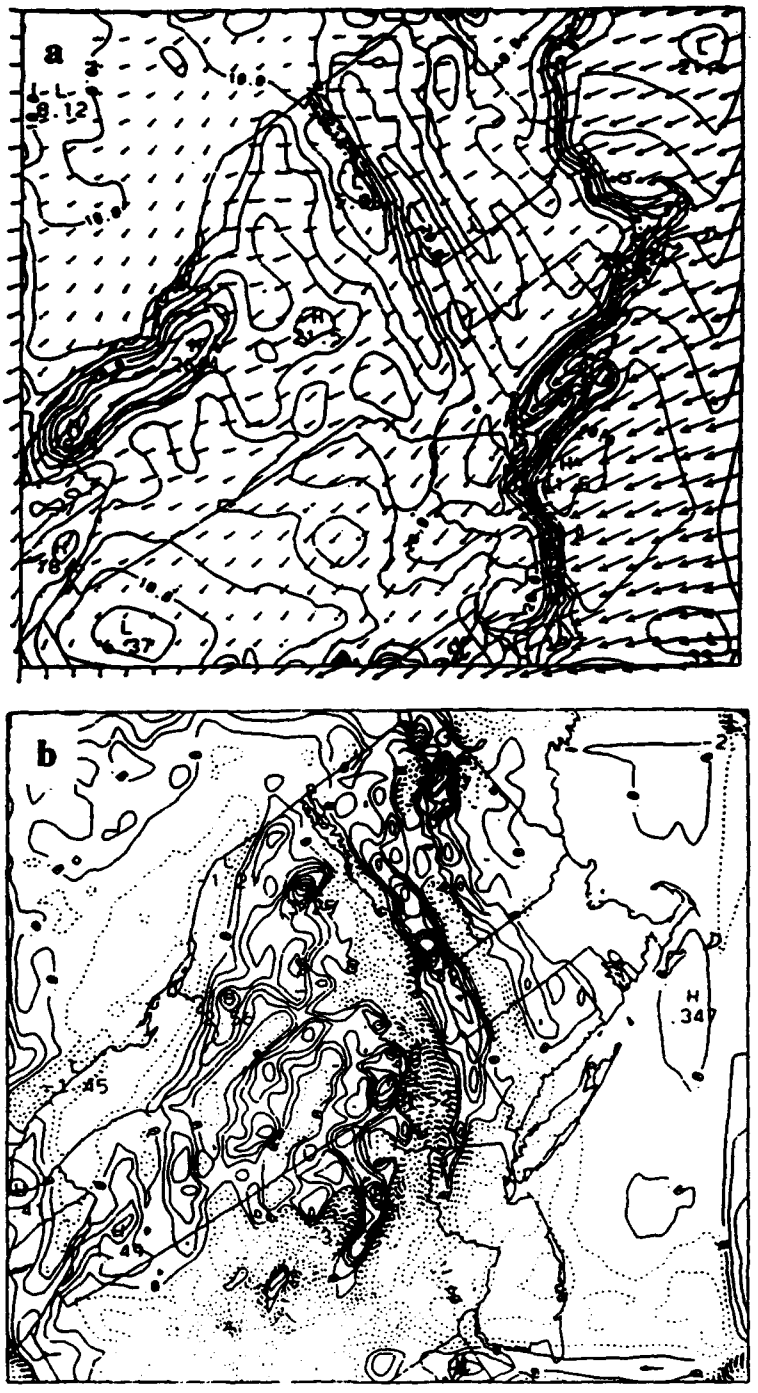

Figure 8-19 *(a) Winds in the lowest model layer (contoured in knots) and (b) vertical velocity ($\omega = dp/dt$) from the MASS 15 km simulation at 1200 UTC 11 December 1992. The vertical velocity contours are in Pa s^{-1}; the solid contours are positive ω (downward motion), the dashed contours represent negative ω (upward motion).*

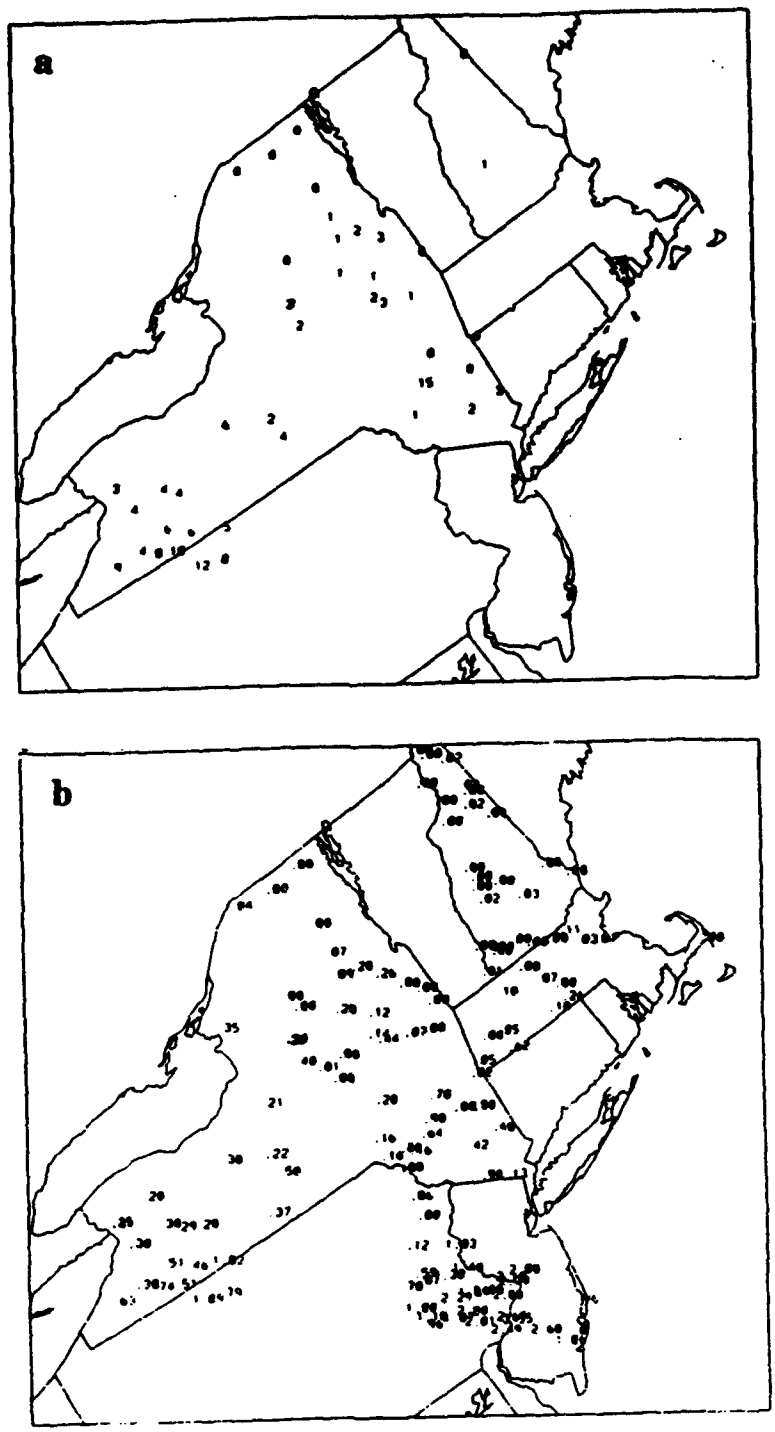

***Figure 8-20** 24 hr totals of: (a) snowfall (inches), and (b) precipitation (inches) from hydrological reports on the morning of 11 December.*

8.3.2 September 14 Southeast Case: Subtle Mesoscale Features

The day of September 14, 1992 was a fairly tranquil day in the Southeast, with an upper level ridge of high pressure dominating the synoptic situation. The set of MASS simulations which were carried out on this day contained some subtle features which were quite well-simulated.

Figure 8-21 shows model fields halfway through the nested MASS simulation at 1800 UTC 14 September. Three mesoscale features are interesting:

(1) The moderate northeasterly winds in the western half of the domain are advecting somewhat drier air into the domain, as can be seen from Figure 8-21c. Figures 8-22 and 8-23 show the model evolution (large scale and nest) of low level temperature, dew point, and winds for Greenwood, MS (GWO) and Montgomery, AL (MGM). The diurnal temperature evolutions are similar at the two stations, but the dew point at MGM drops throughout the day from the dry advection, while the dew point at GWO rises for most of the day.

(2) Both simulations have a spurious drop in dew point in the afternoon, a characteristic problem of the PBL scheme. What seems to happen is that strong mixing through a significant depth of the lower atmosphere occurs suddenly when the PBL has destabilized enough to enter the free convection regime. When air which is relatively dry overlays the surface, it is mixed down to the surface too rapidly. This is a consequence of the plume model of the unstable PBL, which allows sinking and mixing of air at the top of the PBL to the surface immediately. One possible solution is to make a modification to the scheme, which would allow surface parcels to ascend and mix to the top of the PBL immediately (rising plumes), while constraining downward mixing to a lesser rate, on the assumption that negatively buoyant parcels do not traverse through the entire depth of the PBL in the same way that rising parcels do.

(3) The stronger easterly winds in the Gulf of Mexico are coming onshore in Louisiana, leading to some weak convergence and light rainshowers through the afternoon. Observations suggest that this did occur, with towering cumulus and occasional showers observed at stations in and near New Orleans.

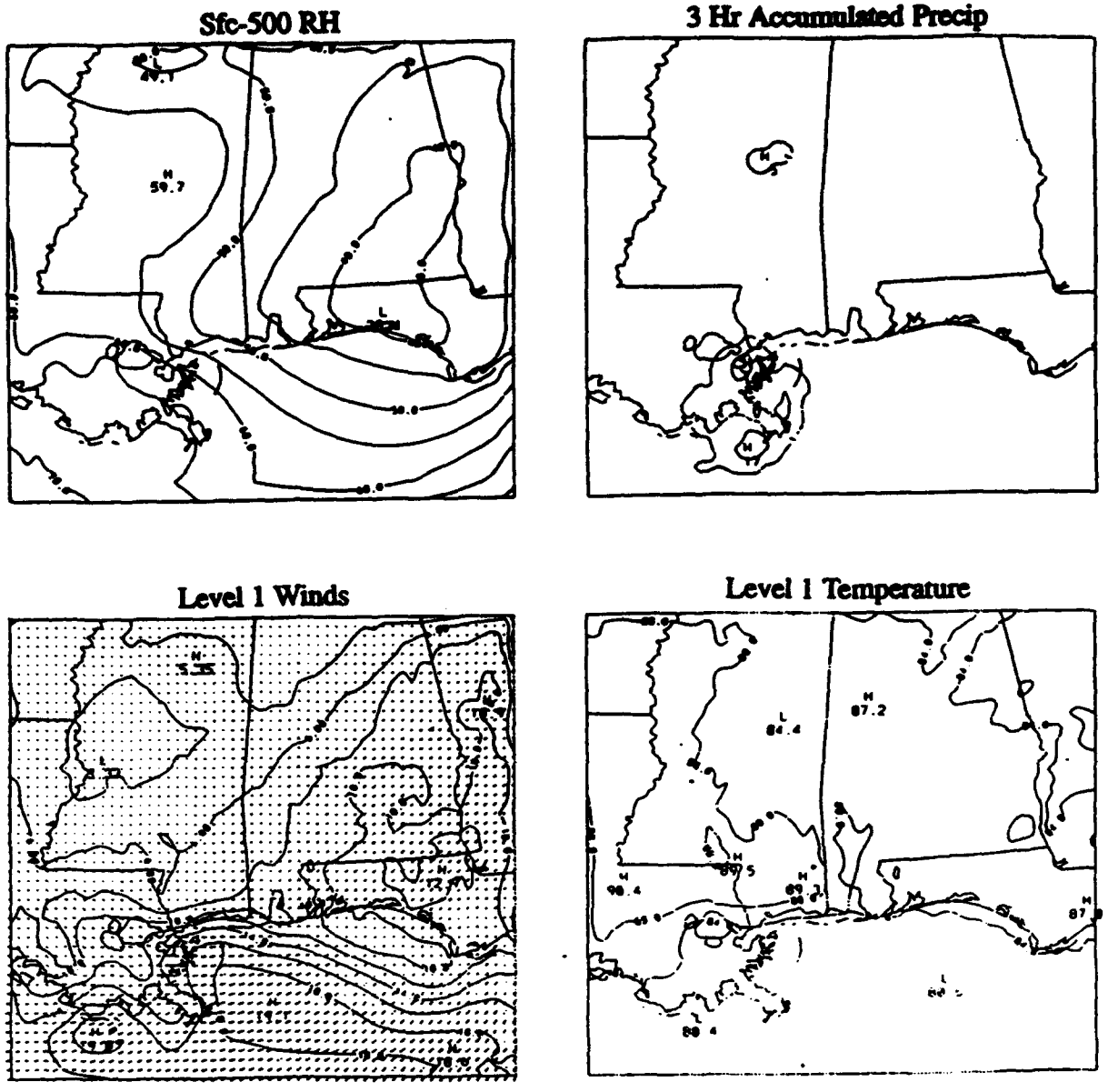

***Figure 8-21** MASS model fields at 1800 UTC 14 September: (a) Temperature (°F) and (b) winds in the lowest model layer, (c) the average relative humidity in the layer from the surface to 500 mb (%), and (d) model precipitation (hundredths of an inch) accumulated in the previous three hours .*

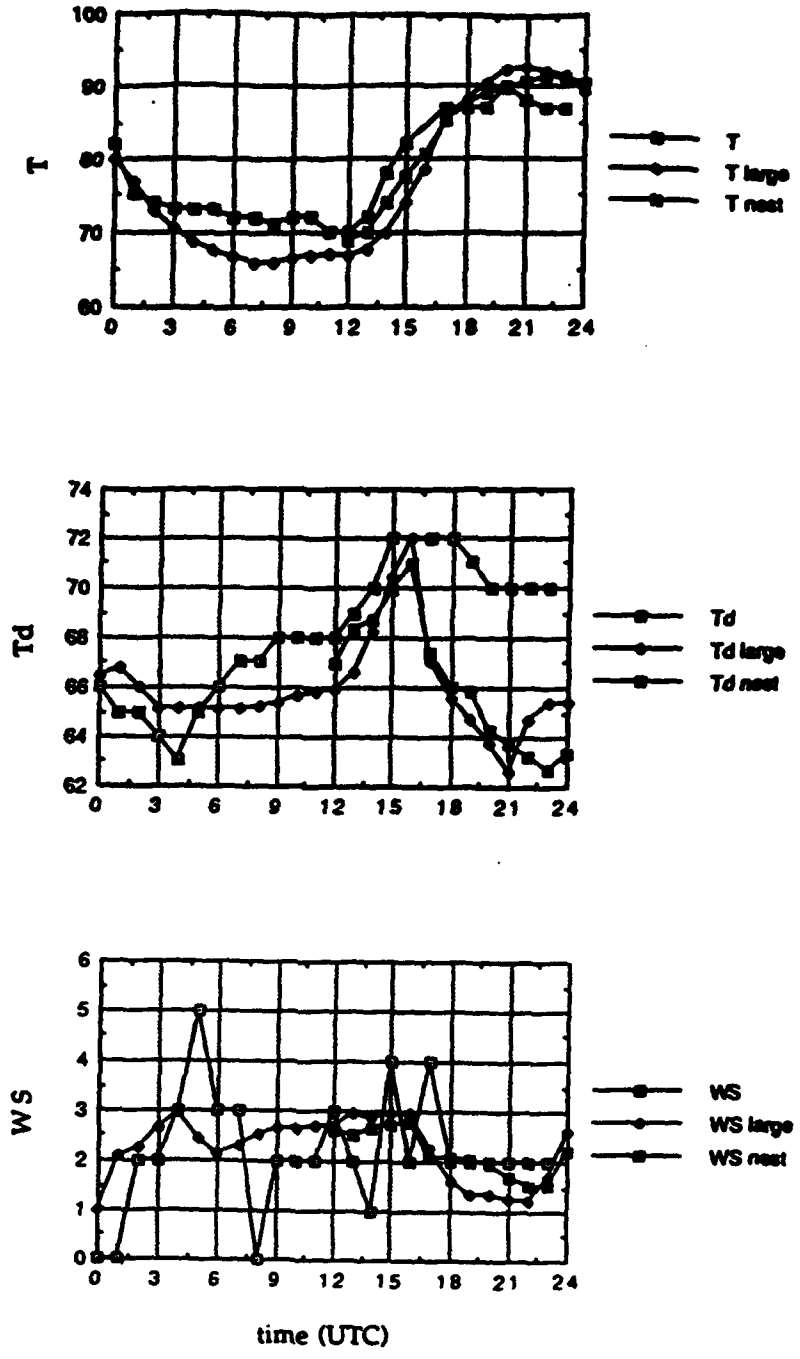

Figure 8-22 *The diurnal evolution of: (a) temperature (°F), (b) dew point (°F), and (c) wind speed (m s^{-1}) during 14 September 1992. at Greenwood, MS. The first curves (open boxes) represent the observed fields, and the other two lines are taken from model grid points nearest to the station location for the large scale (50 km) and nested (15 km) simulations for that day.*

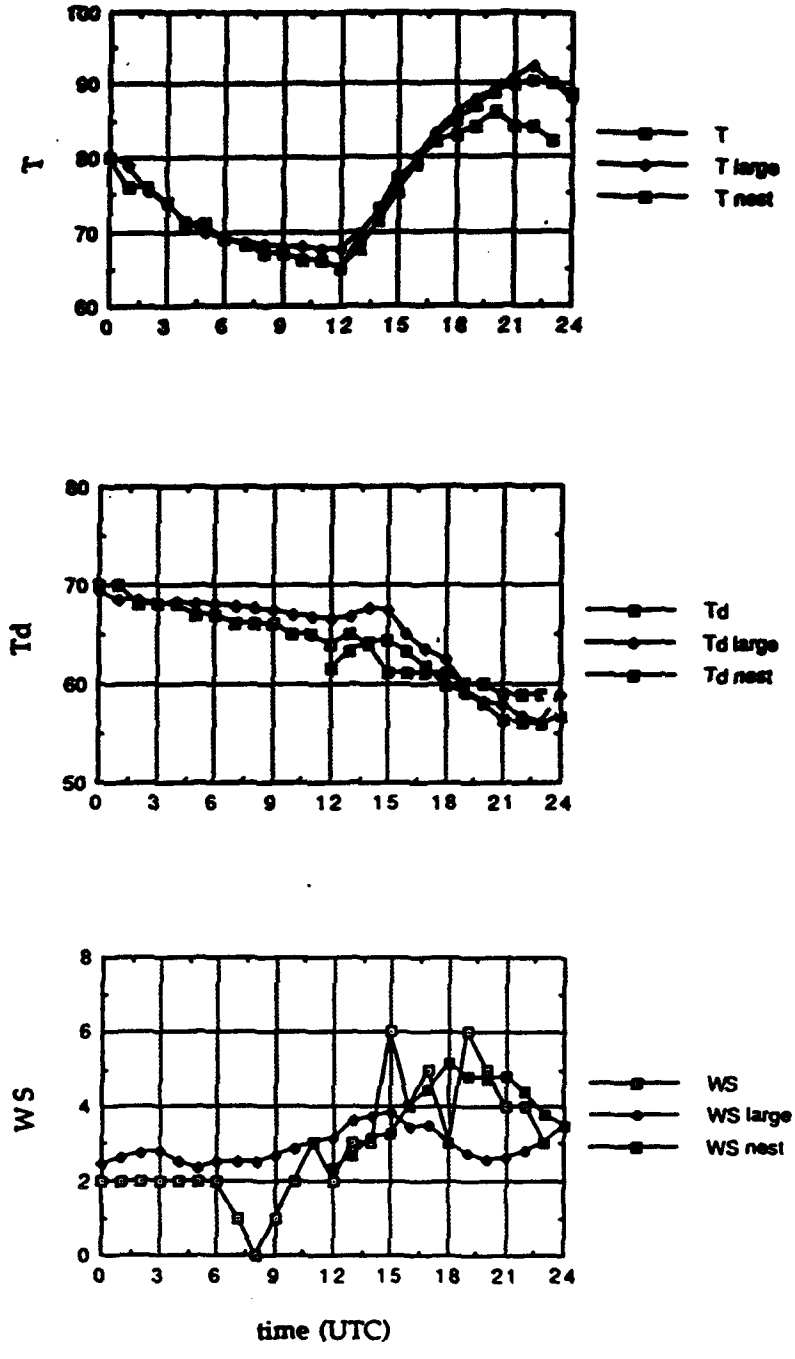

Figure 8-23 The diurnal evolution of: (a) temperature (°F), (b) dew point (°F), and (c) wind speed (m s^{-1}) during 14 September 1992. at Montgomery, AL. The first curves (open boxes) represent the observed fields, and the other two lines are taken from model grid points nearest to the station location for the large scale (50 km) and nested (15 km) simulations for that day.

8.3.3 August 22 Southwest Case: Strong Terrain Influences

On the meso-α scale, terrain tends to be fairly poorly resolved, and only large terrain features which are well-resolved by the model grid have a significant influence on simulations. At the lower limit of hydrostatic mesoscale simulations (10-15 km), smaller terrain features and stronger slopes are resolved, which have a great effect on many nested simulations. For the first set of dates (August 22-24), the nested New Mexico simulations used a 10 km resolution, rather than the 15 km resolution of the later simulations. The strong effects of relatively fine-scale mountain ranges are readily seen. Figure 8-24 shows the terrain heights for this grid. Figures 8-25 through 8-27 show a six hour period in the middle of the nested 10 km simulation for 22 August 1992. The moisture from Hurricane Lester was beginning to move in from the west, and precipitation develops during the day. The precipitation forms over the various terrain features of the area preferentially, first over the high terrain in the western part of the grid and then over the Sacramento Mountains toward the east. Temperature perturbations (low temperatures over the mountains) may be exaggerated by the difficulty of formulating a lateral diffusion scheme for sigma layers over strongly sloping terrain. Vertical (physical) mixing processes typically become entangled with the horizontal diffusion, which is for purely numerical purposes. The horizontal diffusion is designed to prevent the accumulation of energy into short length scales, and subsequent aliasing to longer lengths. The proper treatment of diffusion of moisture along sloping surfaces is also poorly understood.

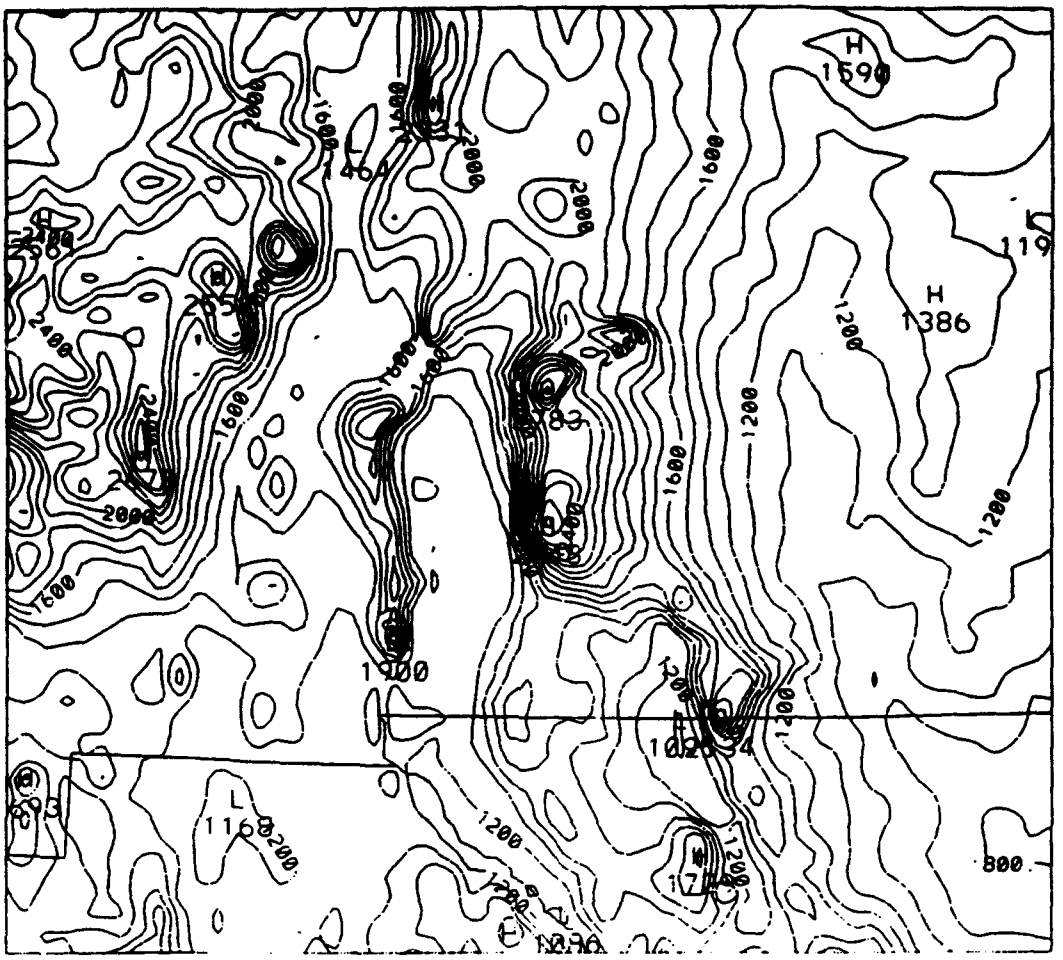

Figure 8-24 Terrain heights (m) for the 10 km New Mexico nested domain.

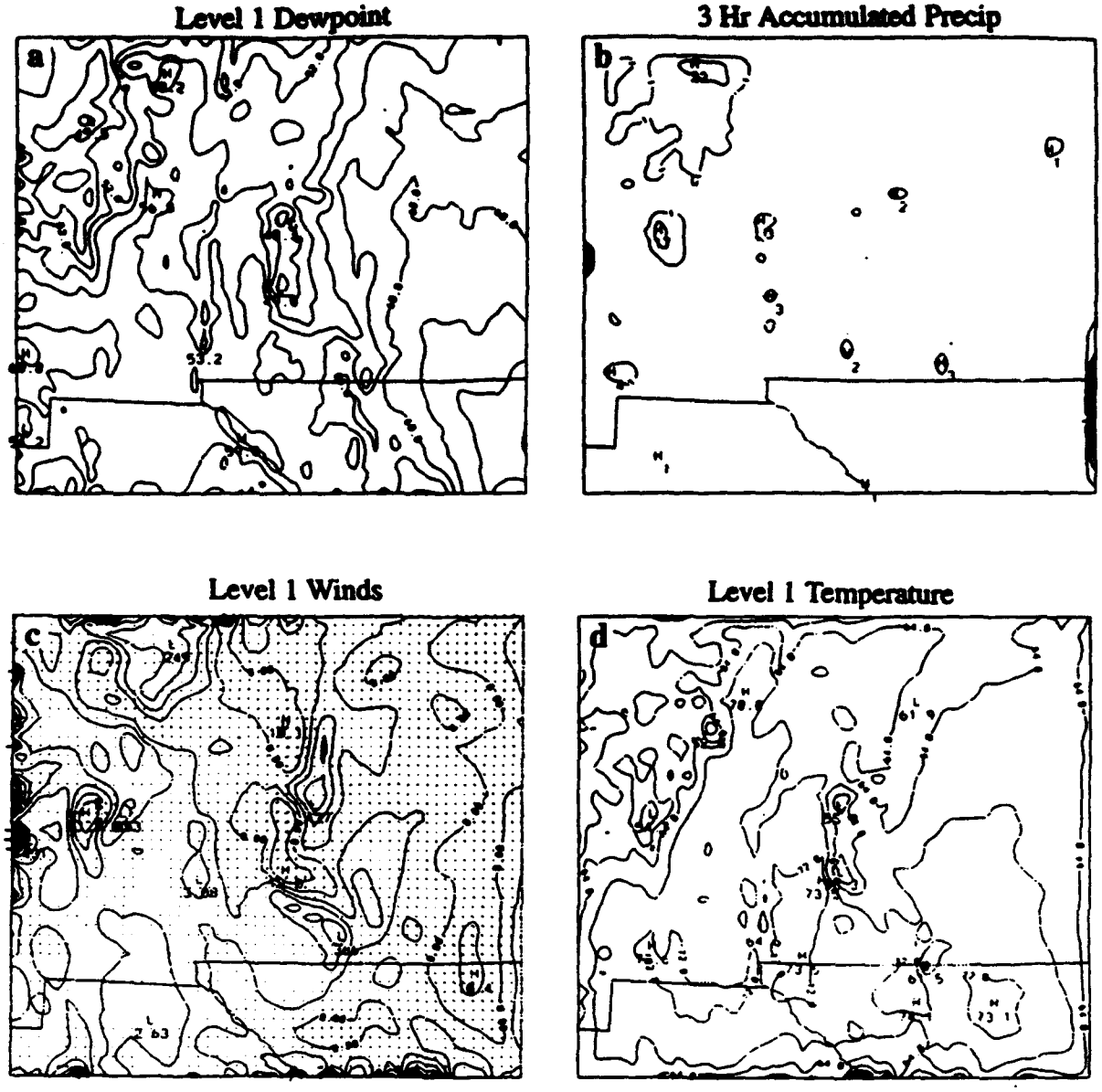

Figure 8-25 Nested model fields for 1500 UTC 22 August 1992: (a) low level dew point (°F), (b) 3 hr accumulated precipitation (hundredths of an inch), (c) low level winds (knots), and (d) low level temperature (°F).

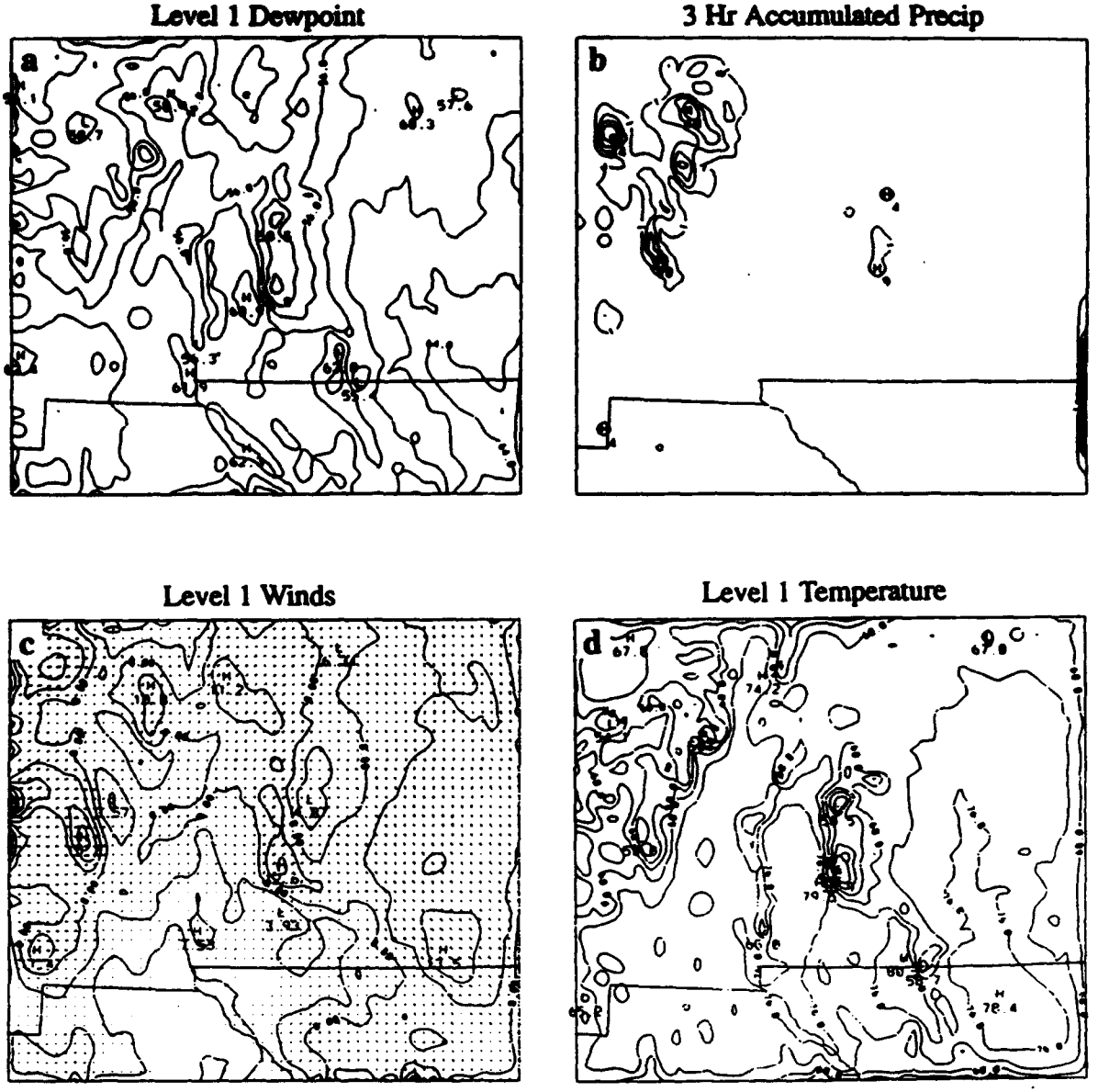

Figure 8-26 Nested model fields for 1800 UTC 22 August 1992: (a) low level dew point (°F), (b) 3 hr accumulated precipitation (hundredths of an inch), (c) low level winds (knots), and (d) low level temperature (°F).

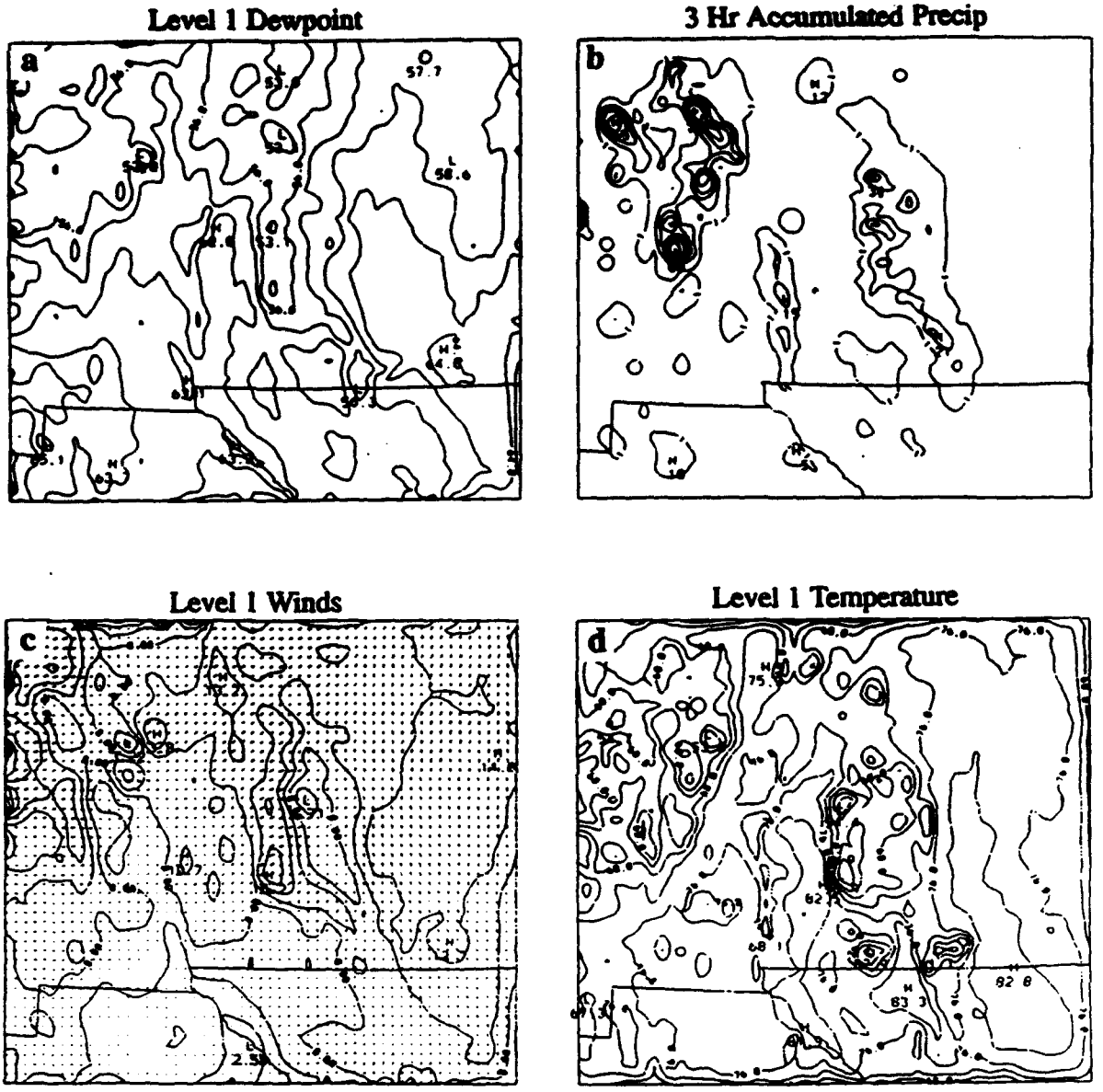

Figure 8-27 Nested model fields for 2100 UTC 22 August 1992: (a) low level dew point (°F), (b) 3 hr accumulated precipitation (hundredths of an inch), (c) low level winds (knots), and (d) low level temperature (°F).

8.3.4 December 10 Great Plains Case: Receding Cloud Boundary

The explicit and implicit treatment of clouds in mesoscale models remains one of the most difficult scientific and practical problems. In some simulations, poor simulation of cloudiness leads to poor results, as temperatures are affected and inland heating gradients due to the delineation of cloudy and cloud-free air either develop when they shouldn't or fail to develop when they should.

Figure 8-28 shows the observed and model evolution of surface variables at Columbia, MO (COU) on 10 December 1992. In this case, a cloudy area associated with the large scale system which produced the Northeastern snowstorm (Section 8.3.1) was receding to the east. The fairly complex and subtle variations during the day were well-simulated by both the large scale and nested simulations, although the temperatures were systematically several degrees too warm. Figure 8-29 shows the modeled clouds (as indicated by the shortwave transmissivity field, where low transmissivity indicates thick clouds) moving toward the northeast in the nested 15 km Illinois grid. Table 8-3 lists the Columbia observations through the day.

Table 8-3 Hourly observations at Columbia, MO for 10 December 1992.

time (UTC)	temperature / dew point (°F)	wind speed/wind direction (deg/kts)	clouds/sky conditions
0000	32/32	130/3	overcast/snow
0100	32/32	140/3	overcast/snow
0200	32/32	160/3	overcast/fog
0300	32/32	180/3	overcast/fog
0400	32/32	200/4	overcast/fog
0500	32/32	210/3	obscured/fog
0600	33/33	200/3	obscured/fog
0700	33/33	220/5	obscured/fog
0800	34/34	180/3	obscured/fog
0900	35/35	210/4	obscured/fog
1000	–	250/3	–
1100	37/36	260/7	overcast
1200	–	230/3	clear
1300	36/33	300/9	overcast
1400	35/33	310/6	overcast/fog
1500	35/33	300/6	overcast/drizzle
1600	35/33	300/7	overcast/drizzle
1700	36/33	310/7	overcast/fog
1800	38/34	300/8	overcast
1900	40/36	310/7	broken
2000	43/35	320/7	scattered
2100	45/34	290/7	clear
2200	44/32	280/7	clear
2300	42/31	300/6	clear

The inferred sequence of events at Columbia is as follows:

(1) Conditions slowly improve in the morning under southerly or southwesterly flow. The temperature and dew points rise.

(2) A weak frontal passage occurs at about 1300 UTC, with a wind shift to the northwest, and some drizzle along the frontal boundary. The wind speed jumps up significantly. The temperature and dew points drop in the new air mass between 1200 and 1500 UTC.

(3) As skies begin to clear out behind the front from 1500 to 2100 UTC, temperatures increase again, and the dew points increase also, possibly from some evaporation of the abundant surface moisture, driven by sunshine and warming.

(4) Drier air advects in behind the front, dropping the dew points after 2000 UTC.

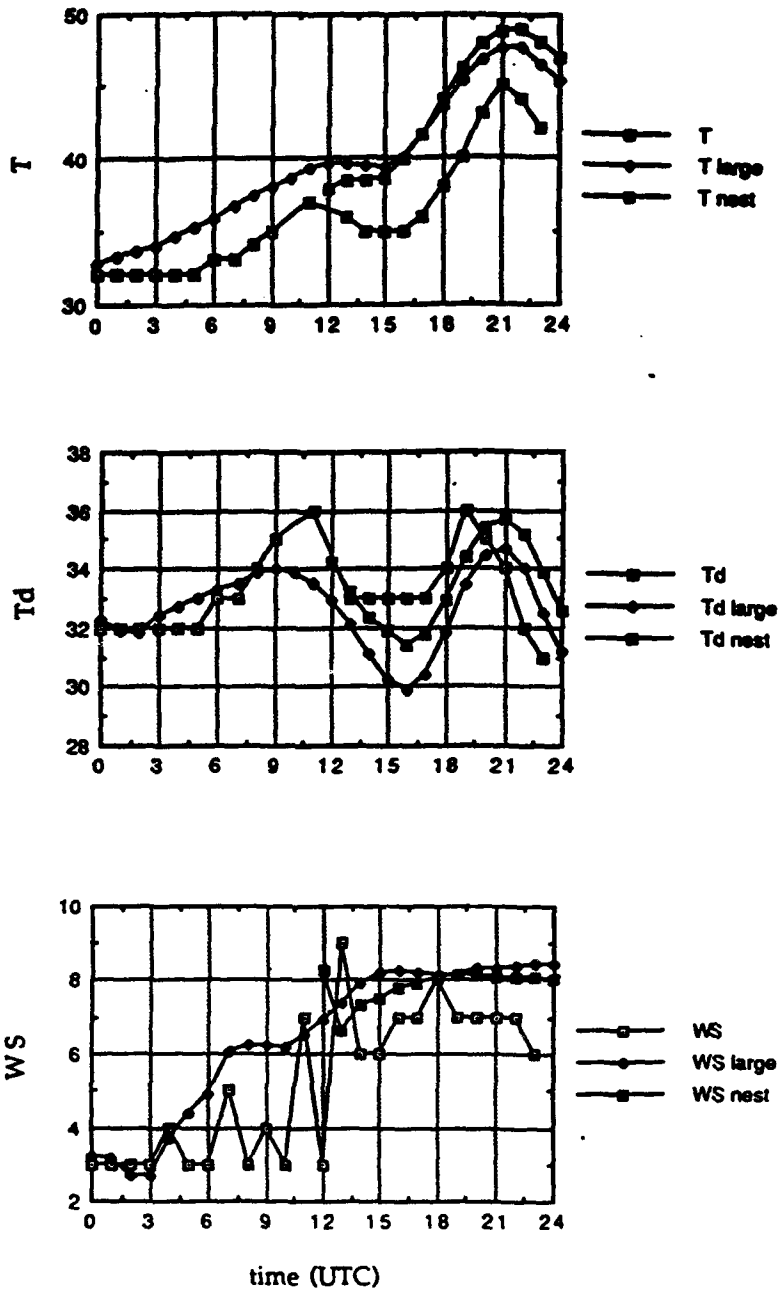

***Figure 8-28** The diurnal evolution of: (a) temperature (°F), (b) dew point (°F), and (c) wind speed (m s^{-1}) during 10 December 1992. at Columbia, MO. The first curves (open boxes) represent the observed fields, and the other two lines are taken from model grid points nearest to the station location for the large scale (50 km) and nested (15 km) simulations for that day.*

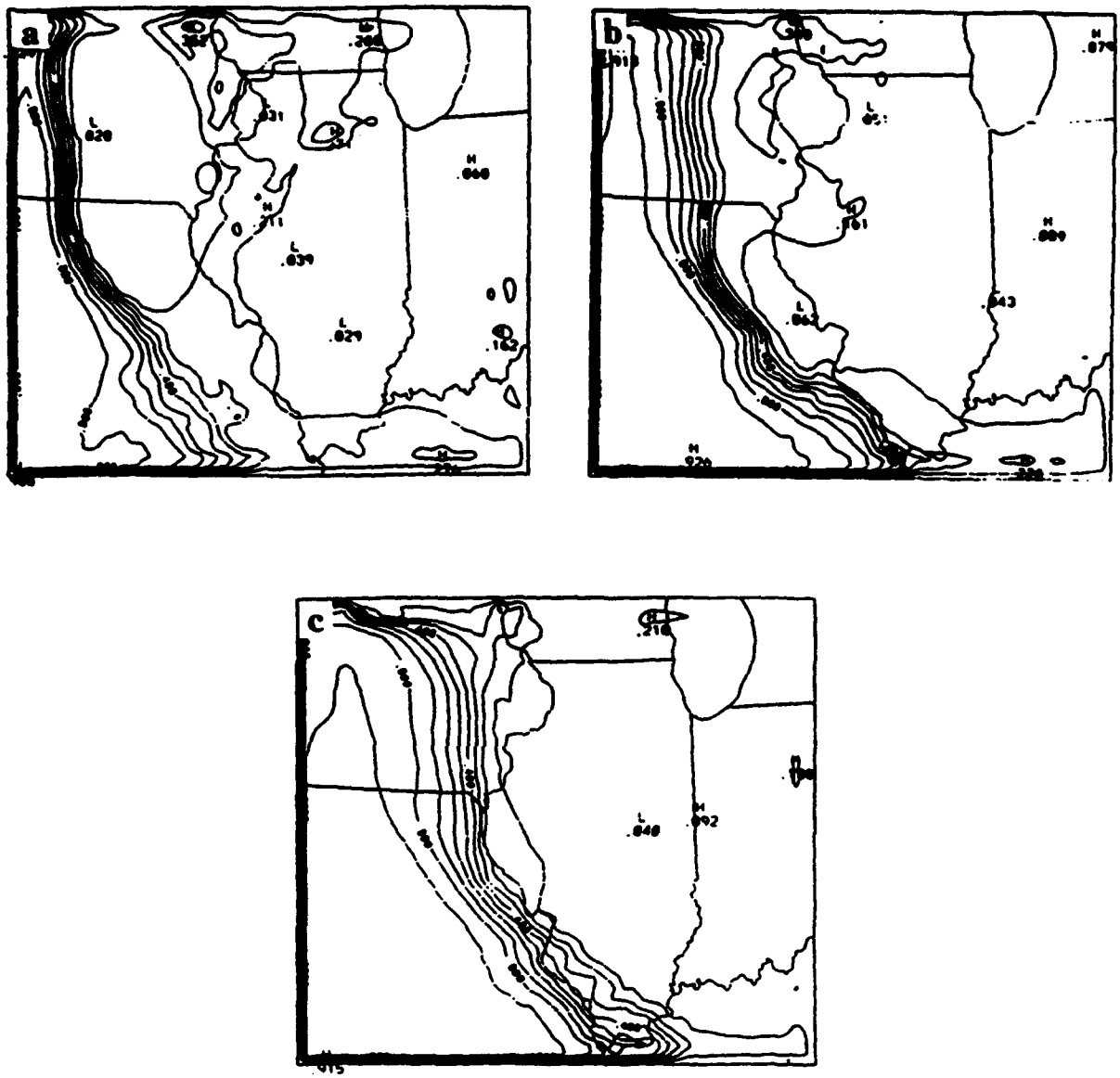

Figure 8-29 The MASS model shortwave transmissivity field at: (a) 1500 UTC (b) 1800 UTC, and (c) 2100 UTC 10 December 1992. Low values of transmissivity indicate the presence of optically thick cloud cover, either explicitly simulated or inferred from the relative humidity field.

9. Development of Graphical Interface

The graphical interface for the MASS simulation system was originally planned to be designed for a NeXT Color Cube system using an Interface Builder under the NeXTstep environment. Because of the use of Motif for the IMETS system at the ASL, there was a shift in the development of the graphical interface from the NeXTstep environment to the X Windows/Motif environment. This approach has produced an X Windows/Motif-based interface that will be consistent with the Army's software standards, and hopefully, one that can be implemented as part of the IMETS system in the future if desired. This development was done on the Stardent 750 which was delivered to ASL.

9.1 Design of the GUI

The Graphical User Interface (GUI) was developed using the Motif Resource Manager (MRM), which allows widgets (i.e. button and text boxes) to be created based on information contained in separate input files called User Interface Definition (UID) files. The information contained in these files includes the location and sizes of different features, text font choices, labels and titles and default initial choices. These files are separate from the main source code written in C, which compiles very slowly due in part to the large X and Motif libraries needed. The separation of the UID files from the C source code allows the developer to dramatically improve his efficiency by modifying the UID files rather than the C files when designing the structure of the windows. Features can quickly be re-sized and moved around or renamed in the UID files and tested.

The GUI was designed so that the user can modify and produce the necessary input files for the preprocessor and model as well as submit preprocessor, nudging or model runs completely from the screen. The design of the menus is shown in Figure 9-1. The top menu (Figure 9-2) has options for configuring either the preprocessor or the mass option files or setting up and submitting a simulation. If the user chooses to configure input option files, subsequent menus let the user choose which specific option file he would like to generate. These option files will be created and stored in the current directory of the user at the time the GUI was started. There are six configuration menus for the preprocessor as listed in Figure 9-3a, for the six different modules: ***prepgrd***, ***prepdat***, ***prepro***, ***prepbog***, ***prepbc*** and ***prepnudg***. There are three configuration menus for the MASS model (Figure 9-3b), one for the MASS model and two for the SRPH and nudging sections of the MASS option file. The configuration of any of these three menus results in the generation of the same *mass.opt* option file. If the user chooses to configure and submit a simulation, the submit menu (Figure 9-4) allows the user to do any or all of the following:

(1) Choose the Preprocessor Init Tag and run any or all of the preprocessor modules.
(2) Run the nudging module for up to six different nudging times.
(3) Choose the Model Run Tag and run the MASS model.

The configuration menus for the six different preprocessor modules are shown in Figures 9-5 through 9-10. These menus allow the user to completely define the input parameters needed by the preprocessor to run a simulation. The three configuration menus needed to run a MASS simulation are shown in Figures 9-11 through 9-13.

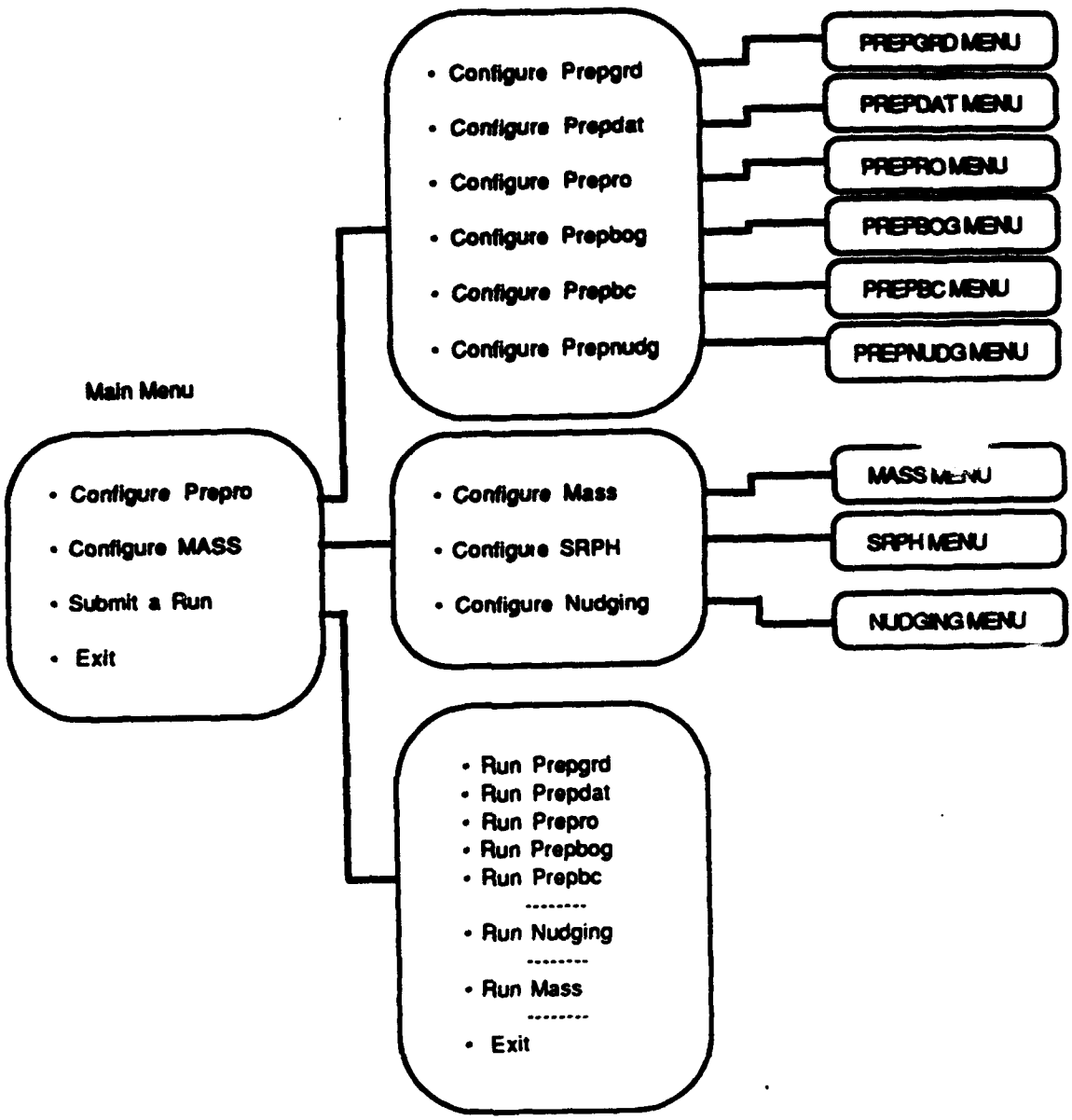

Figure 9-1 Schematic diagram of the basic graphical interface structure.

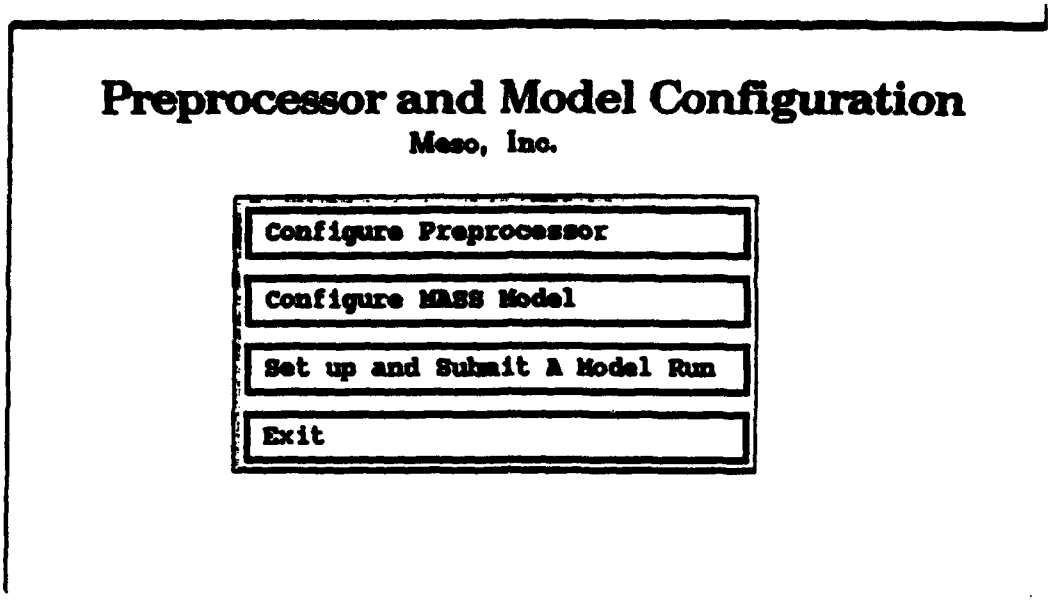

Figure 9-2 The top menu in the imass interface.

a

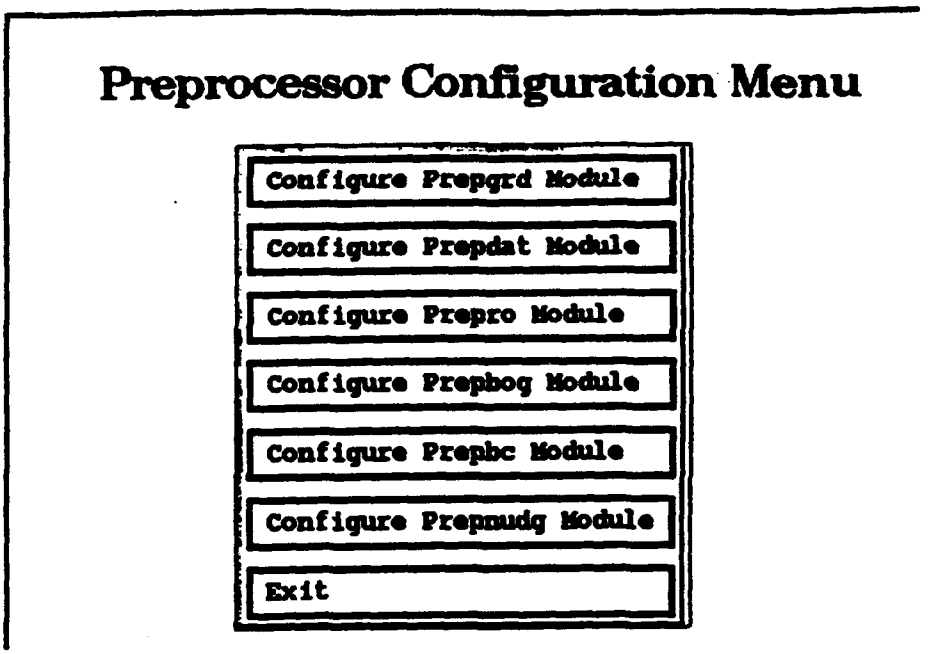

b

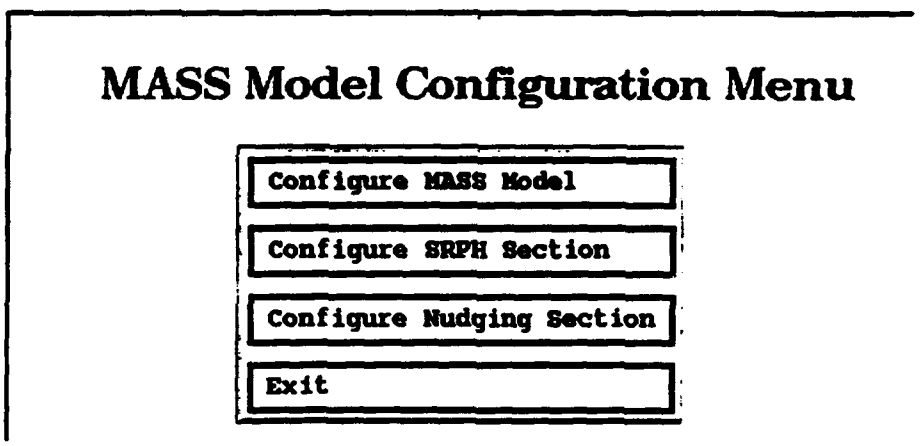

Figure 9-3 The top menu lists for the : (a) preprocessor and (b) MASS model.

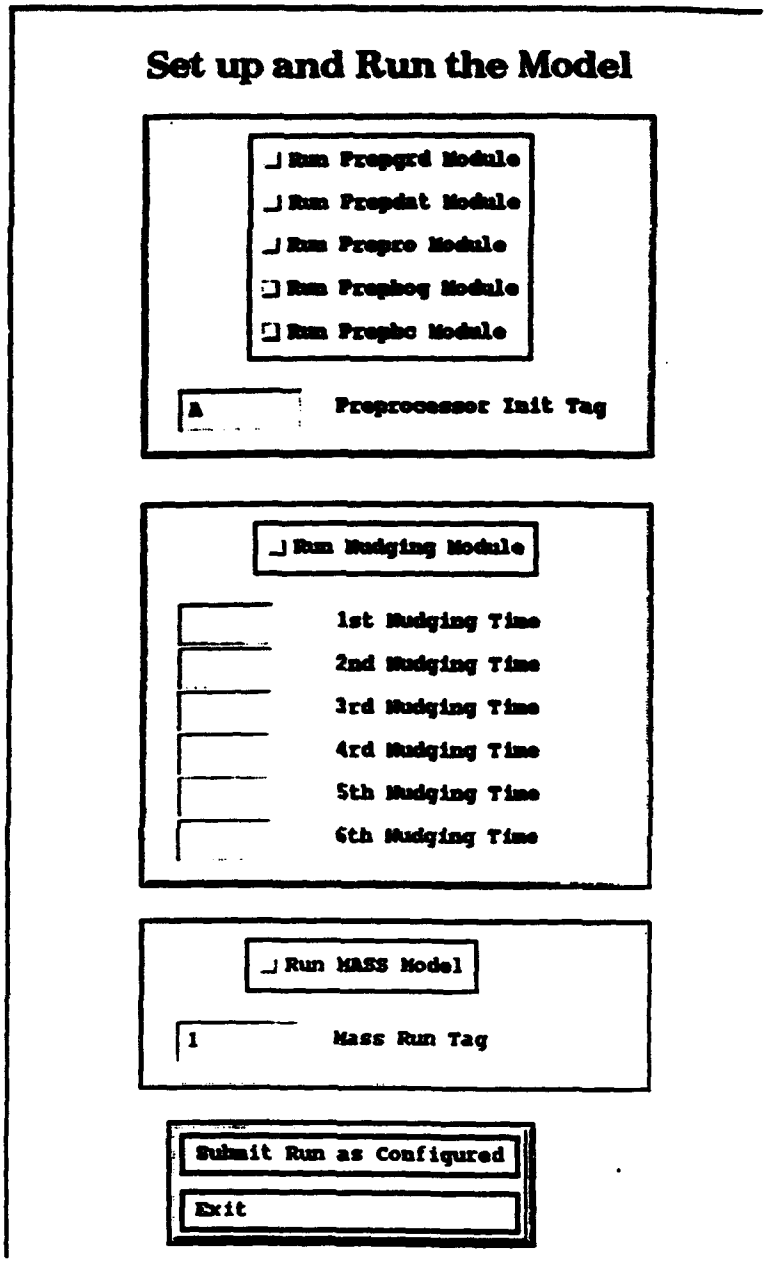

Figure 9-4. The submit menu for the MASS modeling system.

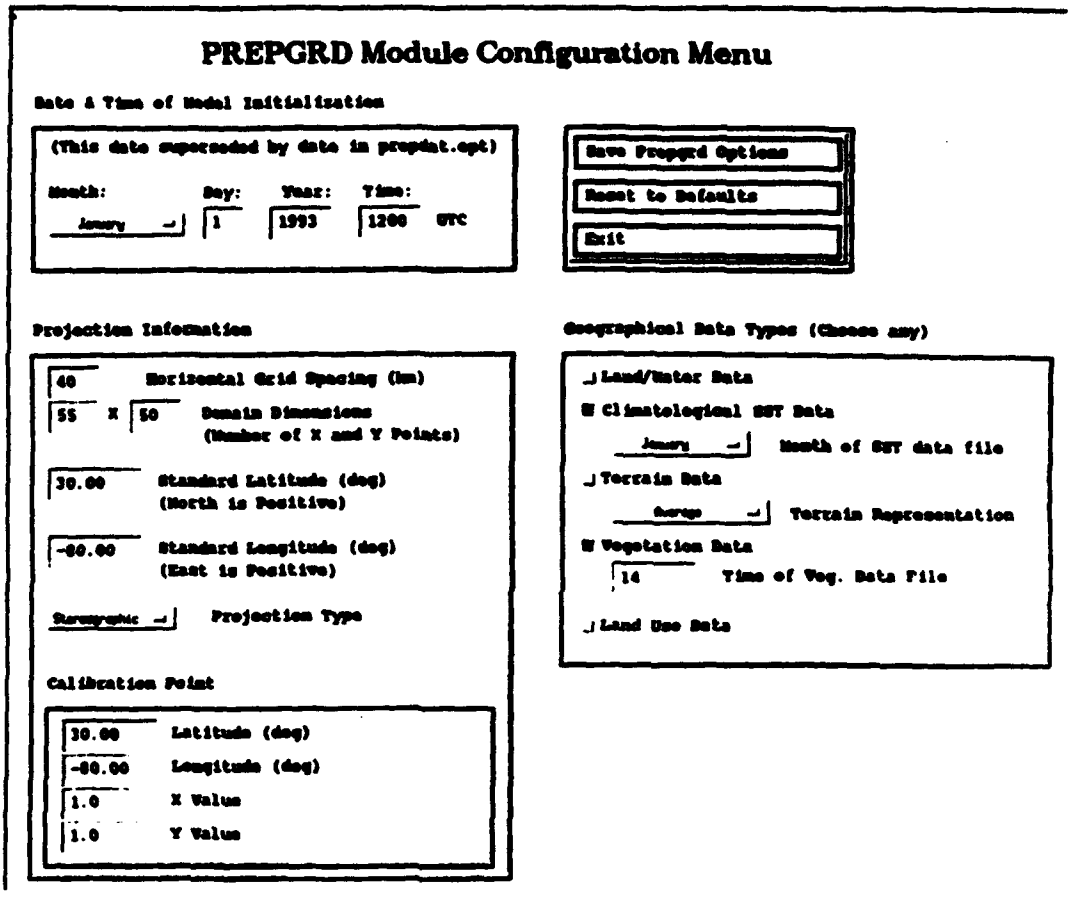

Figure 9-5. The prepgrd configuration menu.

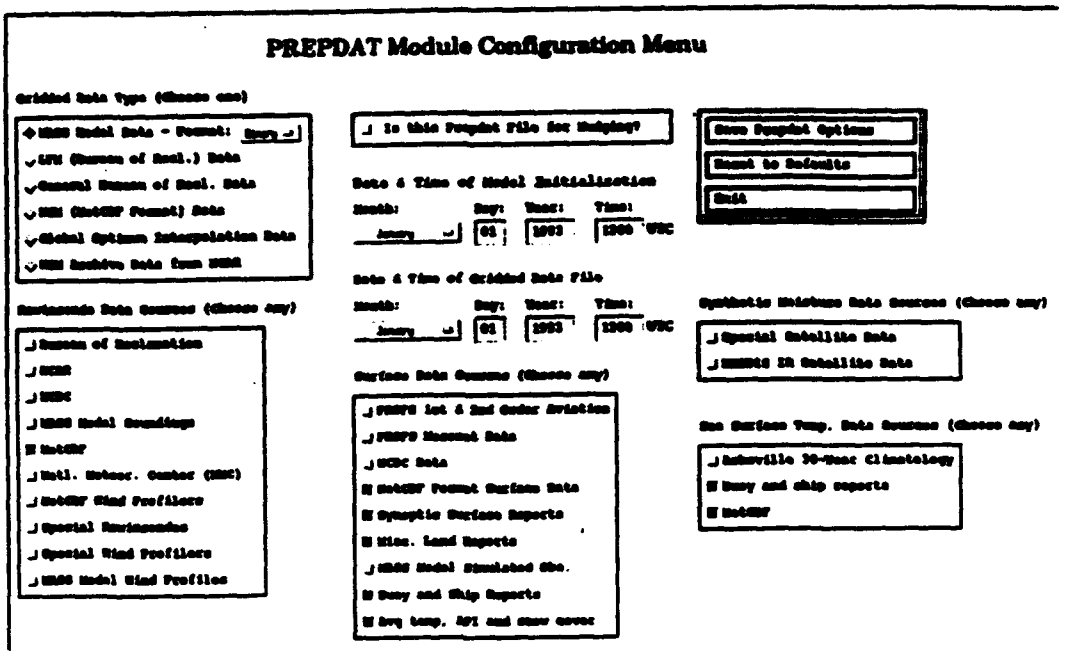

Figure 9-6. The prepdat configuration menu.

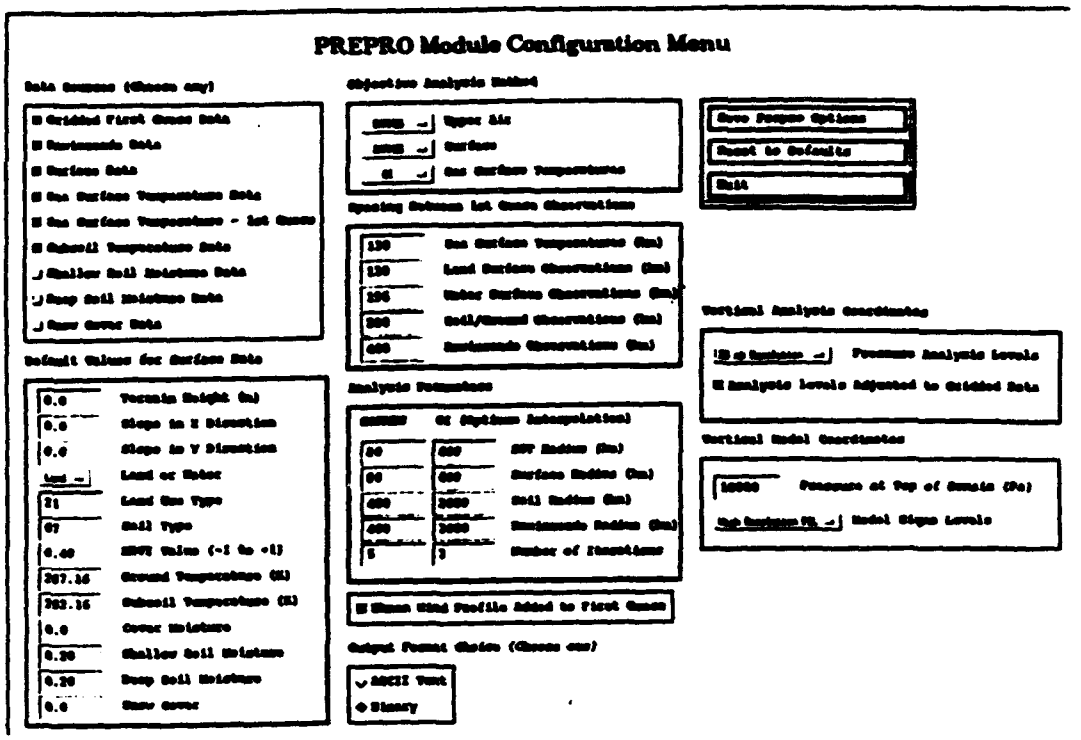

Figure 9-7. The prepro configuration menu.

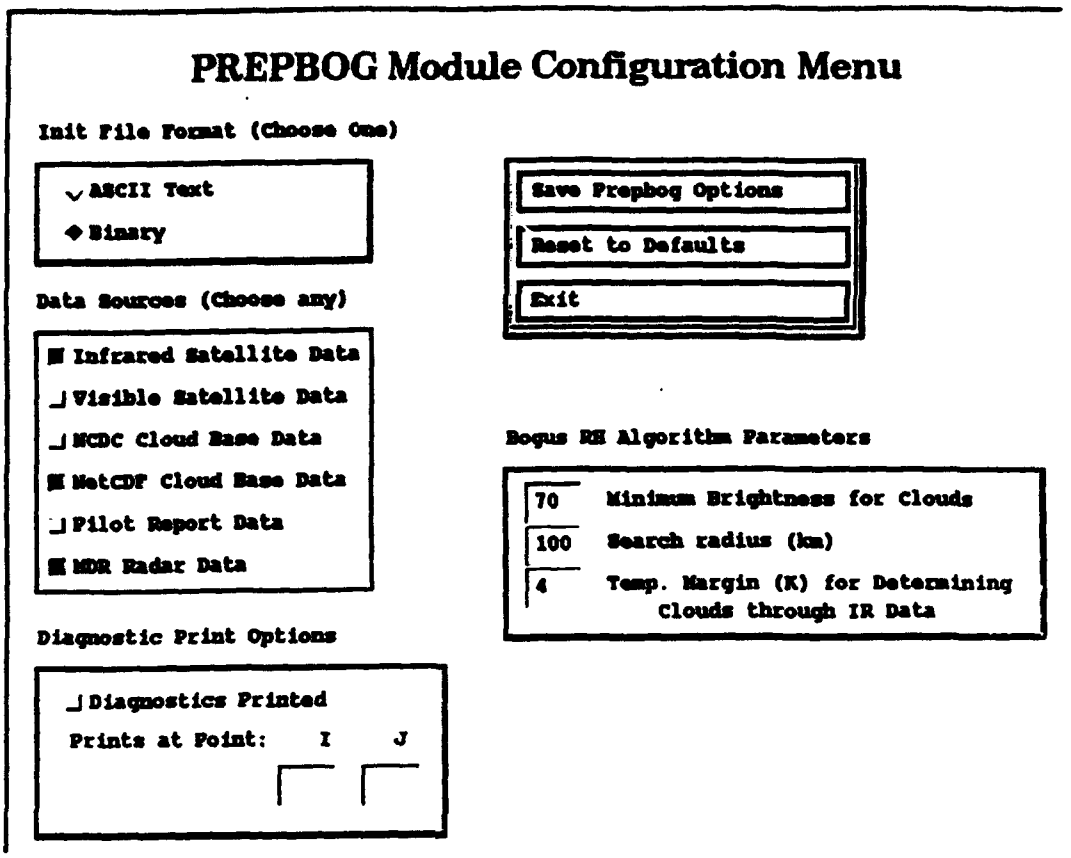

Figure 9-8. The prepbog configuration menu.

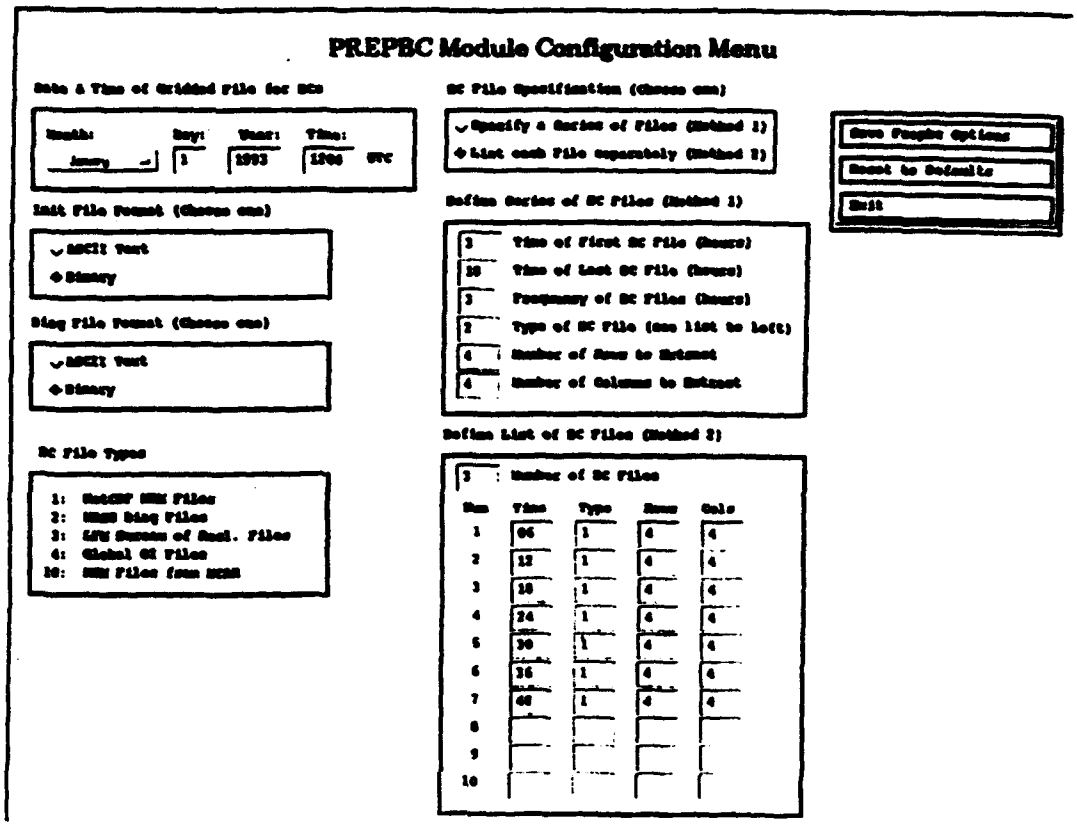

Figure 9-9. The prepbc configuration menu.

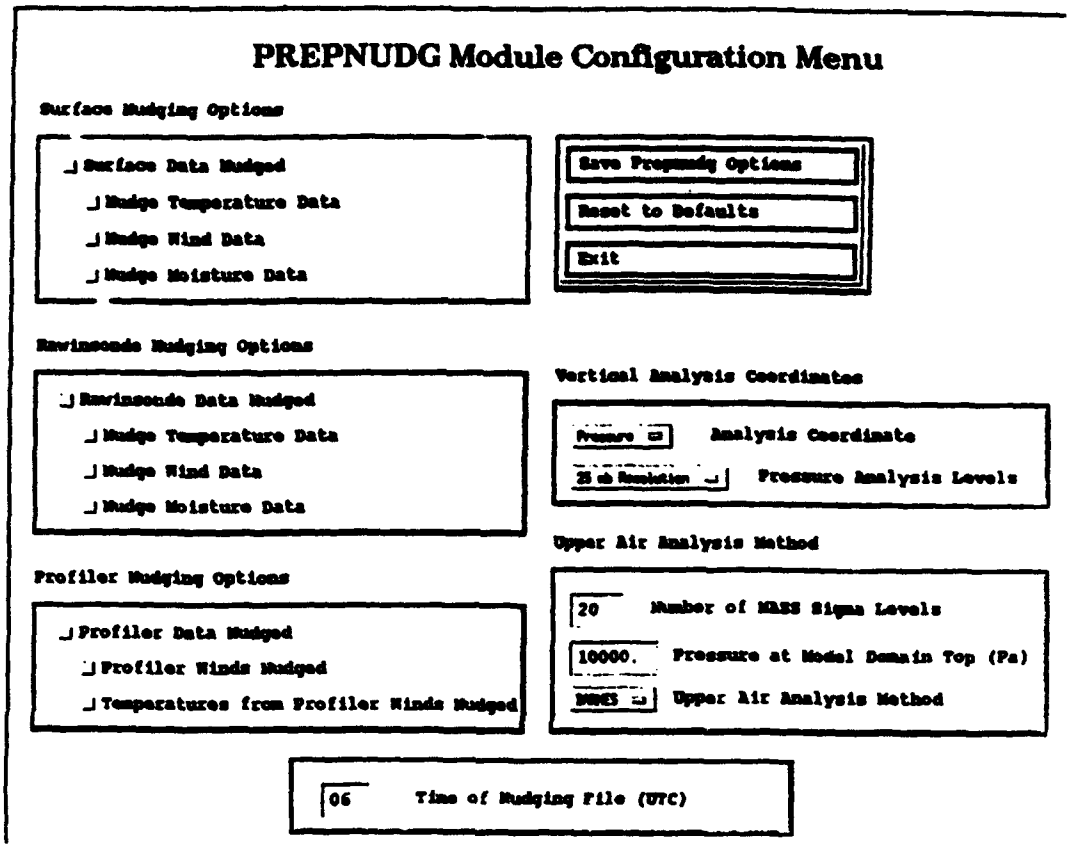

Figure 9-10. The prepnudg configuration menu.

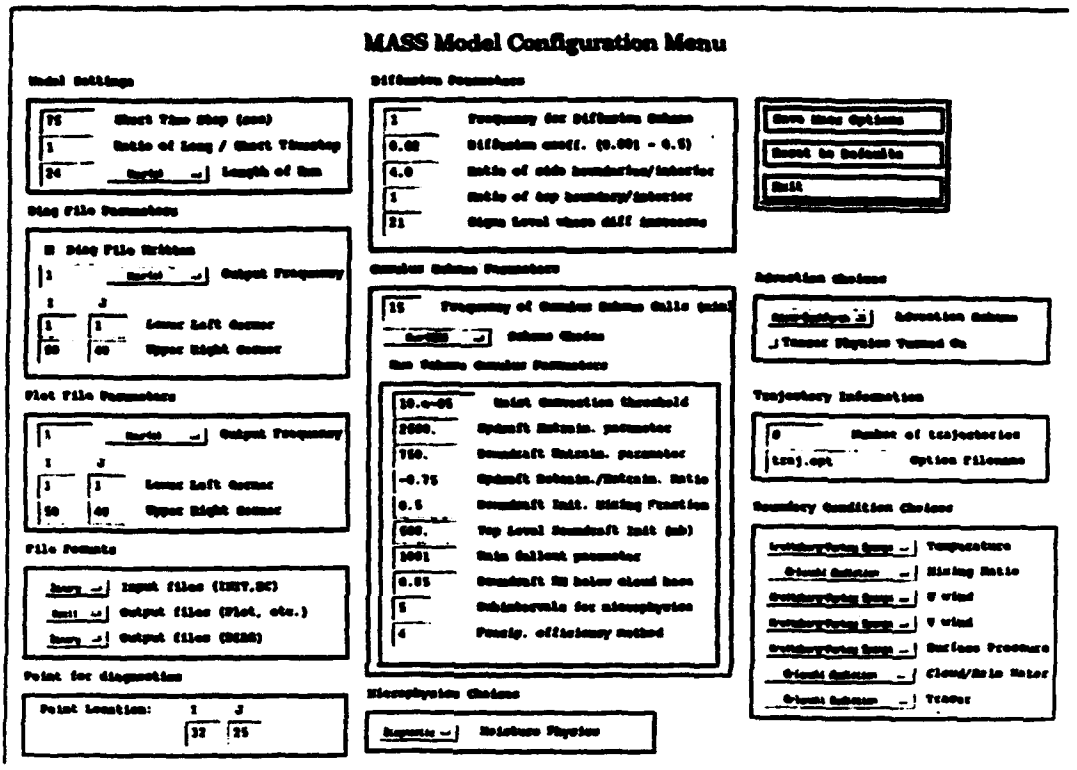

Figure 9-11. The MASS configuration menu.

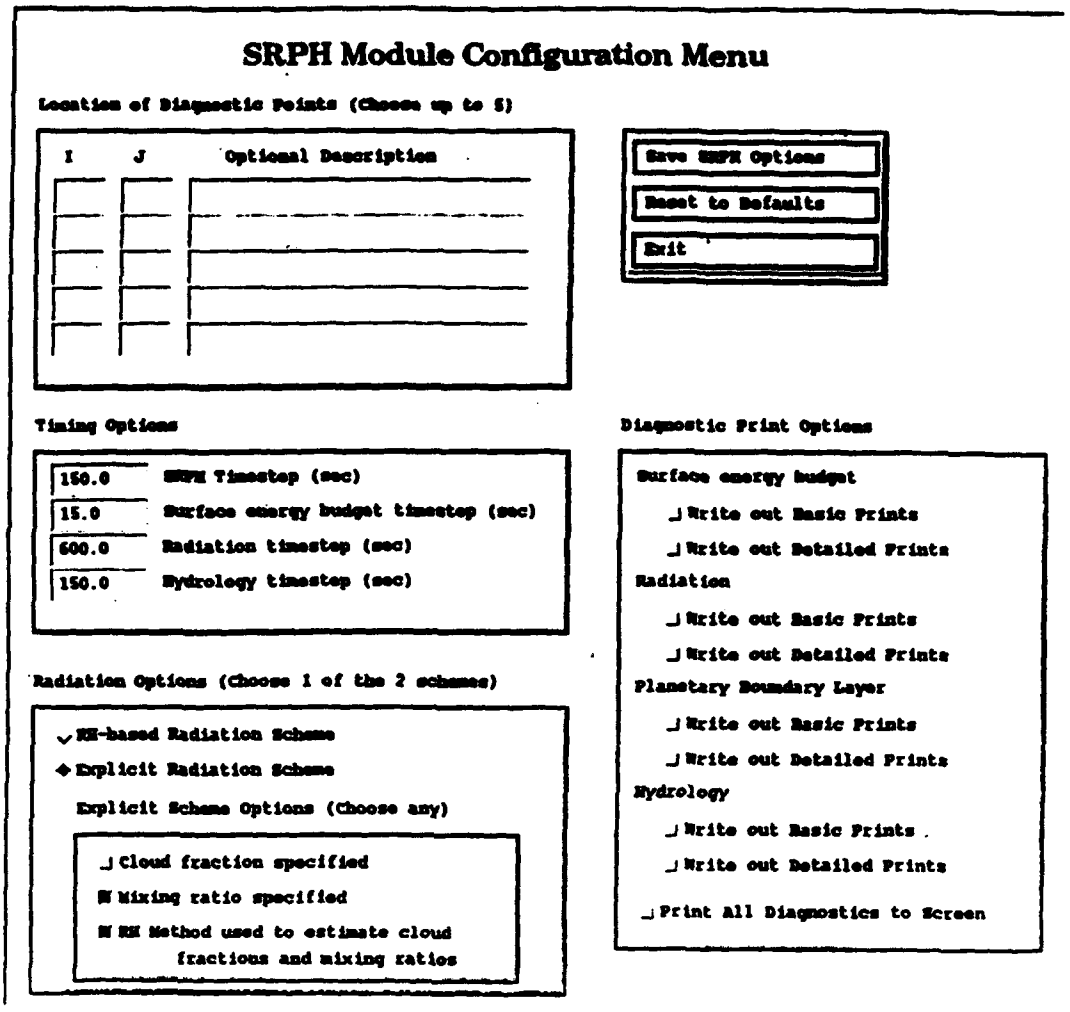

Figure 9-12. The SRPH configuration menu.

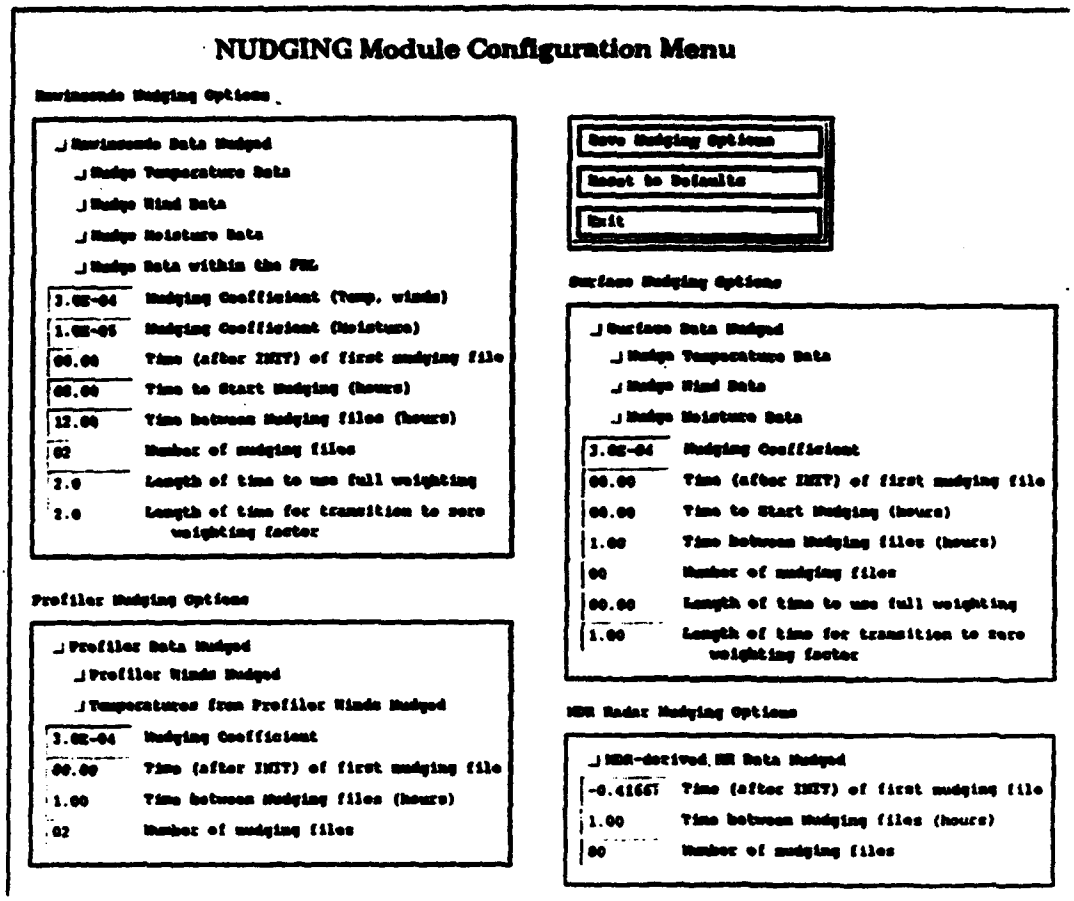

Figure 9-13. The Nudging configuration menu.

10. Summary and Conclusions

The fundamental achievement of this SBIR project was the creation of a self-contained mesoscale atmospheric simulation system which can generate real-time or historical simulations on a high performance moderate-cost workstation computer. The system can: (1) ingest a variety of atmospheric data types; (2) combine the diverse mixture of ingested data into a dynamically consistent initialization dataset for the numerical model; (3) generate a mesoscale numerical simulation; and (4) display the output from the simulations in a variety of formats. A review of the significant accomplishments during the development and evaluation of the system is presented in Section 10.1. A discussion of the areas in which additional research is needed to improved the mesoscale simulation system is presented in Section 10.2.

10.1 Project Summary

The project consisted of three significant components. In the first portion of the project, the workstation-based mesoscale atmospheric simulation system was created by porting a version of the Mesoscale Atmospheric Simulation System (MASS) from a supercomputer to a Stardent 750 vector processing workstation, and then upgrading the system by implementing: (1) a new lateral boundary condition scheme; (2) a positive definite advection formulation; (3) a more sophisticated surface energy and moisture budget formulation; (4) a four-dimensional data assimilation system based on a Newtonian relaxation scheme; and (5) a method to enhance the initialization of relative humidity through the use of satellite image data, MDR reports, pilot reports and surface cloud observations. In the second portion of the project, a graphical user interface (GUI) was developed to permit the user to easily reconfigure the system and execute simulations, and the model software was modified to increase its computational performance on the workstation computer. The final segment of the project consisted of the execution of a observation system simulation experiment (OSSE) to test the performance of the data assimilation system, and the execution of 36 real data simulations to evaluate the performance of the simulation system in a variety of environments.

The first improvement to the modeling system in this project was the implementation of a radiative lateral boundary condition formulation. The formulation was based on the scheme described by Orlanski (1976). In this scheme, atmospheric features which approach the lateral boundaries are permitted to propagate through the boundary by calculating a composite phase velocity at each boundary point and allowing the features to propagate through the lateral boundary with this phase velocity. This formulation improved the quality of the simulations near the lateral boundaries and also reduced the portion of the model domain (i.e. the number of grid points) devoted to the implementation of the boundary conditions. Under the previous Kreitzberg-Perkey sponge boundary condition, four boundary rows and columns were required to blend the external and internal tendencies and filter the outwardly propagating features from the model domain. This effectively reduced the useful portion of the model matrix (i.e. the portion in which the evolution of the prognostic variables is determined solely by the model physics) by 8 grid points along each coordinate axis. In contrast, the radiative scheme utilizes only the outermost row and column for the specification of the boundary conditions and there is no necessity to have a highly diffusive sponge region for several rows or columns adjacent to each lateral boundary.

The quality of the modeling system was also improved in this project by the implementation of a positive definite horizontal advection scheme with low implicit diffusion for the advection of liquid and frozen water substances and any passive tracer substances that the user decides to include in a model simulation. The advection scheme is a version of the MPDATA scheme originally formulated by Smolarkiewicz (1983a, 1983b). This scheme has the

ability to maintain sharp boundaries in simulated fields while not generating spurious numerical oscillations which cause unrealistic negative values to appear in proximity to regions of strong gradients. The scheme was extensively tested in idealized one-dimensional and two-dimensional simulations before it was implemented into the three-dimensional version of the MASS model. It will be possible to implement this advection scheme for all of the model prognostic variables in the future with a modest additional effort.

Various parts of the surface and planetary boundary layer parameterization schemes were significantly improved as a part of this project. A better method of calculating evapotranspiration from land surfaces was formulated, in which the transpiration from plants is sensitive to the fractional vegetation cover (inferred from remotely-sensed vegetation index data) and land use type, as well as soil moisture. Evaporation is also parameterized from bare soil, and from a cover moisture reservoir consisting of intercepted rainfall and dewfall. As a part of the evapotranspiration effort, the model hydrology framework was extended to two soil layers and the cover reservoir, and parameterizations for rainfall interception and snow cover were added.

Tests were made with the initialization of surface and subsoil temperature. It was found that the model is quite sensitive to subsoil temperature, especially in the simulation of nighttime low temperatures. Using an average temperature over the previous few days seems to be a reasonable way to initialize the subsoil temperature.

A formulation for the inclusion of slope effects on the shortwave radiation received at the surface was also added to the model. The local terrain slope magnitude and slope azimuth are used to calculate a corrected solar zenith angle, which replaces the actual zenith angle in the radiation equations. For high resolution nested simulations, the grid-resolved terrain slopes can be large enough to significantly alter the local radiation budget.

The initialization of the mesoscale simulation model was improved in this project by implementing four types of four dimensional data assimilation (FDDA) schemes and an innovative method of static moisture initialization. These FDDA schemes include (1) Newtonian relaxation or nudging of gridded rawinsonde, surface or profiler observations (Hoke and Anthes, 1976) in which the model state is relaxed towards an analysis of observations; and (2) the use of Manually Digitized Radar (MDR) data to specify moisture convergence (precipitation rates) in areas which are (are not) subject to convection according to the Kuo-MESO cumulus parameterization scheme. The static moisture initialization is based upon the enhancement of the three dimensional moisture analysis through the use of surface observations of clouds, pilot reports, MDR data and infrared satellite images. The surface, rawinsonde and profiler nudging schemes are similar to the schemes used by Stauffer, et al., (1991). The most significant changes from Stauffer, et al., (1991) are an improvement in the method of calculating the analysis confidence factors and a scheme to improve the surface analysis near coastlines. Temperatures are derived from the profiler wind field through the inversion of the divergence equation (Cram, et al., 1991) and assimilated along with the wind field.

Simulation experiments indicated that the assimilation of MDR data helped to accurately define both the grid scale and subgrid scale precipitation field at the time of model initialization. The benefits of MDR assimilation typically lasted for about 6 to 9 hours. They were most dramatic during the initial three hours of a simulation due to the elimination of the precipitation spin-up problem that is common to all numerical models.

The synthetic RH scheme is most valuable when simulating cases with weak or nonexistent synoptic forcing and strong boundary layer forcing. In these situations, convection is often triggered by differential heating due to meso-β scale variations in cloud cover. The synthetic RH scheme is the component of the model data assimilation system which is most effective at adding such fine scale variations in cloudiness.

The results of the observing system simulation experiment (OSSE) indicated that the main benefit of nudging is the reduction of the spin-up problem during the initial 3 to 6 hours of a simulation. After this time, nudged simulations were inferior to a statically initialized

simulation because the nudged simulation had to be initialized 12 hours earlier. The poor performance of the nudged simulations after 6 hours was most likely due to the fact that the boundary conditions were based on an NGM 12 hour forecast rather than "observations" from a surrogate atmosphere simulation (SAS). During the assimilation period and the first 6 hours of the forecast, this inferior boundary condition information propagated across a large enough portion of the model domain to degrade the simulation. The results of the case of 5-6 September 1992 indicate that the assimilation of rawinsonde data produces the greatest improvement, while surface data is less valuable and profiler data suffers from a lack of information about the mass field. Since the OSSE consisted of only 1 case, these results are not necessarily true for all conceivable situations. For cases with weak forcing, the assimilation of rawinsonde data may be less important while surface data assimilation may have a greater impact. Stauffer et al. (1991) found this to be true in their weak synoptic forcing case.

Given an abundance of time and other resources, OSSEs have the potential to expand the understanding of data assimilation beyond the limited results presented here. Several potentially valuable experiments must wait for another opportunity. They include:

1) the use of observations from the SAS, rather than output from a numerical model, to provide boundary condition information. This may help to reduce the degradation of the simulation which occurs when forecast boundary condition data propagates into the domain during the data assimilation period.
2) creating a technique to simulate MDR, IR satellite and other non-standard data from the SAS so that the MDR assimilation scheme and the synthetic RH scheme could be tested.
3) testing the effects of the temporal and spatial distribution of the simulated observations on the numerical forecast.

Quite a large number of MASS simulations were performed for this project, including both the OSSE simulations and those simulations performed as part of the 36-case sample. Table 10-1 summarizes the types of phenomena that the model tended to simulate well and those types of features which were consistently difficult to simulate. Some of the strengths and weaknesses are characteristic of mesoscale modeling in general, and some are peculiar to MASS. Model problems can be separated into two main categories: (1) those which arise from a lack of initial or boundary data of sufficient resolution, frequency, or quality; and (2) those which are caused by shortcomings in the model physics, arising either from inadequate understanding of the physical process, or from constraints imposed by the model numerical formulation or by model characteristics such as the grid spacing. Convective and cloud phenomena are the areas in which mesoscale models can make the greatest improvement over current operational models. Despite some successes in these areas, profound difficulties remain in the parameterization of convection and other cloud processes.

Table 10-1 Types of meteorological phenomena which were generally well-simulated or difficult to simulate with the Mesoscale Atmospheric Simulation System.

Consistently Well-Simulated Events	Difficult to Simulate Phenomena
• Synoptic or meso-α scale features which are well-resolved by the rawinsonde network.	• Convective events which are only weakly forced by larger scale circulations, i.e. quasi-barotropic systems.
• Convective events which are strongly forced by larger scale circulations.	• Features which result from convective feedback to the grid scale, e.g. from latent heating, downdrafts, cool outflows, etc.
• Mesoscale circulations which are tied to surface features that are well-represented, e.g. land/sea breezes, terrain-induced circulations.	• Mesoscale circulations which are driven by more subtle surface gradients, especially soil moisture.
• Surface and boundary layer flows occurring under quiescent (clear, non-convective) conditions.	• Circulations driven by cloud boundary effects.
	• Features in the vicinity of large terrain gradients.

An always-important issue in numerical weather prediction is the computational time required to make simulations. With the many different model options, a wide range of speeds can be obtained on a given grid, depending on the model physics selected, and the frequency at which parameterization schemes are invoked. The Stardent 750 Workstation has proven to be an effective platform for the MASS preprocessor and model, and the ability to add another processor would increase the speed considerably. At the end of the 36-case sample simulations, the time required to make a 24 hr large scale run on a 55 × 50 domain with a grid spacing of 50 km was about 3.7 hr. The nested simulations take longer, because of the much shorter timestep: 20 s versus 75 s for the large scale runs. A 12 hr nested simulation on a 55 × 50, 15 km grid took about 4.9 hr on the Stardent 750. These times are a little slow for operational use, but the Stardent line of workstations is more than two years old, and much faster machines are now available. A great advantage of the Stardent is the ability to perform vector processing, a capability which is currently available only on much more expensive computers, and is not available on fast, new workstations such as the Hewlett-Packard 9000 series (the "Snake") and the new "Alpha" workstations from Digital Equipment Corp. These machines are much faster on scalar calculations than the Stardent's MIPS R3000 processor, but it remains to be seen how much is lost by the absence of vector processing. Some parts of the MASS model (advection, diffusion) vectorize very well, significantly speeding up the execution of the code. On the other hand, some parts of the model (surface and microphysical parameterizations) do not vectorize well, and would benefit greatly from faster scalar processing power. Figure 10-1 shows the percentage of execution time required for the major parts of the model when the code is compiled with the vectorization option. The most time-consuming single component of the model is the SRPH scheme (Surface energy budget-Radiation-Planetary boundary layer-Hydrology).

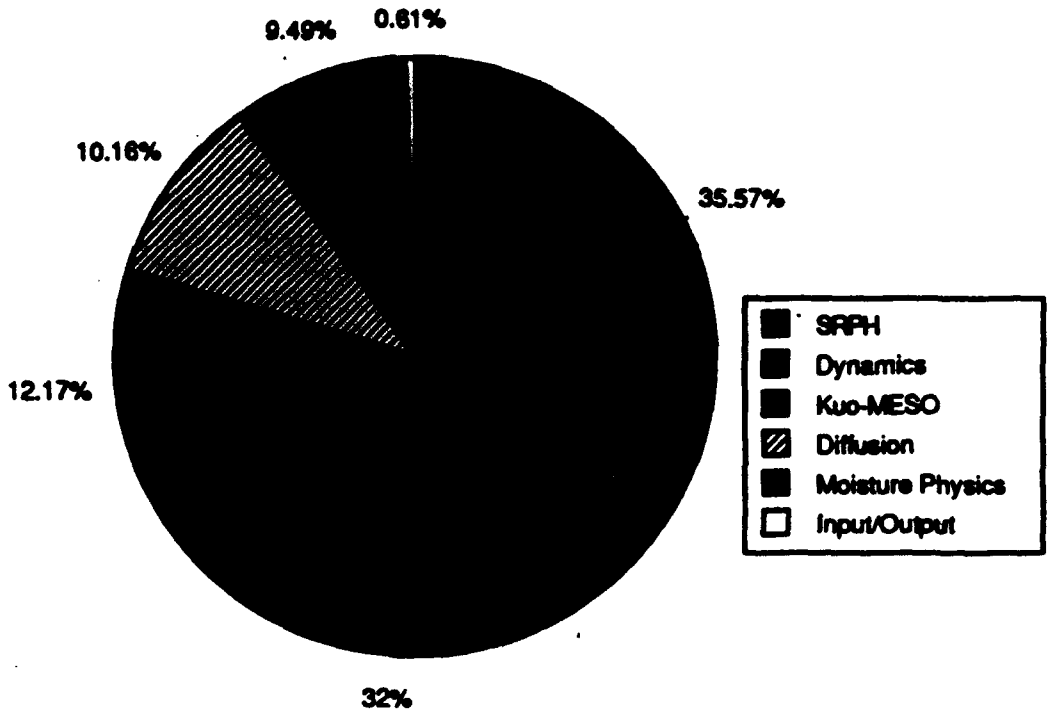

Figure 10-1 *Percentage of model execution time required for major parts of the MASS model. The run used for this breakdown was a 45 km simulation on the Stardent 750, with nudging off, the prognostic microphysical scheme on, and the Kuo-MESO convective parameterization scheme on. All the modules were optimized with the vectorization option of the Stardent FORTRAN compiler.*

10.2 Areas for Future Development

Despite the substantial progress that has been made in the development of mesoscale models during the past decade, and the widespread use of these systems in recent years, there are still a number of problem areas that need to be addressed before mesoscale simulations can achieve their ultimate potential. The major issues that need to be addressed include: (1) the parameterization of moist convection and its interaction with grid scale moisture physics; (2) the parameterization of the boundary layer; (3) the modeling of surface processes; (4) the representation of clouds and their interaction with radiative processes; (5) the availability of sufficient data to define mesoscale features in the initial state; (6) the assimilation of data from new observing systems into the mesoscale model in a beneficial manner; and (7) the endless need for higher computational performance. A brief review of each one of these problem areas will provide an indication of the direction of the future development of MASS and other mesoscale models

One of the most critical problems is the parameterization of the grid scale effects of the sub-grid scale processes associated with shallow and deep moist convection in mesoscale models with grid increments between approximately 5 km and 20 km. A review of the many unresolved issues of convective parameterization at this scale has been compiled by Molinari and Dudek (1992). At this resolution, the mesoscale model partially resolves the convective-scale circulation but cannot resolve the intense updrafts and downdrafts which accomplish much of the vertical transport of energy, moisture and momentum. Thus, the parameterization scheme must simulate the grid scale effects of the large vertical transports which occur in the updrafts and downdrafts, but not duplicate the effects of the processes which are resolved on the mesoscale grid. If a parameterization is not used at this scale, the absence of the vertical transport by convective-scale updrafts and downdrafts frequently results in the spurious feedback process which can unrealistically amplify convective systems. The parameterized updrafts and downdrafts work against the spurious feedback by transporting heat and moisture upward. The proper approach to the parameterization of convection at this scale is still subject to considerable debate. Most mesoscale modelers have simply utilized schemes such as those formulated by Kuo (1965) and Anthes (1977), that were intended for use in models with grid spacing larger than 20 km. Two schemes were expressly designed for models with grid increments in the 20 to 25 km range: the schemes of Fritsch and Chappell (1980) and Frank and Cohen (1987). A mixed set of results has been documented. An appealing approach is to avoid the entire moist convection parameterization issue by explicitly simulating the convection with a non-hydrostatic cloud scale model executed over a mesoscale domain. A few experimental simulations of this type have been performed with a non-hydrostatic version of the CSU RAMS model, but computational requirements will restrict such simulations to very small domains for the immediate future. Thus, the improvement in convective parameterization schemes will play an important role in determining the skill of a mesoscale model to simulate the evolution of mesoscale convective systems. However, cloud-scale simulations of mesoscale systems will undoubtedly provide an important dataset with which to understand how to parameterize convective systems in mesoscale models.

The parameterization of the boundary layer is another area in which mesoscale models can be improved. A key component of the boundary layer parameterization problem is the interaction of the model's boundary layer parameterization with shallow and deep convective clouds that are rooted within the boundary layer. However, most boundary layer parameterization schemes do not directly interact with clouds that extend into the middle and upper troposphere.

The representation of surface processes is also an important contributor to the skill of a mesoscale simulation. A key issue in this area is the calculation of the area-averaged surface moisture flux over land surfaces. The flux of moisture from the surface of the earth into the atmosphere is the result of direct evaporation from the surface soil layer and the material on top of the soil (e.g. vegetation, pavement) as well as the transpiration from vegetation which extracts water from the soil layer below the surface layer. The time dependent area-averaged transpiration from a plant canopy is a very difficult quantity to calculate because of the heterogeneous transpiration rates of plants resulting from (1) their different locations in the canopy; (2) the intrinsic physiological properties of different species; and (3) large variations in soil properties and moisture contents over small distances underneath the canopy. Surface heterogeneity also poses a significant problem to the calculation of area-averaged direct evaporation. A significant obstacle to the accurate modeling of this process is the lack of quality observed evaporation and transpiration data over a wide variety of surfaces. Field experiments such as FIFE (Sellers et al., 1988) have gathered detailed measurements of evapotranspiration over only a few types of mostly homogeneous surfaces.

The simulation of clouds and their interaction with short wave and long wave radiation can be crucial to the quality of a mesoscale simulation. For example, the quality of a simulation

of low level circulations that develop due to the differential heating of the surface between cloudy and clear regions, is heavily dependent on the model's ability to accurately simulate radiative processes in the cloudy and clear regions. There are two significant issues related to this problem area. The first issue is the representation of clouds in the mesoscale model. One criteria to determine the presence of clouds in a model layer is the existence of significant amounts of simulated cloud water (ice) or rain water (snow). However, cloud water (ice) or rain water (snow) can only exist in a grid cell for a significant amount of time if the air in the cell is saturated. This means that the entire grid cell will either be cloudy (if the grid scale is saturated) or clear if this is the only mechanism for cloud specification in the model. This is clearly not realistic at the mesoscale since a significant amount of cloudiness can exist in a grid cell even when the grid cell average relative humidity is somewhat below 100%. This is typically represented in mesoscale models by using a cloud fraction-relative humidity relationship to specify a fractional coverage of clouds in layers where the relative humidity is below 100% but above a threshold value (e.g. 80%). These clouds are considered to be sub-grid in scale and hence are not represented in the grid scale cloud water (ice) or rain water (snow) fields. However, these clouds do interact with the radiative parameterization and thus can have a significant impact on the surface energy budget. Unfortunately, the relationship between layer cloud fraction and relative humidity is subject to a considerable amount of scatter due to the multiscale processes which generate and destroy clouds. It will most likely be necessary to utilize other parameters in addition to relative humidity to obtain a reasonable estimate of the fraction of a model layer that is covered by clouds. A considerable amount of additional research needs to be done on the relationship of grid scale variables to layer cloud fractions. If this is not a difficult enough problem, it must be remembered that in addition to the fractional coverage, the optical depth (i.e. the liquid or frozen water content) of the parameterized clouds must be known in order to calculate the radiative effects of the clouds. A second issue relates to the way in which the radiative calculations are performed. The execution of a comprehensive radiative transfer formulation within a mesoscale model is not computationally feasible at present or in the near future. Therefore, simplified parameterizations must be used. The challenge is to create a computationally efficient radiative scheme that can simulate the important aspects of the radiative effects of both parameterized and explicit clouds in a mesoscale model.

A long standing problem for mesoscale modelers has been the lack of data with which to define mesoscale circulations at the time of initialization of a mesoscale model. In the past, rawinsonde data has been the foundation for the preparation of the initialization datasets for mesoscale models. With an average separation of about 400 km between observing sites, the rawinsonde network cannot resolve meso-β scale features and can provide only a marginal representation of meso-α scale systems. Surface, satellite and aircraft data have provided some information about finer scale mesoscale features, but it is still true that if a feature is not well-resolved by the rawinsonde data it generally is not well-represented in the initial state. The success of mesoscale models under these conditions has been the result of the fact that a significant fraction of mesoscale features result from (1) the non-linear interactions between coarse scale (resolvable by the rawinsonde network) features; and (2) the forcing supplied by small scale features of the earth's surface (e.g. land/water boundaries, terrain elevation features, etc.) which are fixed in time and can be accurately mapped. Fortunately, new observing system technology is beginning to provide operational tools which can be used to make routine measurements of mesoscale features. These systems offer the potential to improve the initialization of mesoscale models and to provide mesoscale data to improve the parameterization schemes used in mesoscale models. Examples of these new systems are Doppler wind profilers and NEXRAD Doppler radars. Unfortunately, virtually all of the new observing systems provide high quality and high resolution measurements of only a subset of the variables which are required for initialization. For example, the NEXRAD system provides only reflectivity and radial wind data. However, a mesoscale model needs both components of the horizontal wind

field, the temperature, surface pressure, water vapor mixing ratio and the cloud water and rain water mixing ratio values. The challenge during the coming years will be to create an initialization procedure that utilizes a combination of remote sensing systems and innovative data retrieval techniques to build an initialization dataset which can resolve the three-dimensional structure of meso-β scale features such as mesoscale convective systems.

Another issue that has frustrated all atmospheric modelers is the insatiable thirst that atmospheric models have for computational power. As computers become more powerful, atmospheric models have quickly consumed all of the increased power by using higher resolution grids and incorporating more detailed physics. Thus, the processing time for the "best" simulation always tends to be the maximum acceptable time for a particular research or operational application. Fortunately, computer technology is advancing rapidly at the present time. It is becoming increasingly evident that the principal scientific computing engines of the mid to late 1990's will be characterized by massive parallelism (hundreds to thousands of processors) in a distributed memory configuration. An overview of the current state of parallel computing and prospects for the future is presented by Poutain and Bryan (1992). All the evidence indicates that computational performance will increase dramatically in all price ranges over the next several years. The increased performance will provide an opportunity for the user with modest resources to run a three-dimensional mesoscale simulation over a significant domain in less than an hour on a low-cost desktop computer capable of generating processing speeds of 100 Megaflops. On the other end of the spectrum, the user with substantial resources will be able to execute non-hydrostatic cloud-scale resolution simulations over mesoscale domains in near real-time on high performance massively parallel supercomputers that can attain processing speeds between 500 Gigaflops and 1 Teraflop.

REFERENCES

Anthes, R. A., 1977: A cumulus parameterization scheme using a one-dimensional cloud model. *Mon. Wea. Rev.*, **105**, 270-286.

Boris, J. and D. Book, 1973: Flux-corrected transport. I. SHASTA, a fluid transport algorithmthat works, *J. Comput. Phys.*, **11**, 38-69.

Carpenter, Jr., R. L. , K. Droegemeier, P. Woodward, and C. E. Hane, 1990: Application of the Piecewise Parabolic Method (PPM) to Meteorological Modeling. *Mon. Wea. Rev.*, **118**, 586-612.

Carey, S. N. and H. Sigurdsson, 1982: Influence of particle aggregation on deposition of distal tephra from the May 18, 1980, eruption of Mount St. Helens volcano. *J. Geophysical Res.*, **87**, No. B8, 7061-7072.

Charney, J. G., M. Halem, and R. Jastrow, 1969: Use of incomplete historical data to infer the present state of the atmosphere. *J. Atmos. Sci.*, **26**, 1160-1163.

Coats, G. D., V. C. Wong, J. W. Zack and M. L. Kaplan, 1984: A numerical investigation of the effect of soil moisture gradients on the regional severe storm environment, Preprints of the 10th Conference on Weather Forecasting and Analysis, June 25-29, 1984, Clearwater Beach, Florida, 506-512.

Cram, J. M., M. L. Kaplan, C. A. Mattocks and J. W. Zack, 1991: The use and analysis of profiler winds to derive mesoscale height and temperature fields: simulation and real-data experiments. *Mon. Wea. Rev.*, **119**, 1040-1056.

Frank, W.M., and C. Cohen, 1987: Simulation of tropical convective systems. Part I: A cumulus parameterization. *J. Atmos. Sci.*, **44**, 3787-3799.

Fritsch, J.M., E.L. Magaziner, and C.F. Chappell, 1980: Analytical initialization for three-dimensional numerical models. *J. Appl. Meteor.*, **19**, 809-818.

——— and C.F. Chappell, 1980: Numerical prediction of convectively driven mesoscale pressure systems. Part I: Convective parameterization. *J. Atmos. Sci.*, **37**, 1722-1733.

Hodur, R.M., 1987: Evaluation of a regional model with an update cycle. *Mon. Wea. Rev.*, **115**, 2707-2718.

Hoke, J. E., and R. A. Anthes, 1976: The initialization of numerical models by a duynamical initialization technique. *Mon Wea. Rev.*, **104**, 1551-1556.

Kaplan, M. L., J. W. Zack, V. C. Wong and J. J. Tuccillo, 1982a: A mesoscale eighth-order numerical modeling system and the "Red River" tornado outbreak of 1979 (Part I - model structure), *Preprints to the 12th Conference on Severe Local Storms*, San Antonio, Texas, January 11-15, 1982, 546-553.

———, ———, ——— and ———, 1982b: A mesoscale eighth-order numerical modeling system and the "Red River" tornado outbreak of 1979 (Part II analysis and simulation of the tornado outbreak), *Preprints to the 12th Conference on Severe Local Storms*, San Antonio, Texas, January 11-15, 1982, 554-555.

———, ———, ——— and ———, 1982c: Initial results from a mesoscale atmospheric simulation system and comparisons with an AVE-SESAME I data set. *Mon. Wea. Rev.*, **110**, 1564-1590.

———, ———, ——— and G. D. Coats, 1982d: The interactive role of subsynoptic scale jet streak and planetary boundary adjustments in organizing an apparently isolated convective complex, *Preprints of the 9th Conference on Weather Forecasting and Analysis*, Seattle, Washington, June 28 - July 1, 1984, 407-416.

———, ———, ——— and ———, 1985: The interactive role of subsynoptic scale jet streak and planetary boundary layer adjustments in organizing an isolated convective complex. *Mon. Wea. Rev.*, **113**, 2212-2238.

Karyampudi, V. M., J. W. Zack, M. L. Kaplan and J. M. Cram, 1988: A split-explicit time integration scheme for the MASS model. *Preprints of the 8th Conference on Numerical Weather Prediction*, Baltimore, MD, American Meteorological Society, Boston, 807-814.

Koch, S. E., 1985: Ability of a regional scale model to predict the genesis of intense mesoscale convective systems, *Mon. Wea. Rev.*, **113**, 1693-1713.

———, W.C. Skillman, P.J. Kocin, P.J. Wetzel, K.F. Brill, D.A. Keyser and M.C. McCumber, 1985: Synoptic scale forecast skill and systematic errors in the MASS 2.0 model. *Mon. Wea. Rev.*, **113**, 1714-1737.

Kocin, P. J., L. W. Uccellini, J. W. Zack and M. L. Kaplan, 1985: A mesoscale numerical forecast of an intense convective snowburst along the east coast, *Bull. Amer. Meteor. Soc.*, **66**, 1412-1424.

Kuo, H.L., 1965: On formation and intensification of tropical cyclones through latent heat release by cumulus convection. *J. Atmos. Sci.*, **22**, 40-63.

Mahfouf, J.-F. and B. Jacquemin, 1989: A study of rainfall interception using a land surface parameterization for mesoscale meteorological models. *J. Appl. Meteor.*, **28**, 1282-1302.

Mahrt, L. and H. Pan, 1984: A two-layer model of soil hydrology. *Boundary-Layer Meteorol.*, **29**, 1-20.

Mattocks, C. A. and R. Bleck, 1986: Jet streak dynamics and geostrophic adjustment processes during the initial stages of lee cyclogenesis, *Mon. Wea. Rev.*, **114**, 2033-2056.

McCumber , M. C. and R. A. Pielke, 1981: Simulation of the effects of surface fluxes of heat and moisture in a mesoscale numerical model. *J. Geophys. Res.*, **86**, 9929-9938.

Mesinger, F., Z. Janjic, S. Nickovic, D. Gavrilov and D. Deaven, 1988: The step-moutain coordinate: model description and performance for cases of Alpine cyclogensesis and for a case of Appalachian redevelopment. *Mon. Wea. Rev.*, **116**, 1493-1518.

MESO, 1993a: *MASS Version 5.5 Reference Manual*, 118 pp. [available from MESO, Inc., 185 Jordan Rd, Troy, NY 12180]

MESO, 1993b: *MASS Version 5.5 User's Guide*, 57 pp. [available from MESO, Inc., 185 Jordan Rd, Troy, NY 12180]

Molinari, J and M. Dudek, 1992: Parameterization of convective precipitation in mesoscale models: a critical review. *Mon. Wea. Rev.*, **120**, 326-341.

Noilhan, J. and S. Planton, 1989: A simple parameterization of land surface processes for meteorological models. *Mon. Wea. Rev.*, **117**, 536-549.

Oke, T. R., 1978: *Boundary Layer Climates*, Methuen, London, 372 pp.

Orlanski, I., 1976: A simple boundary condition for unbounded hyperbolic flows. *J. Comput. Phys.*, **21**, 251-269.

Perkey, D. J., 1976: A description and preliminary results from a fine-mesh model for forecasting quantitative precipitation. *Mon. Wea. Rev.*, **104**, 1513-1526.

Perkey, D. J. and C. W. Kreitzberg, 1976: A time-dependent lateral boundary scheme for limited-area primitive equation models. *Mon. Wea. Rev.*, **104**, 745-755.

Pielke, R. A., 1984: *Mesoscale Meteorological Modeling*, Academic Press, New York, 612 pp.

Pountain, D. and J. Bryan, 1992: All systems go. *Byte*, August 1992, 112- 136.

Proctor, F. H., 1985: Application of radiative boundary conditions to nonhydrostatic primitive equation models, Preprints of the 7th Conference on Numerical Weather Prediction, Montreal, Canada, American Meteorological Society, Boston, 291-298.

Sarna-Wojcicki, A.M., S. Shipley, R. Waitt, Jr., D. Dzurisin and S. Wood, 1982: Aeral distribution, thickness, mass, volume and grain-size of airfall ash from six major eruptions of 1980 in *The 1980 Eruptions of Mount St. Helens, Washington*, edited by P.W. Lipman and D.R. Mullineaux, U.S. Department of Interior, Washington, D.C.

Segal, M., J. R. Garratt, R. A. Pielke and Z. Ye, 1991: Scaling and numerical model evaluation of snow-cover effects on the generation and modification of daytime mesoscale circulations. *J. Atmos. Sci.*, 48, 1024-1042.

Sellers, P. J., F. G. Hall, G. Asrar, D. E. Strebal and R. E. Murphy, 1988: The First ISCLCP Field Experiment (FIFE). *Bull. Amer. Meteor. Soc.*, 69, 22-27.

Smolarkiewicz, P.K., 1983a: A simple positive definite advection scheme with small implicit diffusion. *Mon. Wea. Rev.*, 111, 479-486.

———, P.K., 1983b: A fully multidimensional positive definite advection transport algorithm with small implicit diffusion. *J. Comput. Phys.*, 54, 325-362.

———, P.K. and T.L. Clark, 1986: The multidimensional positive definite advection transport algorithm: Further development and applications. *J. Comput. Phys.*, 67, 396-438.

Stauffer, D. R., N. L. Seaman, and F. S. Binkowski, 1991: Use of four-dimensional data assimilation in a limited-area mesoscale model. Part II: Effects of data assimilation within the planetary boundary layer. *Mon. Wea. Rev.*, 119, 734-754.

Tripoli, G.J. and W.R. Cotton, 1989: Numerical study of an observed orogenic mesoscale convective system. Part I: Simulated genesis and comparison with observations. *Mon. Wea. Rev.*, 117, 273-304.

Uccellini, L. W., M. L. Kaplan, J. W. Zack, G. D. Coats and S. L. Chuang, 1983: Mesoscale numerical simulations of the Presidents' Day cyclone; impact of sensible and latent heating on the precyclogenetic environment, *Preprints of the 6th Conference on Numerical Weather Prediction*, Omaha, Nebraska, June 6-9, 1983, 45-52.

———, R.A. Petersen, K. F. Brill, P.J. Kocin and J.J. Tuccillo, 1987: Synergistic interactions between an upper-level jet streak and diabatic processes that influence the development of a low-level jet and a secondary coastal cyclone. *Mon. Wea Rev.*, 115, 2227-2261.

Waight, K.T. , J.W. Zack and V.M. Karyampudi, 1989: The need for enhanced initial moisture information in simulations of a complex summertime precipitation event. *Preprints to the 12th Conference on Weather Analysis and Forecasting*, Monterey, California, American Meteorological Society, Boston..

——— and J.W. Zack, 1990: An analysis of a small mesoscale convective system during COHMEX. *Preprints to the Fourth Conference on Mesoscale Processes*, Boulder, Colorado, American Meteorological Society, Boston.

Warner, T. T. and N. L. Seaman, 1990: A real-time mesoscale numerical weather-prediction system used for research, teaching, and public service at the Pennsylvania State University. *Bull. Amer. Meteor. Soc.*, 71, 792-805.

Whitaker, J.S., L. W. Uccellini and K.F. Brill, 1988: A model-based diagnostic study of the rapid development phase of the Presidents' Day cyclone. *Mon. Wea Rev.*, 116, 2337-2365.

Wong, V. C., J. W. Zack, M. L. Kaplan and G. D. Coats, 1983: A nested-grid limited-area model for short-term weather forecasting, *Preprints of the 6th Conference on Numerical Weather Prediction, Omaha*, Nebraska, June 6-9, 1983, 9-15.

Zack, J. W., V. C. Wong, M. L. Kaplan and G. D. Coats, 1984: A model-based investigation of the role of boundary layer fluxes and deep convective processes in the precipitation distribution of east coast cyclones. *Preprints of the 10th Conference on Weather Forecasting and Analysis*, June 25-29, 1984, Clearwater Beach, Florida, 588-595.

——— and M. L. Kaplan, 1987: Numerical simulations of the subsynoptic features associated with the AVE-SESAME I Case, Part I: The preconvective environment. *Mon. Wea. Rev.*, 115, 2367-2394.

———, V. M. Karyampudi, C. A. Mattocks and G. D. Coats, 1988: Meso-beta scale simulations of convective cloud systems over Florida utilizing synthetic data derived from GOES satellite imagery. *Preprints of the 8th Conference on Numerical Weather Prediction*, Baltimore, MD, American Meteorological Society, Boston. 293-300.

Zalesak, S. T., 1979: Fully multidimensional flux-corrected transport algorithms for fluids, *J. Comput. Phys.*, 31, 335-362.

Zhang, D.-L. and R. A. Anthes, 1982: A high resolution model of the planetary boundary layer - sensitivity tests and comparisons with SESAME-79 data. *J. Appl. Meteor.*, 21, 1594-1609.

———, and J. M.Fritsch,,1988: A numerical investigation of a convectively generated, inertially stable, extratropical warm-core mesovortex over land. Part I: Structure and evolution. *Mon. Wea. Rev.*, 116, 2660-2687.